NATURAL FORMATION OF NANOSTRUCTURES: FROM FUNDAMENTALS IN METAL HETEROEPITAXY TO APPLICATIONS IN OPTICS AND BIOMATERIALS SCIENCE

BERT MÜLLER

Departement Werkstoffe, Eidgenössische Technische Hochschule Zürich,
Wagistrasse 23, CH-8952 Schlieren, Switzerland

The tailoring of nanostructures by the use of vapor deposition techniques opens up new opportunities to engineer innovative materials and devices in different fields, including optoelectronics and biomaterials. This review elucidates recent advances in the understanding of heteroepitaxy exemplifying the growth of copper on Ni(100) and the growth of para-hexaphenyl on GaAs. Although copper on nickel belongs to the simplest systems, unprecedented morphologies arise, such as ramified islands on a square lattice and strain relief by internal faceting. The elongated para-hexaphenyl crystallites formed on GaAs(001) exhibit a polarized blue light emission, which is a basis for developing organic diode lasers. Anisotropic thin film morphologies are also realized by oblique incidence deposition of noncentrosymmetric organic molecules onto amorphous substrates. Using the frequency doubling of light, it has been demonstrated for the first time that the films not only are anisotropic but also exhibit a preferential orientation of the molecules. Germanium nanopyramids epitaxially grown on Si(001) provide evidence that a well-defined nanopatterned substrate alters the contact angles of water, the protein adsorption and activity, as well as the cell behavior. These results are a milestone in structural biocompatibility on the nanometer scale.

1. Introduction

1.1. *Nanopatterning by molecular beam epitaxy*

Well-prepared single crystalline surfaces are an ideal substrate for studying the formation of islands by physical vapor deposition. Molecular beam deposition (MBD) — or, in the case of epitaxial growth, molecular beam epitaxy (MBE) — belongs to the most versatile deposition techniques.[1,2] Here, atoms, molecules or clusters are deposited from a molecular beam onto the substrate. The density of particles within the beam is so low that there is no particle interaction above the surface. MBE with reasonable growth rates, however, occurs only far from the thermodynamic equilibrium. Thus, the growth is a kinetic process governed by the competition between thermodynamics and growth kinetics. The understanding of this competition has led to the control and manipulation of the MBE growth process. This knowledge can be used to generate artificial surface structures with a desired architecture down to the atomic level. The choice of the external parameter, i.e. the deposition rate and the substrate temperature, determines the surface morphology at the specific coverage. The growth kinetics particularly dominate at low substrate temperatures and high deposition rates, i.e. at a high degree of supersaturation.

The deposition time, and therefore the coverage, is easily controlled by the shutter in front of the source or in front of the substrate with a precision better than 1/10 s. Sandwich structures with abrupt interfaces on the atomic level are generated by combining MBE sources for different species. The kind of defects and their density within the film, however, depend not only on the choice of substrate and film materials including their thicknesses, but also crucially on substrate temperature and deposition rate. This implies, on the other hand, that 1D or 0D nanostructures, termed "quantum wires" and "quantum dots," can be tailored by the choice

of MBE growth conditions, if the essentials for the growth of the particular system are known. Hence, these methods give rise to the natural formation of nano- and micropatterns consisting of islands with a well-defined size, shape, spacing, orientation and composition down to the atomic level.

The growth processes and the succeeding surface architecture or morphology are especially simple if substrate and film material are identical. Here, in the homoepitaxial growth, strain only results from surface effects. Consequently, strain plays a minor role. Homoepitaxy, however, is rather interesting from a fundamental point of view, since any ultimate application of nanostructures is based on the combination of different materials as shown by different examples below. Here, the question arises as to whether the knowledge from homoepitaxial growth can be directly transferred to heteroepitaxy. Maybe, for the very early stages of growth, where the strain plays only a minor role, nucleation and scaling theories are applicable. The thermodynamic constraints due to the lattice strain and their potential influence on the growth kinetics are discussed in detail for one of the simplest systems, copper on Ni(100). Another section deals with the growth of a highly anisotropic, rather large organic molecule on GaAs surfaces. In general, it is believed that organic materials do not interact strongly enough with the substrate to exhibit the typical epitaxial growth behavior but only give rise to a certain order.[3–5] Therefore, this phenomenon is termed "quasiepitaxy." Furthermore, the anisotropy of the molecular shape makes the applicability of the present growth models questionable. Anisotropies, however, are quite common in nature and often desirable, for example to realize optical nonlinearities.[6] Consequently, it is important to figure out possible ways to align organic molecules by physical vapor deposition. It is well known that inorganic films grown at oblique incidence deposition exhibit anisotropic properties,[7–11] but it has not been shown by organic materials.

1.2. *Tailoring thin film properties using epitaxial strain*

The properties of thin films can differ from those in bulk largely since the films are generated artificially far from equilibrium. Therefore, it is possible to tailor the physical and chemical properties of the film

and to produce artificial structures, which do not exist in nature. A recent example is the doubling of the critical temperature T_c of high temperature superconductors using the epitaxial strain.[12,13] It is well known that the application of hydrostatic pressure can raise T_c. It is, therefore, not surprising that the strain due to the lattice mismatch between substrate and film material affects T_c. While the hydrostatic pressure is necessarily isotropic, the strain dependence of T_c has opposite signs along different crystallographic orientations. Therefore, the substrate material and the growth conditions have to be chosen appropriately so that the uniaxial strain does not decrease but increase T_c. The appropriate choice of substrate material and growth conditions is also complicated because many strain-relieving defects are known which destroy the desired properties. Locquet *et al.*[12] have managed all these problems and realized an increase of T_c which is much larger than any achieved by standard pressure techniques. The understanding of the strain relief mechanisms, which occur in heteroepitaxial growth, is therefore not only interesting from a fundamental point of view but becomes important for potential applications in different fields.

On the other hand, one can take advantage of the strain-relieving defect structures. For example, Brune *et al.*[14] have used the strain relief pattern, which is spontaneously created by mono- or bilayer metal films on fcc(111) metals with a different lattice constant, as a template to grow silver and iron nanostructures. These islands have a well-defined separation and a narrow size distribution. Thus, this method should be useful for realizing quantum dot arrays, where the size and the period of the dots are smaller than the Fermi wavelength.

1.3. *Nanoscale surface architecture — a key aspect of biocompatibility*

The significance of topographic features of micrometer size for cell shape and function has been clearly demonstrated.[15–20] However, the power of features on the nanometer scale in phenomena such as protein adsorption, cell function and, finally, tissue formation is still unclear.

Considering bone, an example of highly organized tissue, one finds apatite crystallites with sizes of about 10 nm. The size and shape of these crystallites,

as well as their density and size distribution, are parameters possibly essential for bone–bone-cell interactions. The hypothesis is that implant surfaces have to be structured on the nanometer scale similar to natural bone containing nanometer-sized apatite crystals in order to realize an optimal incorporation of the implant into the human body. Besides the effects on the mechanical properties of bone tissue itself, there are several fundamental questions related to the role of the nanometer-sized apatite crystals. In the tissue, the bone cells, having an average diameter of 20–50 μm, are attached to each other and to the fibrillar proteineous network known as the extracellular matrix (ECM). In general, bone cells need this attachment and the subsequent spreading on the ECM for their functionality and their survival. The interactions of the cells with the ECM occur mainly by a class of transmembrane molecules, termed "integrins." The integrins are clustered in focal adhesion points, which can be visualized by electron microscopy[21] and other techniques. One question is: How far do nanometer-sized structures such as apatite crystallites determine the number and size of focal adhesion points? Furthermore, even if the number and size of focal adhesion points per cell are fixed, their distribution on a nanostructured surface is expected to steer the cell anchorage and, thereby, may strongly affect the cell function. Thus, the surface architecture on the nanometer scale is predicted to control the cell shape and function. Investigations with fibroblasts on smooth and rough substrates on the micrometer scale *in vitro* have revealed that focal adhesion points show a concentration on prominent ridges, and no focal adhesion points are found in groves of the substrate.[21–25] The fundamental question is: How small can the feature be made to still have this response?

The interaction between tissue and implant is also crucial in craniomaxillofacial surgery where adhesion or nonadhesion decides the success of the surgical intervention. Bony integration is required for permanent implants, whereas osseointegration has to be avoided for temporary implants or for implants where an unhindered sliding of soft tissues is an absolute prerequisite. This is the case for tendons, or for the eye-globe in the orbital. Highly polished implant surfaces seem to result in minimal tissue adhesion; surface roughness seems to encourage osseointegration. Optimal conditions, especially in the submicron

range, for resulting in one or the other feature are not sufficiently known. The use of nanostructures of different dimensions, and distribution patterns, offers an excellent possibility of studying these effects under controlled conditions. Although one can find some indications in the literature,[26] it cannot be predicted at this time to what extent nanostructures can improve the routine implant surfaces.

This review covers preliminary experiments with germanium nanopyramids grown on Si(001) by chemical vapor deposition. The influence of the nanopyramid density on the contact angle hysteresis of water, the adsorption and activity of selected proteins, and the cell behavior is addressed. *In vitro* assays with monocytes on Ge/Si nanostructures, which are related to specific aspects of inflammatory reactions of the body, are performed to decide if oxidized Ge nanostructures are biocompatible and, therefore, appropriate for *in vivo* experiments. *In vivo* evaluation of promising surface topographies can address both aspects: Those favoring adhesion and those favoring nonadhesion. The cranial vault of the rabbit could be chosen as implantation site. This region, and thereby the implant, is not highly loaded, and no major contouring of the implant is required. The implant can be placed subperiosteally. The collected data of the comprehensive study combining physical and biological sciences can be used to optimize the nanostructures of bone implants. The final goal is the improvement of the interface between implant material and bone tissue which is crucial for the function and long term stability of the implant. The understanding of the fundamental processes is a prerequisite for this ambitious goal.

2. Initial Stages of Heteroepitaxy — A "Simple" Example, Cu/Ni(100)

Copper on Ni(100) belongs to the simplest heteroepitaxial systems. Copper on nickel has been selected for the fundamental study since the two elements are very similar not only from a chemical point of view but also concerning their atomic structure. Both are face-centered-cubic metals, where the {100} surfaces exhibit a lattice with square symmetry. Under well-defined ultrahigh vacuum conditions, the (100) surface does not reconstruct. The lattice constant of copper ($a_{Cu} = 0.36147$ nm) is only 2.6% larger than that of nickel ($a_{Ni} = 0.35237$ nm).[27] Below

400 K, intermixing between copper and nickel is not observed. At these substrate temperatures, re-evaporation of copper atoms is negligible. Copper, deposited in the form of monomers by means of thermal evaporation, grows on Ni(100) in an almost ideal layer-by-layer fashion.[28–31] The data indicate that surface migration takes place by adatom hopping, as already shown by simulations.[32] Hence, copper on Ni(100) should be an appropriate candidate for studying the influence of compressive strain on fundamental processes such as nucleation, growth and defect formation in a simple atomic system with square symmetry.

2.1.   *Hierarchy of activated processes in epitaxial growth*

2.1.1.   *Concept of the critical nucleus and lattice symmetry*

In general, the stability of islands depends on their size. Small islands decay or dissociate if they are sub-critical. The size of the critical nucleus i corresponds to an island which becomes stable by the incorporation of an extra atom. Stable refers to the time scale of deposition. This means that stable islands have a higher probability of growing than dissociating during the deposition experiment.

For the lowest substrate temperatures, the statistically deposited monomers are incorporated at the nearest lattice site. Surface migration does not occur at all. The regime, where the monomer is immobile ($i = 0$), is termed "statistic growth" and results in a rough surface morphology. With increasing substrate temperature, the monomers become mobile and start to migrate. However, the dimers are immobile, and therefore stable ($i = 1$). If one increases the substrate temperature further, the dimers dissociate (or migrate as a whole dimer), and either the trimer becomes the smallest stable island ($i = 2$), or the smallest stable island corresponds to the tetramer ($i = 3$), and so on.

This is a classic continuum model that completely ignores the adsorption site geometry of the crystalline substrate. The adsorption site geometry does not play any role for the small critical island sizes $i = 0$ and $i = 1$. For the larger islands, however, the total binding energy substantially depends on the geometric arrangement of the atoms within the island. The possible configurations are given by the

lattice symmetry of the substrate, as shown for the square and hexagonal lattices in Fig. 1. The atoms within the most stable trimer ($i = 2$) on a hexagonal surface are characterized by laterally twofold-coordinated atoms. On the lattice with square symmetry, on the other hand, the trimers can always dissociate by single bond breaking. Hence, on a square lattice, dimers and trimers are associated with similar dissociation barriers, and a direct change from $i = 1$ to $i = 3$ that is related to the transition from single to double bond breaking is observed. Since dissociation of monatomic high islands on lattices with square symmetry is invariably characterized by single or double bond breaking, no well-defined transition above $i = 3$ has been found. The magic island sizes on a square lattice are the dimer and the tetramer, whereas on the hexagonal lattice the dimer (single bond breaking), the trimer (double bond breaking) and the heptamer (triple bond breaking) are the magic ones. Only recently, results of field ion microscopy have been reported those which demonstrate a definite correlation between atomic island structure and island stability (mobility) across a single crystal surface, namely Rh/Rh(100).[33] Such a behavior has been predicted before.[34] The oscillations in the activation barrier of surface migration as a function of island size are attributed to the island compactness.
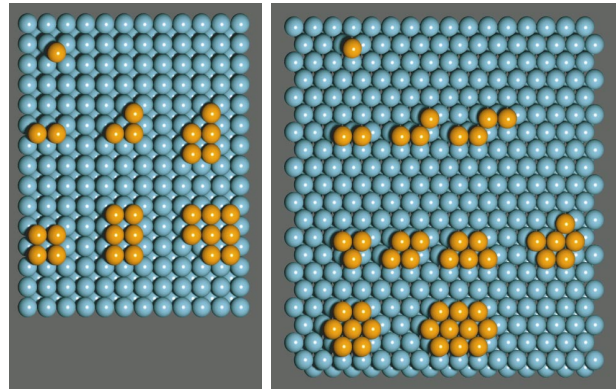

Fig. 1.   The square and hexagonal lattice symmetry and the related magic islands (first column in the left and the right picture, respectively). In the first line, there are single atoms on the hollow site. The islands in the second line are characterized by an extra atom along a close-packed direction. For island dissociation a single bond has to be broken laterally. For the islands in the third line one needs double bond breaking, whereas the islands in the fourth line only dissociate by triple bond breaking.

Compact islands have a relatively low mobility associated with a higher activation barrier since double bond breaking is required to detach an atom from the island's perimeter.

Experimentally, the size of the critical nucleus can be determined (i) by the direct measurement of the mean island size during the very early stages of growth,[35] (ii) by the measurement of the temperature threshold for Ostwald ripening,[36] (iii) by the determination of the rate dependence of the saturation island density using mean field nucleation theory,[37] and (iv) by the comparison of the island size distribution with simulations based on scaling theory.[38,39] The consistency between the two latter approaches is demonstrated below for copper on Ni(100).

2.1.2. *Thermally activated processes in MBE growth*

In general, MBE growth is used to generate layered structures with sharp interfaces. Therefore, it is necessary to start from an almost defect-free substrate, as shown by the blue–green lattice in Fig. 2. The only defect shown is the step with two kink sites. Such surfaces can be routinely prepared on metal and semiconductor substrates. In heteroepitaxy another material is deposited, here given by the orange spheres representing the copper atoms.

As discussed above, the thermal processes are frozen in at very low substrate temperatures. The first thermally activated process is usually the
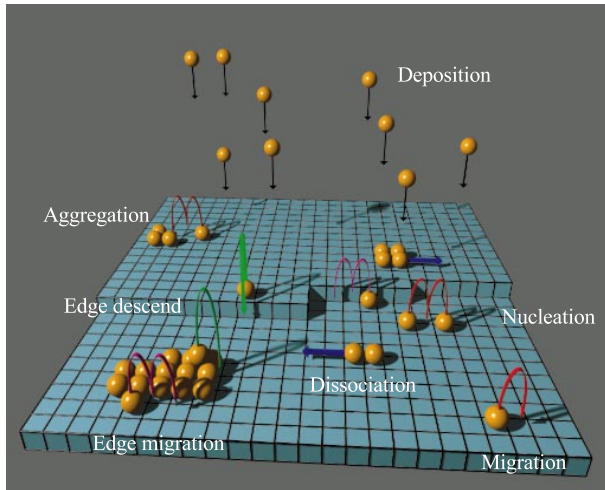

Fig. 2.   Hierarchy of activated processes: a scenario on the atomic level.

migration means that the application of an appropriated substrate temperature results just in the activation of a single process, which can be studied in detail. On increasing the substrate temperature a second process is activated, which can be analyzed under consideration of the first one. In principle, this kind of subsequent activation can be used to describe the different processes on the atomic scale. This hierarchy of a few important processes is represented in Fig. 2 by differently colored arrows: adatom terrace migration (red), edge migration (light pink), step descent (green), single and double bond breaking (blue). It is *a priori* difficult to determine the order of the thermal processes. Even for terrace migration of monomers, one of the simplest processes, different pathways such as hopping and exchange are identified. However, besides surface alloying, the island shape, the island density and the island size distribution as well as the occurrence of special defects give access to the order of the activation energies of the different processes.

2.2.   *Submonolayer nucleation and growth*

It is not the purpose of this review to describe nucleation theory and its applicability. Here, only the main ingredients of the theory are briefly recalled to elucidate the relation between the measured island densities and the external parameters: Substrate temperature and deposition rate. The mean field nucleation theory has been established by Venables.[40,41] For the very early stages of epitaxial growth on metals, the nucleation theory is comprehensively discussed in a recent review.[42]

2.2.1. *Island nucleation — the balance between monomer deposition and migration*

The migration of the adatoms on a periodic lattice by hopping, often termed "surface diffusion" or "tracer diffusion," is a thermally activated process.[43] Thus the hopping rate ν can be expressed by an exponential law:

$$\nu = \nu_0 \exp\left(-\frac{E_m}{kT}\right), \qquad (1)$$

where ν_0, the attempt frequency, and E_m, the migration barrier, are regarded as substrate-temperature-

independent quantities. T denotes the substrate temperature, and k is the Boltzmann factor. To describe the mean square displacement of a random walking adatom per time unit, the tracer diffusion coefficient D is coupled to the hopping frequency by the square of the surface lattice constant a_s times a geometric factor — a result of the Einstein relation. For a 2D motion on a square lattice, D is simply $a_s^2 \nu / 4$. Hence, the migration of the adatoms depends exponentially on the substrate temperature.

Assuming a substrate without special nucleation sites, the island density results from the balance between surface migration and deposition rate. The deposition rate is the main parameter introducing the time into the description of growth. It is the only time-dependent parameter, if already the dimer is stable and re-evaporation is negligible. The mean free path of atoms on the substrate before formation of a nucleus by the encounter of another adatom, and therefore the island density n_x, has been demonstrated to depend on the D/R ratio by a power law:

$$n_x \sim \left(\frac{D}{R} \right)^{-\chi} . \tag{2}$$

The scaling exponent χ is equal to $i/(i+2)$ for complete condensation and formation of 2D islands, as valid for the Cu/Ni system at substrate temperatures below 400 K. The scaling exponent for other nucleation regimes is given by Eq. (2.9) in Ref. 44. This scaling behavior of the island density with substrate temperature and deposition rate is a central issue of nucleation theory. It results from the traditional rate equation analysis for the growth model we discuss.

2.2.2.   *Rate equation approach*

A traditional method for understanding and simulating the kinetics of the initial stages of the growth process is based on ideas developed by von Smoluchowski many decades ago.[45,46] He used a mean field approach neglecting the crystal geometry of substrate and film. This approach, refined by many authors, is given below for the simple case, where only monomers migrate ($i = 1$), although much more complex situations can be treated. For our system with square symmetry the time evolution of the monomer density n_1 and the density of stable islands n_x can be represented by a set of two differential equations:

$$\frac{dn_1}{dt} = R - 2D\sigma_1 n_1^2 - D\sigma_x n_1 n_x$$
$$\qquad - R(Rt - n_1) - 10Rn_1 , \tag{3}$$
$$\frac{dn_x}{dt} = D\sigma_1 n_1^2 + 5Rn_1 - n_x \left(R - \frac{dn_1}{dt} \right) .$$

The capture numbers σ_1 and σ_x describe the propensity of monomers and stable islands, respectively, to incorporate migrating adatoms. The monomer density increases by the deposition rate R. It is reduced by island formation and aggregation processes: Two monomers form a dimer by migration (second term); a monomer aggregates at a stable island by migration (third term); a monomer is deposited on top of a stable island (fourth term); and on top of another monomer or on a nearest neighbor site (fifth term). The factor of ten in the fifth term accounts for the fact that a dimer is created either when the monomer directly arrives on top of the adsorbed monomer, or on one of its four neighboring sites; these five channels have to be doubled since two monomers disappear by the dimer formation. The deposition of monomers onto neighboring sites of stable islands is neglected here for simplicity. The density of the stable islands, on the other hand, increases by dimer generation due to monomer migration (the first term of the second equation) and due to the deposition of an atom on top of a monomer and its nearest neighbor sites (second term). Coalescence reduces the density of stable islands (third term).

The validity of the differential equations is closely related to the choice of the capture numbers. The simplest choice is a constant value, which is motivated by the fact that the capture of randomly walking monomers by islands does not strongly depend on their size for well-separated islands at small coverages (point islands). More important, rather sophisticated approximations show that the capture numbers do not significantly vary close to saturation coverage.[40,47] It turns out that the choice of $\sigma_1 = 3$ and $\sigma_x = 7$ works very well for saturation coverage.[42] Constant capture numbers give rise to the conventional scaling exponent given above. More sophisticated approaches for the capture numbers, such as the lattice approximation[40,47] (see below) and the uniform depletion approximation,[40,48,49] are discussed in detail elsewhere.[42]

It should be mentioned that the rate equation approach provides accurate predictions for mean values including the monomer and island density. However, owing to the neglect of spatial fluctuations it fails to yield a suitable description of the island size distributions.[49,50]

2.2.3. *Mean field nucleation*

At the beginning of the deposition process, the monomer density linearly grows with time until small islands start to nucleate. For the formation of 2D islands, the island density linearly increases as a result of nucleation. As deposition proceeds, the monomers vanish not only by nucleation but also by their incorporation into the existing islands (aggregation). Thus, the increase of the island density due to nucleation becomes smaller and smaller. At even higher coverage, island coalescence occurs, reducing the island density. Well below monolayer coverage, a percolation network forms, so that no isolated island remains.

For the determination of quantities such as the height of the migration barrier, the saturation island density that corresponds to maximal island density is used, because here the full expression of the island density is especially simple.[41] In good approximation for our system with square symmetry, the island density is given by

$$n_x = 0.2 \left(\frac{D}{R}\right)^{-\chi} \exp\left[\frac{E_i}{(i+2)kT}\right] . \qquad (4)$$

As discussed, the island density is generally a function of coverage. At saturation coverage, however, it remains constant. Here, a prefactor of 0.2 from Ref. 41 is used. E_i is the binding energy for the critical nucleus i, $E_0 = E_1 = 0$. Rewriting this equation,

$$n_x = 0.2 \left(\frac{4R}{\nu_0}\right)^{\frac{i}{i+2}} \exp\left[\frac{iE_m + E_i}{(i+2)kT}\right] , \qquad (5)$$

it becomes clear that the size of the critical nucleus is found by the measurement of the rate dependence of the island density. For $i = 1$, the migration barrier and the related attempt frequency can be extracted in a straightforward manner from the Arrhenius plot of the island density. Knowing these quantities, the binding energies can be determined from the mea-

surement of the island density at the regimes where $i > 1$.

2.2.4. *Analysis of submonolayer island densities for Cu/Ni(100)*

The island densities were determined from STM images by counting the islands on a certain area. The size of the analyzed area was corrected for thermal drift by keeping track of characteristic features in successively obtained images. The influence of structural defects such as steps was excluded by considering only areas far away from such defects. Analogous instrumentation as used was described by Brune *et al.*[51]

The dependence of the island density on coverage is qualitatively shown by a series of STM images in Fig. 3. Usually, saturation is expected at coverages between 0.1 and 0.2 monolayers. The related
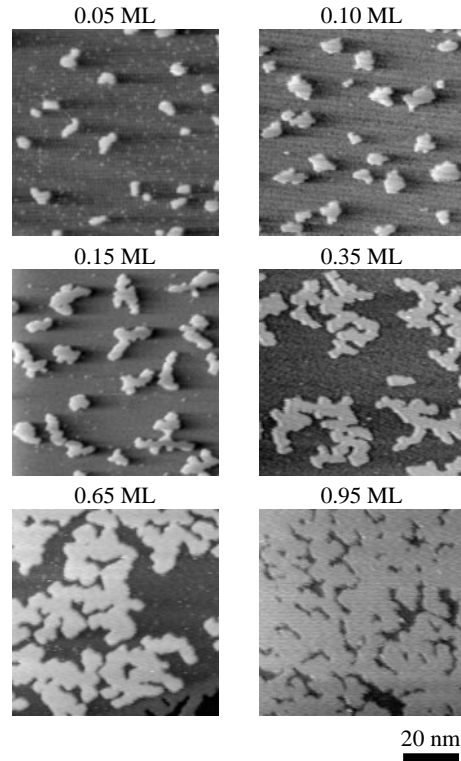

Fig. 3. STM images showing the evolution of the area density of copper islands on Ni(100) with coverage at a substrate temperature of 345 K and a deposition rate of 6×10^{-3} monolayers/s. The different submonolayer coverages are indicated. The copper islands are always of monolayer thickness. The larger islands exhibit a ramified shape.
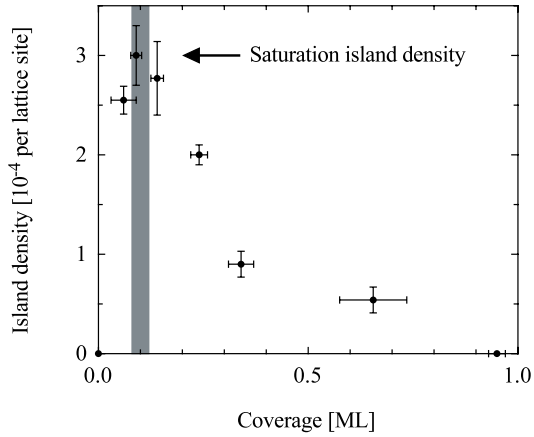
Fig. 4. Density of copper islands on Ni(100) versus coverage for a substrate temperature of 345 K and a deposition rate of 6×10^{-3} monolayers/s.
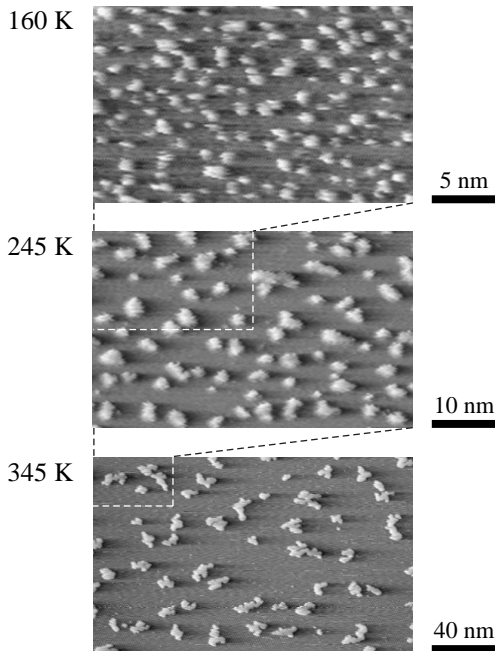

Fig. 5. STM images of 0.1 monolayer copper on Ni(100) characterizing the submonolayer growth at different substrate temperatures and a fixed deposition rate of 1.5×10^{-3} monolayers/s.

quantitative data (Fig. 4) reveal that for a substrate temperature of 345 K and a deposition rate of 6×10^{-3} monolayers/s, the island density stays constant between 0.08 and 0.12 monolayers. Therefore, this coverage range is considered to be the saturation level for the present system. Coalescence starts well above the expected percolation limit. Sometimes

the islands seem to split and to separate. A possible reason is the strain field around the islands as a result of the lattice mismatch between deposit and substrate. The lattice mismatch is also responsible for the ramified island shape, as discussed below.

The variation of the saturation island density with substrate temperature is qualitatively characterized in Fig. 5, showing three STM images obtained at a fixed deposition rate (1.5×10^{-3} monolayers/s) and saturation coverage. Lower substrate temperatures result in higher island densities. The decrease of the saturation island density over more than three orders of magnitude directly reflects the exponential temperature dependence of the adatom mobility.

Figure 6 shows the related quantitative data, i.e. the measured temperature dependence of the saturation island density as an Arrhenius plot. One can distinguish between three linear slopes of the curves that are associated with different nucleation regimes and labeled "postdeposition," "$i = 1$," and "$i = 3$," respectively.

Below 160 K, the island density does not vary with temperature, indicating that $i = 0$, i.e. monomers rest stably during deposition. The mean island size of 4–5 atoms is too large for statistic growth, where a mean island size of 1.25 atoms is obtained on a square lattice at a coverage of 0.1 monolayers from percolation theory.[52] Therefore, pure statistic growth can definitely be excluded. The physical reason for the plateau in the Arrhenius plot is related to a postdeposition effect, discussed below.

The two regimes entered above the substrate temperatures of 160 K and 320 K, respectively, have been labeled corresponding to the size of the critical nuclei. To establish these sizes, the rate dependences of the island density $n_x(R)$ at three different substrate temperatures, 145, 215 and 345 K, each located in the center of the labeled regions of the Arrhenius plot, have been measured.

As shown for isotropic 2D migration, the rate dependence of the saturation island density follows a power law with an exponent $i/(i + 2)$. It corresponds to 1/3 for $i = 1$, 1/2 for $i = 2$, and rises to 3/5 for $i = 3$. The double-logarithmic plots of the saturation island density versus the deposition rate in Fig. 7 reveal that the exponent corresponds to 0.32 ± 0.01 at a substrate temperature of 215 K and to 0.58 ± 0.02 at a substrate temperature of 345 K, which clearly shows that the monomer is the critical
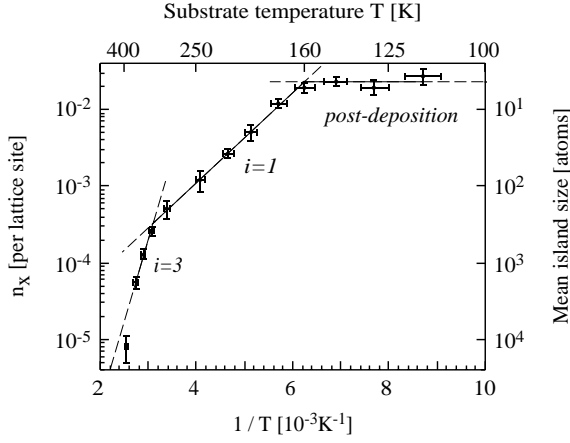
Fig. 6. Arrhenius plot of the measured saturation island density for copper on Ni(100) at a deposition rate of 1.5×10^{-3} monolayers/s.
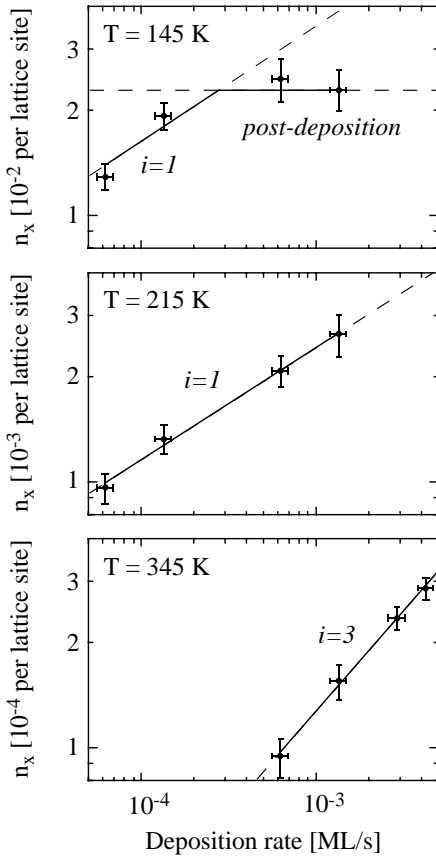

Fig. 7. Double-logarithmic plot of the island density versus deposition rate in the saturation regime (coverage 0.1 monolayer) at the substrate temperatures indicated.

nucleus at 215 K ($i = 1$) and the tetramer becomes the smallest stable island at 345 K ($i = 3$).

Because the analysis of the rate dependence of the saturation island density at 215 K results in a critical nucleus of 1, and the slope of the saturation island density in the Arrhenius plot is constant between 160 K and 320 K, the barrier height for adatom migration $E_m = (0.35 \pm 0.02)$ eV can directly be obtained from this slope. The related attempt frequency is found by the intersection of the linear fit with the ordinate and yields $\nu_0 = 4 \times 10^{11 \pm 1}$ Hz. Since we know the migration energy from the latter analysis, the dimer bond energy can be extracted in a similar way from the slope of the saturation island density between 320 K and 370 K. Here, the size of the critical nucleus is 3, and based on the bond counting argument, where E_i is given by the number of nearest neighbor adatom bonds in the critical nucleus i times the binding energy per bond E_b, we obtain $E_3 = 2E_b$, and $E_b = (0.46 \pm 0.19)$ eV. The related attempt frequency $\nu_0^* = 5 \times 10^{12 \pm 2}$ Hz agrees within the error bars with the attempt frequency of monomer migration. Therefore, one may assume that the attempt frequencies for the different processes are identical.

The dimer bond energy E_b is in general associated with a very large error bar due to the rather narrow temperature interval, where $i = 3$. A combined fit based on the assumption of an identical attempt frequency for monomer migration and dimer dissociation, which uses all data of the $i = 1$ and $i = 3$ regimes including their error bars, results in a well-defined value not only for the migration barrier but also for the dimer bond energy. The values obtained for the migration barrier (0.37 ± 0.03) eV, for the attempt frequency $5 \times 10^{11 \pm 1}$ Hz, and for the dimer bond energy $E_b = (0.34 \pm 0.03)$ eV coincide with the results of a previous analysis,[37] but the error bar of E_b is reduced by a factor of 6 since the intersections of the $i = 1$ and $i = 3$ curves with the ordinate are well defined in the combined fit. This dimer bond energy corresponds exactly to the value predicted by Evans and Bartelt for a transition temperature of 320 K based on kinetic Monte-Carlo simulations.[53] The migration barrier for Cu/Ni(100) is very similar to homoepitaxial systems: Fe/Fe(100),[39,54] Cu/Cu(100)[55–59] and Ag/Ag(100)[60–62] with square symmetry. The binding energy is rather high and gives rise to the well-defined and abrupt change of the smallest stable island from a dimer to a tetramer.

2.2.5.   *Scaling of the island size distributions*

Besides the island density, the island size distribution belongs to the fundamental quantities in the description of growth kinetics. In general, this distribution is a function of deposition time. If the deposition rate is constant, the time is introduced by the coverage $\theta = Rt$. The island size distribution $n_s(\theta)$ gives the density of islands of size s, where s is the number of atoms (molecules, clusters or other particles). The total island density n_x can be defined by

$$n_x = \sum_{s \geq 2} n_s(\theta) \qquad (6)$$

and the coverage by

$$\theta = \sum_{s \geq 1} s n_s(\theta). \qquad (7)$$

Therefore, the mean island size S can be written as

$$S = \frac{\sum_{s \geq 2} s n_s(\theta)}{\sum_{s \geq 2} n_s(\theta)} = \frac{\theta - n_1}{n_x}. \qquad (8)$$

The mean island size $S(\theta)$ defined in Eq. (8) is the only characteristic size in the description of growth. Therefore, one can assume that $n_s(\theta)$ scales with $S(\theta)$. In general, one may write $n_s(\theta) = F(S, \theta) f(s/S)$, with $f(s/S)$ as the scaling function for the island size distribution. The definition of θ and the scaling are the basis for the assumption that $F(S, \theta) = \theta/S^2$. Thus, a general form for the scaling behavior of the island size distribution is obtained:

$$n_s(\theta) = \left(\frac{\theta}{S^2}\right) f\left(\frac{s}{S}\right). \qquad (9)$$

Both experiments and simulations have shown that the scaling behavior is characteristic for the size of the critical nucleus.[37-39,50,63-70] Therefore, one can obtain the size of the critical nucleus by the comparison of the experimental data with simulations.

The scaled island size distributions for Cu/Ni(100) of the three growth regimes postdeposition at 160 K, $i = 1$ at 215 K and $i = 3$ at 345 K are presented in Fig. 8. The coverage corresponds to 0.1 monolayer at the substrate temperatures of 160 K and 215 K. For 345 K, however, the coverage chosen is much smaller, since for higher coverage the island becomes an irregular shape related to a significant broadening of the size distribution.
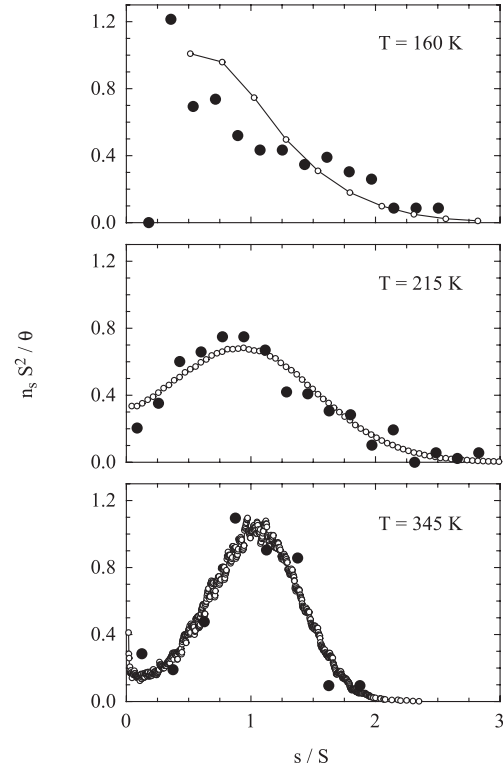

Fig. 8.   Scaled island size distributions deduced from STM images (filled circles). The substrate temperatures are indicated. The deposition rate was 1.5×10^{-3} monolayers/s. The experimental data are compared with simulations of M. C. Bartelt and J. W. Evans (open circles).

The experimental data are compared with simulations of M. C. Bartelt and J. W. Evans: Postdeposition effects as well as the ramified island shapes are considered for the $i = 1$ regime.[71] The simulations for $i = 3$ are presented in Appendix A of Ref. 62. Especially at the higher substrate temperatures, the agreement between simulations and experiments is obvious.

Consequently, the size of the critical nuclei is consistently determined by the rate dependence of the saturation island density using nucleation theory and by the scaled island size distribution using scaling theory.

2.2.6.   *Postdeposition effects in submonolayer nucleation and growth*

At low substrate temperatures the migration rate of adatoms becomes low with respect to the deposition rate. Therefore, during the deposition experiment, only a relatively small fraction of the migrating

adatoms can form nuclei or aggregate at existing islands; consequently, the monomer density is high. This high monomer density leads to postdeposition effects, i.e. they aggregate at existing islands (postgrowth) or even form additional islands by nucleation (postnucleation) after the deposition has been terminated. A similar effect arises during the interruption of MBE growth.[72,73] It is often observed after multilayer growth by RHEED intensity measurements during postgrowth recovery.[74] Here, however, we consider only the very early stages of growth in a quantitative manner.

The postdeposition effects at a certain coverage are characterized by the ratio between surface migration and deposition rate, D/R. For 0.1-monolayer copper on Ni(100), postgrowth is observed for D/R values between $\sim 10^5$ and $\sim 10^1$. For $D/R < 10$ postnucleation dominates. If migration of adatoms during the deposition and the subsequent imaging is suppressed, one finds statistic growth.

The experiments for Cu/Ni(100), where $D/R < 10^5$, show that postdeposition effects manifest a plateau in the Arrhenius plot of the saturation island density for substrate temperatures of less than about 160 K (cf. Fig. 6). The plateau is also found for the rate dependence of the saturation island density at 145 K (cf. Fig. 7). The crossing of the horizontal lines and the lines labeled "$i = 1$" in Figs. 6 and 7 corresponds to $D/R = 5 \times 10^2$. Furthermore, the scaled island size distribution at 160 K decreases monotonically, as found for statistic growth ($i = 0$).[65,75] Thus, postgrowth results in a scaling behavior very similar to statistic growth. But this behavior is accidental. The mean island sizes, however, are much larger because of the nonvanishing adatom mobility. Irrespective of substrate temperature and deposition rate, statistic growth on a square lattice results in a mean island size of 1.25 atoms at a coverage of 0.1 monolayer.[52] At 160 K, in the postgrowth regime, a much larger mean island size of 5.5 atoms is observed, which cannot be described by statistic growth.

These experimental findings are quantitatively explained by the rate equation analysis considering the regime where the monomers have a low mobility during deposition. The smallest stable island after deposition, however, is the dimer ($i = 1$). The numerical solution of the rate equations [Eq. (3)], which are integrated by a Runge–Kutta algorithm, gives both the monomer density n_1 and the density of the stable islands n_x as a function of time. The capture numbers of stable islands σ_x are chosen according to the lattice approximation.[40,47] For the monomers $\sigma_1 = 3$ has been chosen to simplify the calculation. It has been shown that this choice is a reasonable approximation.[35,76] It relies on the geometrical concept[77] applied to monomers. Postdeposition effects are considered by introducing a time-dependent deposition rate $R(t)$ that is constant during deposition and zero afterwards. The resulting densities of monomers and stable islands as a function of time are given in Fig. 9 on a logarithmic scale. During the first 75 s, a coverage of 0.1 monolayer is generated applying a constant deposition rate. After deposition, nucleation and growth processes due to monomer migration are considered for 300 s. The graph labeled "0 K" corresponds to immobile adatoms ($i = 0$). The curve actually shows the result of the integration of the rate equations at $T = 0$ K. It is
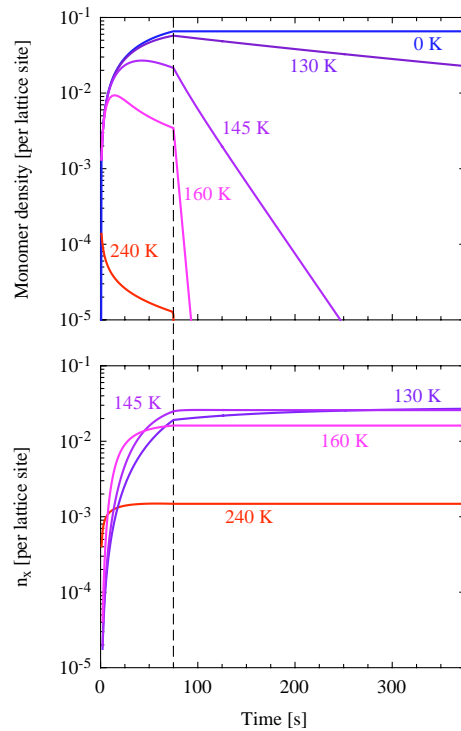

Fig. 9. Monomer density and density of the stable islands during and after deposition at the substrate temperatures indicated. The densities are determined by integrating the rate equations within lattice approximation. Deposition is performed between 0 and 75 s corresponding to a coverage of 0.1 monolayer.

almost identical to the result from percolation theory on the square lattice.[52] The minor difference is not apparent in Fig. 9. The monomer density derived by the rate equations is slightly lower (less than 5%), since atoms impinging on top of monomers are allowed to descend by dimer formation, whereas these atoms are removed in percolation theory. The statistic growth is related to the highest possible island density, because the monomers belong to the stable islands. Note that the curve obtained for a substrate temperature of 130 K is still quite close to the statistic growth regime. With increasing temperature, one can nicely see how the monomer density left after deposition steadily decreases, since an increasing number of islands nucleate and grow already during deposition. The final densities of stable islands islands are quite similar for $D/R < 10^4$, which correspond to substrate temperatures below 160 K. Further integration for a substrate temperature of 130 K still increases the density of stable islands. This means that the postdeposition effects give rise to the experimentally observed plateau in the Arrhenius plot. For comparison a curve for the dynamic nucleation and growth behavior at a substrate temperature of 240 K is shown in Fig. 9. Here, nearly all monomers are incorporated during deposition.

The island density in the regime where the dimer is stable can be derived from the rate equation analysis as shown in Fig. 10, where the experimental data are compared with the results of the simulation. The quantitative agreement between the experimentally observed island densities and the simulated ones may be improved by a more appropriate choice of capture numbers. The lattice approximation gives slightly higher values than the experiment, as also found by Bott *et al.*[76] The upper line in Fig. 10 represents the calculated total island density including the monomers (amount shaded gray), which exist after a wait time of 10^4 s, while the lower line shows only the density of stable islands, i.e. dimers and larger islands. For the dynamic and the postgrowth regime, the curves are identical. The difference between the solid curve and the experimental data in the postnucleation regime suggests that atoms upon deposition have an enhanced mobility with respect to equilibrated adatoms at these substrate temperatures. This might be ascribed to transient mobility.[78] However, this phenomenon has
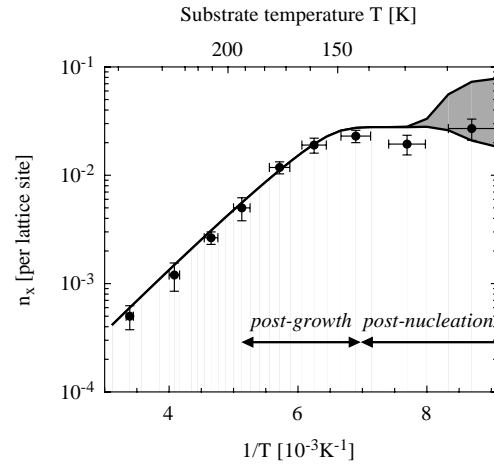

Fig. 10.   Comparison of calculated and measured island densities. The postdeposition effects (postgrowth and postnucleation) are well reproduced by the rate equation analysis.

not yet been proven by experiment. Therefore, another mechanism, i.e. the next-nearest-neighbor-driven mobility or the easy attachment, is proposed to explain the difference. Here, atoms in the direct vicinity of the islands have a reduced barrier for hopping,[79,80] an effect which is not considered by the present rate equation analysis.

Postdeposition is a phenomenon related to the ratio of monomer migration and deposition rate. Both the island density and the island size distribution are modified as a result of these postdeposition effects at $D/R < 10^5$.

2.3.   Strain-induced island shape transition

2.3.1.   Ramified island formation

The architecture of an epitaxially grown surface is characterized not only by the island density and the island size distribution but also by the shape of the islands. A great variety of compact and ramified island shapes have been observed even for single layer 2D islands. Scanning tunneling microscopy studies of metal-on-metal growth have revealed that ramified island shapes are frequently found on surfaces with triangular and hexagonal symmetry whereas compact islands have been observed on substrates with square symmetry.[81] The atomic mechanisms of fractal or dendritic growth can be easily explained by hit-and-stick models such as diffusion-limited

aggregation (DLA).[81–86] Here, the ramified islands are observed at low substrate temperatures. They are of kinetic origin as a result of the competition between the lateral impingement rate to a step edge determined by adatom migration and the deposition rate and, on the other hand, by the edge and corner migration of single atoms along the growing island. At first glance, the ramified island growth based on the growth kinetics should work equally for triangular and square lattices. But the substrate symmetry plays a decisive role in the formation of the island morphologies.[81] The difference in island shape on triangular and on square lattices is explained by the higher barrier of edge migration on triangular lattices due to the presence of twofold-coordinated edge sites in the close-packed directions. Thus, on square lattices, the fabrication of ramified islands should be possible only at very low substrate temperatures, or be even inhibited for systems where the barrier of edge migration is lower than that of adatom migration.[87,88] This picture is consistent with the experimental observations; so far exclusively compact islands have been observed in metal epitaxy on substrates with square symmetry.[54,75,89–91] The only exception is the growth of Ag on Ni(100),[92] where dendritic step decoration has been observed on a substrate with square symmetry, but here the Ag islands exhibit a triangular symmetry.

However, the present system, copper on Ni(100), exhibits ramified islands although the substrate and the islands display plain square symmetry. The STM images uncover a shape transition of copper islands on Ni(100) at submonolayer coverages over a wide range of typical growth conditions. At substrate temperatures between 250 and 370 K and deposition rates between 6×10^{-5} and 3×10^{-2} monolayers/s, the small islands exhibit the expected compact shape while the islands exceeding a critical size of about 500 atoms are ramified. Because of the elevated substrate temperatures and the invariance of the transition on substrate temperature and deposition rate, a kinetic origin of the island shape can definitely be ruled out. As demonstrated below, the island ramification results from the compressive strain in the copper islands due to the positive lattice mismatch of the two metals. By ramification the islands increase their perimeter, where strain can efficiently be relieved through outward relaxation of the edge atoms.
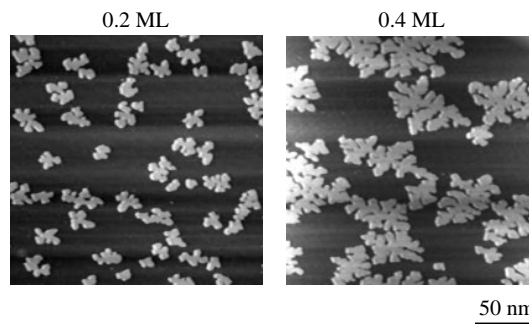

Fig. 11. Ramified island growth in submonolayer heteroepitaxy for monatomic high copper on Ni(100). The high substrate temperature of 345 K at the low deposition rate of 1.5×10^{-4} monolayers/s means that the islands are in an equilibrium configuration and their ramified shape is due to strain relief.
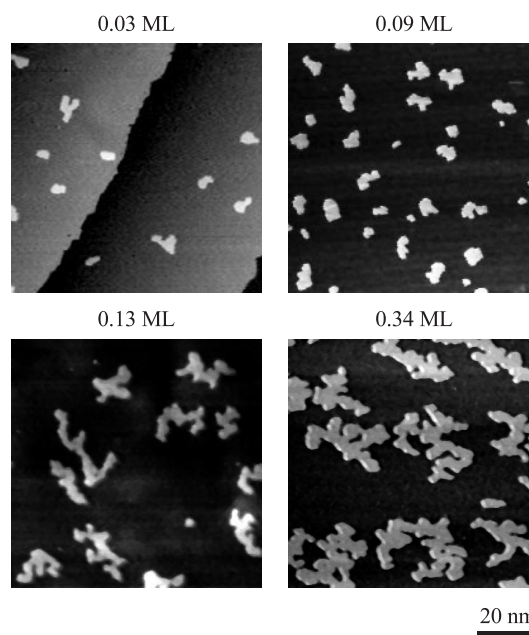

Fig. 12. Transition from compact to ramified island shapes at two different deposition rates (1.5×10^{-3} monolayers/s — images on the left hand side — and 6.3×10^{-3} monolayers/s — images on the right hand side) and a fixed substrate temperature of 345 K. The coverages are indicated.

Strained epitaxial islands are expected to be unstable against shape changes.[93–95] Analyzing the relation between strain energy and island shape in heteroepitaxial growth, Tersoff and Tromp[96] have predicted a spontaneous shape transition during growth of the coherently strained islands. Shape changes have been predicted to be a major

mechanism of strain relief. But, up to now, experimental evidence for strain-induced shape transitions of epitaxial islands has been rather scarce.[96–98] The concept was related first to the growth of three-dimensional, flat germanium pyramids with a rectangular basis on Si(001)[96,97] (cf. Sec. 5). Cu/Ni(100) is the first experimental verification of such a shape transition in the growth of single layer islands.

2.3.2. *Characterization of the island shape transition by STM images*

Examples of copper islands on Ni(100), which clearly show a noncompact shape, are displayed in Fig. 11. As pointed out, it is surprising to find ramified islands on a substrate with square symmetry. Edge migration rates of single atoms on substrates with square symmetry have been reported to be comparable to adatom migration rates,[87,88] and, therefore, compact islands are generally expected. In order to confirm the assumption that the ramified copper islands are not of kinetic origin, the substrate temperature and the deposition rate were varied systematically. A qualitative comparison for different growth conditions is given in Figs. 12 and 13. The images on the left hand side are obtained at higher substrate temperatures and lower deposition rates, respectively, and exhibit, therefore, a lower island density, whereas the images on the right obtained at lower substrate temperatures and higher deposition rates show a higher island density. The island shapes, however, depend only on the average island size and are not affected by the growth conditions. Small islands always have a compact shape. As they grow in size, their shape becomes noncompact. Almost all islands larger than the critical island size of about 500 atoms are ramified, and the very large islands even exhibit a preferential arm width of about 20 atoms. The step edges of the islands are preferentially oriented parallel and perpendicular to the substrate steps in the close-packed $\langle 110 \rangle$ directions. At substrate temperatures between 250 and 370 K the adsorbed copper atoms are shown to be very mobile on terraces and at step edges.[37] This temperature range even includes a transition in the critical nucleus from $i = 1$ to $i = 3$ which is associated with dimer bond breaking.[37] Therefore, the growth kinetics does not establish the ramified island shape, and we can conclude that the island shapes correspond to an equilibrium configuration.

This "equilibrium" configuration is not the thermodynamically stable one, since alloy formation is not active below 400 K. Experimentally, the onset of alloying is demonstrated by annealing the sample at 450 K. The STM images of Fig. 14 show that
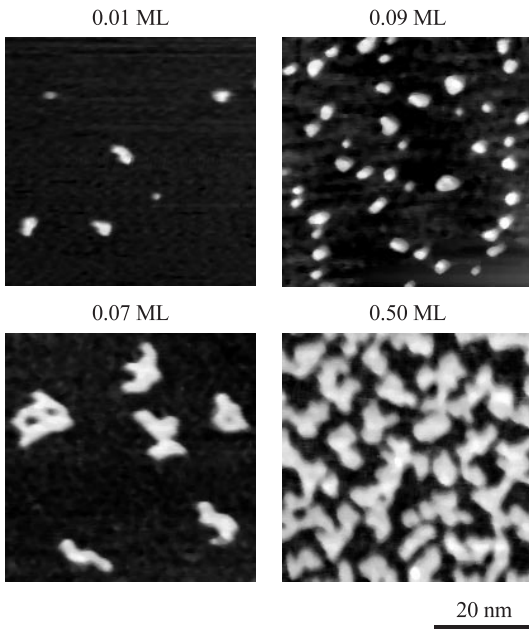
0.01 ML   0.09 ML

0.07 ML   0.50 ML

20 nm

Fig. 13.   Transition from compact to ramified island shapes at two different substrate temperatures (345 K — images on the left hand side — and 250 K — images on the right hand side) and a fixed deposition rate of 1.5×10^{-3} monolayers/s. The coverages are indicated.

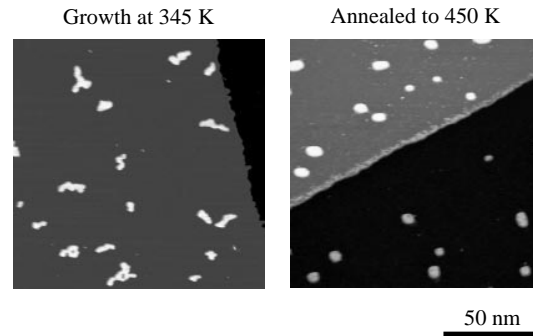Growth at 345 K   Annealed to 450 K

50 nm

Fig. 14.   STM images of islands and step edge for a 0.04 monolayer copper film on Ni(100) before and after annealing to 450 K, demonstrating the effect of surface alloying on the monatomic islands and decorated step edges. The substrate temperature during the epitaxial growth was 345 K and the deposition rate 6×10^{-4} monolayers/s.

at substrate temperatures, where the islands are not yet dissolved, exchange processes between the copper atoms of the islands and the nickel atoms of the substrate occur. The intermixing becomes not only evident on the islands, but also even clearer at the step edges, which are straightened and whose rims are imaged higher and spotted. The rims are not abruptly separated from the nickel substrate and a rather irregular interface is formed. The islands are imaged with the same height and exhibit a similar spotted surface, and hence should also consist of a randomly mixed copper–nickel alloy. Since the nickel atoms incorporated into the islands are smaller than the copper atoms, the strain energy of the islands is significantly reduced[99] and, consequently, compact islands form. Note that the islands shown in Fig. 14 contain up to about 1000 atoms.

2.3.3.   *Quantitative analysis of the island shapes*

The shape of islands without and with symmetry elements can be characterized by the fractal dimension of the islands. For example, one can determine the radius of gyration and the size of each 2D island. From a series of data plotted in a double-logarithmic fashion, the fractal dimension is easily extracted. For compact islands such as circular ones, the radius of gyration scales with the square root of the size, so that the fractal dimension is 2 (2D growth). A chain made up of single atoms, the most "open" island structure gives rise to a fractal dimension of 1, or 1D growth. Hence, the single layer 2D copper islands have a fractal dimension between 1 and 2.

The independence of the island shape from the growth conditions, as already qualitatively shown by the STM images in Figs. 12 and 13, is quantitatively confirmed by the analysis of more than 3000 islands grown at very different substrate temperatures (250–370 K) and deposition rates ($6 \times 10^{-5} - 3 \times 10^{-2}$ monolayers/s). Figure 15 demonstrates that the data scatter around a curve close to a fractal dimension of compact islands. Since the linear fit in the double-logarithmic plot has to include the monomer, one may choose only one fit parameter, which is the inverse fractal dimension. The fit, which includes island size variations of more than four orders of magnitude, leads to a fractal dimension of 1.889 ± 0.002. These rather compact island shapes

can be recognized in the STM images of Fig. 11. Even for very large islands, the arms are separated only by narrow channels. This quantitative analysis substantiates the previous statement that the island ramification cannot be understood in terms of a fractal growth mode of kinetic origin.

Because of the occurrence of these narrow channels, the evaluation of the island perimeter p as a function of island size A is more helpful for gaining insight into the physics behind the island shape transition, since the perimeter-to-size ratio of the strained copper islands is energetically relevant (see below). It is displayed for the same islands as used for the presentation in Fig. 15 as a double-logarithmic plot in Fig. 16. Islands of less than 300 atoms always exhibit a compact shape (2D growth). Their perimeter scales with the square root of the island size. For larger islands a deviation from this behavior is observed, and the dependence cannot be described in simple analytical terms, until for island sizes exceeding about 3000 atoms, the island perimeter is found to be directly proportional to the island size (1D growth). This behavior can be modeled by the growth of a linear chain with a certain arm width w. Using this model, the arm width is obtained fitting the data for the islands, which exceed the critical island size to
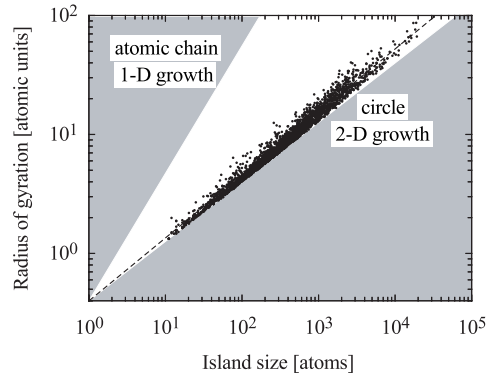
$$p = \frac{2A}{w} + 2w. \qquad (10)$$

Fig. 15.   Double-logarithmic plot of the islands' radius of gyration versus island size, demonstrating the coincidence of data obtained at different substrate temperatures (250–350 K), different growth rates (3×10^{-5}–3×10^{-2} monolayers/s) and different coverages (0.06–0.66 monolayers). Each dot represents one island. The forbidden regions are shaded gray; the upper limit is given by a one-atom-wide chain; the lower limit is an island of circular shape.
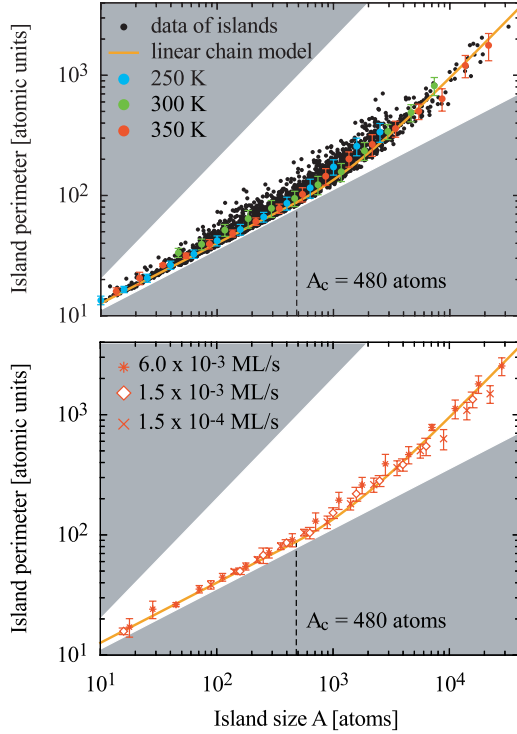
Fig. 16.   Island perimeter p versus island size A for sub-monolayer copper islands on Ni(100) obtained from the same islands as presented in Fig. 15. The gray-shaded areas are forbidden regions; the lower limit of the allowed region corresponds to circular islands and the upper limit to one-atom-wide chains. The colored dots are averaged data displayed with their statistical error bars. The upper part includes the substrate temperature variation and the lower one the average values for different deposition rates. The data are compared with the linear chain model, where $p = 2A/22 + 2 \times 22$ (solid line, in orange).

Since $p(A)$ is given by the experimental data, the arm width w is the only fit parameter. Several fits for island sizes above the critical value were performed and gave almost identical results. Using the data of the island sizes above 1000 atoms, one obtains $w = (21.98 \pm 0.25)$ atoms, whereas for island sizes above 400 atoms, $w = (21.87 \pm 0.18)$ atoms. The arm width $w = 22 \pm 1$ is thus almost independent of the starting point. The critical island size, extracted with the linear chain model, is therefore $A_c = w^2 = (480 \pm 20)$ atoms.

2.3.4.   *The influence of strain on the island shape*

Tersoff and Tromp[96] have analyzed the energy of coherently strained, i.e. dislocation-free, hetero-epitaxial islands as a function of their size. They have considered 3D, pyramidal islands of width W, length L and height H on a square substrate. The height, however, is considered to be much smaller than the width and length. Minimizing the total energy, including the excess surface and strain energy, they have predicted a spontaneous shape transition at a certain island size. Small islands have a compact, symmetric shape while above the critical island size they become elongated for a better strain relaxation. While only the simple rectangular shape was studied, the basic result should be applicable also to the ramified shape of the single layer copper islands on Ni(100), particularly if the arm length substantially exceeds its width. With respect to a rectangular island with width W, the branching of the ramified islands with arm width w does not affect the perimeter for a given island size.

The model of Tersoff and Tromp[96] is based on different assumptions:

(1) Corner effects are totally neglected, since kink sites are energetically unfavored and occur, therefore, infrequently.
(2) The surface energies of the substrate and of the islands are assumed to be equal.
(3) The strain of the islands does not significantly change perpendicular to the substrate surface.

These assumptions are not severe limitations on the applicability of that theory on copper on Ni(100):

(1) Owing to the preferential orientation of the island step edges in the close-packed directions, corner effects are weak.
(2) The surface energies of Cu(100) and Ni(100) are almost identical.[100,101]
(3) For single layer islands the strain cannot change perpendicular to the surface by definition.

Hence, the approximations made by the assumptions of Tersoff and Tromp are applicable to the Cu/Ni(100) system much better than to spontaneous shape transitions in any other system. Therefore, Cu/Ni(100) is an appropriate system for confirming the predictions of the theory in a quantitative manner.

In the model, the normalized energy E given by the excess surface energy and the change in strain energy due to elastic relaxation is

$$E = b(W + L) - W \cdot \ln L - L \cdot \ln W. \qquad (11)$$

Here, b is supposed to be a constant related to the elastic properties of film and substrate material. Since the island size $A = WL$, one finds that

$$E = b \left(W + \frac{A}{W} \right) - W \cdot \ln \left(\frac{A}{W} \right) - \frac{A}{W} \cdot \ln W \,. \tag{12}$$

The minimization of E with respect to W results in two identical solutions below a critical island size A_c: $A_c = \exp(2b + 4)$. Above A_c, however, it leads to different solutions. The width W shrinks from the width at the critical size $W_c = \exp(b + 2)$ to a width of an infinite island. The development of W as a function of island size is given in Fig. 17.

Because the width and the length cannot be directly measured due to the ramified island morphology and the existence of two equivalent close-packed directions, the values have been derived from the island perimeter and the island size assuming a
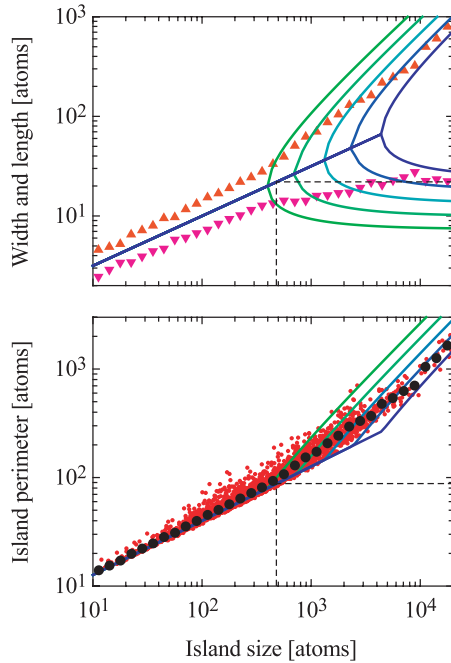

Fig. 17. Comparison between the model of Tersoff and Tromp, Eq. (12) with $b = 1.0, 1.3, 1.6, 1.9, 2.2$ (lines colored from green to blue), and the experimental data. An increase of the constant b shifts the shape transition to higher island sizes. In the upper part width W and length L are derived from the island perimeter p and island size A assuming a rectangular island shape and compared with the prediction from the model. The lower part contains the data shown in Fig. 16 (small red dots) and the values averaged within a certain size interval (black dots).

rectangular island shape. Up to the critical island size both width and length grow with the square root of island size as valid for compact islands (2D growth). Above the critical island size they show the predicted split, whereas the width does not shrink but reaches a constant value. The discrepancy between theory and experimental data is due to the particular, ramified shape of the 2D islands. The model, a quasi-1D description, does not account for the growth in two equivalent directions and for finite size effects at the ends of the arms. Although the shrinking of the arm width is not present in the quantitative data of Fig. 17, it is observable in Fig. 11. The island on the upper left of Fig. 11(a), for example, shows a clover-leaf-like structure, since only the inner part of the island develops the reduced arm width. The larger islands [cf. Fig. 11(b)] are, therefore, also almost compact, only narrow channels are formed, and the distances between neighboring channels are thinner in the center of the island than in the outer part. This outer part, however, dominates $p(A)$ even for the largest islands, so that shrinking is not present in the data of Fig. 17. Hence, the transition for Cu/Ni(100) may be described better by $b = 1.1$ although higher values, e.g. 2.0, give a closer fit to the data. A value of $b = 1.1$ leads to $A_c = 500$ atoms, $W_c = 22$ atoms and $W_\infty = 8$ atoms. These quantities are confirmed by the STM images: 500 atoms is, indeed, the critical island size, 22 atoms the critical arm width, and the arms in the center of an island exhibit a width of approximately 8 atoms. A reason that this behavior is not found for each island in a similar manner is the weak driving force for diffusion because of the flat energy minimum. Therefore, the phenomenon is understood rather by the continuous transition between 2D and 1D growth whereas the model predicts a sharp transition at the critical island size. The equilibrium theory in the present state does not include the marginal effects in 2D island growth and fails in the quantitative description of these data. Nevertheless, the theory correctly predicts the shape transition between 2D and 1D growth of single layer copper islands on Ni(100) due to lattice strain.

2.3.5.   *The relaxation of edge atoms*

The driving force for the observed preferential arm width and thus for the ramification of the copper
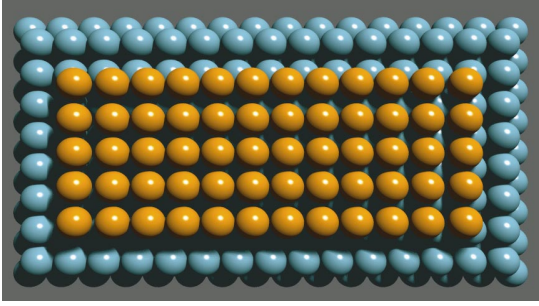
Fig. 18.   Hard sphere model of a relatively small copper island on Ni(100) illustrating, with an exaggeration by a factor of 30, edge atom relaxation of compressively strained heteroepitaxial islands. The values for the outward relaxation are obtained from effective medium theory calculations performed by H. Brune.

islands on Ni(100) is associated with the positive lattice mismatch for copper on nickel. The larger lattice constant of copper forces the atoms to shift outwards from the center of the islands. This behavior is especially important for the step edges, since the step edge atoms are bound only to one side and, therefore, rather free to relax outwards. They may more easily follow their natural lattice spacing. On the other hand, the lower coordination of the edge atoms favors a size-dependent inward relaxation,[102] since less coordination tends to shrink bond lengths. In general, these two effects compete, and it is *a priori* difficult to determine the dominant term. Therefore, calculations using effective medium theory (EMT)[88] have been performed by H. Brune to determine the dominant term for copper islands on Ni(100). They reveal a significant outward relaxation of the edge atoms, confirming the dominance of strain effects. The result for a relatively small rectangular island is visualized by a hard sphere model in Fig. 18.

The observation that the ramification of the islands involves preferential growth along the close-packed directions indicates that there is high mobility along the edges. Kink sites are energetically unfavorable. Both indications are corroborated by the EMT results. As for other square lattices, the barrier for edge migration (0.29 eV) is found to be lower than that for monomer migration on terraces (0.47 eV) and the barrier for corner crossing (0.53 eV) is only slightly larger. Kink sites are energetically costly since they reduce coordination while leaving the number of edge atoms constant. Corner sites, however, are not very stable because these

atoms are relaxed outwards with respect to both close-packed directions, giving rise to rounded corners. The formation of a constant arm width also implies that the island growth becomes anisotropic and atoms attached sideways diffuse towards a tip.

The conclusion that ramification of islands is caused by the outward edge relaxation of copper atoms on Ni(100) due to the compressive strain is supported by the fact that copper forms ramified islands on Ni(100) but not on Pd(100),[90] although the two substrate materials are very similar. The copper islands are compressively strained on Ni(100) and exhibit tensile strain on Pd(100) due to the positive and the negative misfit, respectively.

In addition, high resolution low energy electron diffraction measurements confirm the outward relaxation of atoms at step edges of copper islands on Ni(100).[103]

2.3.6.   *Island shape analysis for the determination of strain energy*

The equilibrium shape of a heteroepitaxial island is understood as a result of the energy balance of the atomic bond energy within the islands and the strain energy due to the lattice mismatch with the substrate. Therefore, one can estimate the strain energy by the evaluation of the bond energy difference between the observed ramified islands and square islands of identical size. On the one hand, the islands try to attain compact shapes to optimize their binding energy. On the other hand, the strain energy associated with the island relaxation favors ramification. Based on the simple bond counting, atoms inside of an island have four nearest neighbors in the adlayer, i.e. they are associated with two bonds per atom, whereby edge atoms have only three nearest neighbors in the adlayer associated with 1.5 bonds per atom. Therefore, the binding energy of an island corresponds to $(2A - p/2)E_b$, where A and p are expressed in the number of atoms forming the island and its perimeter, respectively. The binding energy per atom is, therefore, $(2 - p/2A)E_b$. For a square island, $p = 4\sqrt{A}$, and the bond energy per atom is given by $(2 - 2\sqrt{A})E_b$. For the ramified islands, however, we have found that $p = 2A/22 + 2 \times 22$, which results in a bond energy per atom of $(2 - 1/22 - 22/A)E_b$. Hence, in the bond counting model, for large islands, the energy gain of forming

square-shaped with respect to ramified islands, E^*, is 1/22 of the dimer bond energy per atom.

The dimer bond energy has been derived from the Arrhenius behavior of the island density in the saturation regime, when the size of the critical nucleus is larger than 1. On the basis of this value, $E_b = (0.34 \pm 0.03)$ eV, the energy gain E^* corresponds to (15 ± 2) meV per island atom. This value is comparable to strain energies calculated from bulk properties. Since 15 meV is a relatively small energy, it is reasonable to assume that the difference is overbalanced by the energy gain associated with the more effective strain relief at the longer edges of ramified islands. On the other hand, it is high enough to explain that the arm width is constant over the wide temperature range between 250 and 370 K.

2.3.7. *Shape transition and nanostructure formation*

Strain relaxation at the edges of copper islands on Ni(100) drives a transition from compact to ramified islands at a critical island size. The ramified islands exhibit a preferential arm width. This phenomenon, predicted theoretically by Tersoff and Tromp,[96] should be of general importance in heteroepitaxy on square lattices with a positive lattice misfit. Thus, the ramified islands can be prepared not only at rather low substrate temperatures by kinetic processes but also at rather high substrate temperatures by thermodynamics. While thermodynamics embodies the essence of the behavior of the adlayer/substrate system at equilibrium, kinetics controls the pathway of the system towards an equilibrium state within the thermodynamic restrictions. These limitations reduce drastically the variety of nanostructures, which can be tailored by the choice of the growth conditions. The present system gives an example of thermodynamic limitations: The ramified island growth at submonolayer coverages due to the lattice strain in heteroepitaxy cannot be outwitted by the choice of substrate temperature and deposition rate. On the other hand, one can employ this phenomenon to realize particular nanostructures even at rather high substrate temperatures. These nanostructures, which represent an equilibrium state of the heterosystem, should be quite stable because they are formed within a very large range of growth conditions.

2.4. *Strain relief via stripe formation*

The strain relief by island ramification operates only until the first monolayer is filled by islands with arms 22 atoms wide and narrow channels in between. Therefore, one expects that the complete first and the subsequent copper layers are not only homogeneously strained but contain certain structural defects. Such defects should also be present at submonolayer coverages. Indeed, already at coverages of 0.3 monolayers, there exist some islands about 40 atoms wide, which exhibit long protruding stripes traversing the entire island (cf. Fig. 19). These one-atom-wide stripes with a height of 1/3 of the atomic step are described by a new model of strain relief below.
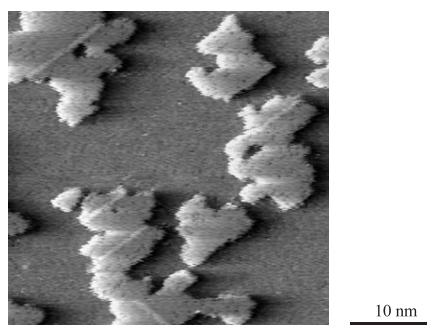

Fig. 19. Stripe formation on strained copper islands grown on Ni(100), coverage 0.36 monolayers.

2.4.1. *Strain relief in submonolayer heteroepitaxy on substrates with square symmetry via stripe formation*

The lattice mismatch between film and substrate material leads to strain in the film until the film has adopted its bulk structure through the formation of strain-relieving defects. In the widely accepted classical "Matthews picture" the adlayer is locked to the substrate up to a finite critical thickness.[104–108] Below the critical thickness h_c the film grows essentially pseudomorphic. Above h_c the strain is relieved by means of misfit dislocations and associated lattice relaxation. The critical thickness is determined by the elastic constants of both materials and their misfit. For copper on nickel, a critical thickness h_c of 1.1 nm was calculated.[105] This concept is a continuum model ignoring atomic details of the interface structure. Indeed, it has recently been found to fail in the description of hexagonal close-packed
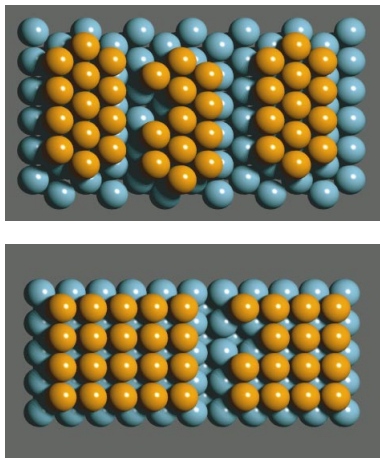
Fig. 20. Island formation on substrates with hexagonal and square symmetry.

metal interfaces.[109–112] This failure is related to the particular structure of fcc(111) surfaces with two favorable adsorption sites. The threefold-coordinated hollow fcc and hcp sites have similar adsorption energy. Compressive and tensile strain at metal and semiconductor interfaces can easily be accommodated at domain walls by the formation of fcc–hcp stackings, as schematically shown in Fig. 20. As a result, one can observe zigzag-striped and triangular patterns. The low energy cost for the formation of these misfit defects essentially drops the critical thickness to zero or just to the first monolayer.[109–112]

Such a stacking fault mechanism, however, is impossible at square interfaces, because there are no different adsorption sites of similar energy (cf. Fig. 20). For these interfaces many experimental studies have been reported which seem to be in agreement with the predictions of the Matthews picture.[113] In particular, an Auger electron diffraction study of copper growth on Ni(100) seemed to provide quantitative support of the continuum model.[31] Chambers *et al.*[31] interpreted their data in favor of a pseudomorphic growth up to a critical thickness of eight monolayers, which is indeed the h_c value predicted for this system by the continuum model.

In the following, the discussion of the observed stripes proves that the continuum theory also fails for the description of copper growth on Ni(100), having an interface with square symmetry. A simple model has been developed which is based on the STM observations[114,115] (and which has been proved subsequently by high resolution low energy electron diffraction[116] and X-ray diffraction measurements[117–119]):

(1) Stripes occur at coverages as low as 0.25 monolayers, when the islands have reached a critical width of about 30 atoms. When the first monolayer is filled, the whole surface is covered by a stripe pattern (cf. Fig. 21).
(2) At submonolayer coverages the stripes are always one atom wide.
(3) The height of the stripes is about 1/3 of the atomic step.
(4) The stripes run parallel and perpendicular to the step edges in close-packed $\langle 110 \rangle$ directions.
(5) The stripes neither cross nor coalesce, and are best seen near monolayer coverage when a network of stripes is formed.
(6) Stripes occur only on islands more than about 30 atoms wide. On islands, their minimal length is found to be 10 atoms.

The model is motivated by the fact that the compressive strain at the fcc(100) surface is highest in the close-packed $\langle 110 \rangle$ directions. Removing an atomic $\langle 110 \rangle$ chain as shown in Fig. 20, the surrounding copper atoms can laterally relax outwards perpendicular to the $\langle 110 \rangle$ chain chosen. If one assumes a small outward relaxation of less than $\sim 10\%$, the atomic chain shifted by half a nearest neighbor distance can be put back, so that the atoms are located on twofold-coordinated bridge sites instead of the fourfold-coordinated hollow sites (cf. Fig. 22). Such a bridge site is unstable in homoepitaxial growth since the atoms at the ends can simply flip to the neighboring hollow site, where the number of nearest
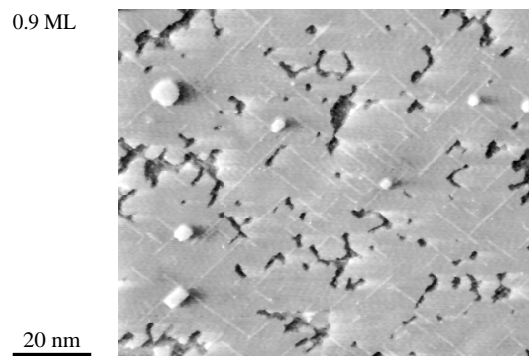

0.9 ML

20 nm

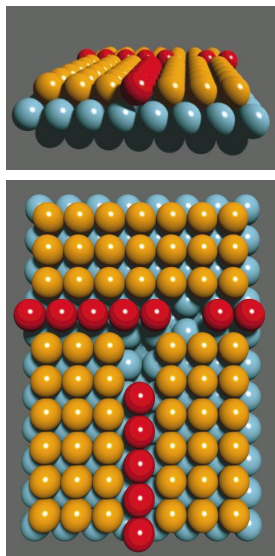Fig. 21. Formation of the stripe pattern for copper on Ni(100) by completion of the first monolayer.

Fig. 22. The two domains of bridge sites related to the [110] and [1̄10] directions make crossing of stripes impossible.

substrate atoms is four instead of two. In heteroepitaxy, where the compressive strain has to be taken into account, such a configuration is likely, since the protruding bridge site atoms and their neighbors gain lateral freedom of expansion and the film can partially relieve its strain. Furthermore, the reduced number of nearest neighbors in the substrate is somehow compensated by the gain of binding energy in the adlayer. Besides the two neighboring atoms within the stripe, there are four lateral neighbors with a binding length about 10% larger, an amount which is even reduced by the strain. Obviously, the total binding energy can even be higher by the increased lateral coordination.

In addition, a reduction of binding energy is not conclusive in heteroepitaxial growth, since the dimer bond energy within the adlayer can be larger than the binding energy between substrate and adlayer atoms. In particular, for the present system the dimer bond energy of 0.34 eV is larger than the Cu–Ni bond energy derived from the adatom migration (0.37/2 eV) considering only nearest neighbor interactions. Although this consideration is only a rough estimate, and also ignores any effect at the island edges, it demonstrates the complexity of defect formation in submonolayer heteroepitaxy even for simple systems.

The formation of the stripes by the shift of atoms from hollow to bridge sites is supported by the height measurement. The height of the stripes at submonolayer coverages is (0.06 ± 0.01) nm, in reasonable agreement with a simple hard sphere model, which yields a height of 0.04 nm.[114]

Because of the square symmetry of substrate and adlayer, the stripes have to form with equal probability in both ⟨110⟩ directions, which is indeed the case, as verified by the STM images. The facts that stripes neither cross nor coalesce is understood by the occurrence of two bridge site domains on the square fcc(100) surface. Two orthogonal stripes are always separated at their potential junction by 1/2 nearest neighbor distance, rendering crossing impossible. Coalescence is also unlikely as the distance between two parallel stripes is given by the lattice constant of the nickel substrate, and the merging of two stripes would block further transverse relaxation.

Stripe atoms at the step edge are rather unstable. Therefore, stripes of less than about eight atoms are rare.

Consequently, this recently proposed model accounts for all the experimental observations.

2.4.2. *Conclusion of submonolayer copper growth on Ni(100)*

The two strain relief mechanisms — island ramification and stripe formation — have in common the fact that they involve displacements of atoms from the ideal pseudomorphic hollow site. For very small islands the strain can be relieved at the step edges even if they have a compact shape. Larger islands become ramified to optimize the ratio between perimeter and island size. Finally, the stripes appear when the strain relief at the island edges is no longer sufficient for minimizing the total energy of the coherently strained islands. While the critical arm width is 22 atoms in the case of ramification, the typical island width for the onset of stripe formation corresponds to about 30 atoms.

2.5. *Multilayer growth of copper on Ni(100)*

2.5.1. *Internal faceting*

When the first monolayer is filled, the film exhibits a network of stripes. These stripes act as diffusion barriers and heterogeneous nucleation centers.[120] The islands in the second layer nucleate preferentially at

the stripes. Their shape is almost perfectly rectangular, even if their width or length exceeds 30 atoms. Nevertheless, the larger islands of the second layer contain stripes, too.[114] The stripes are now two
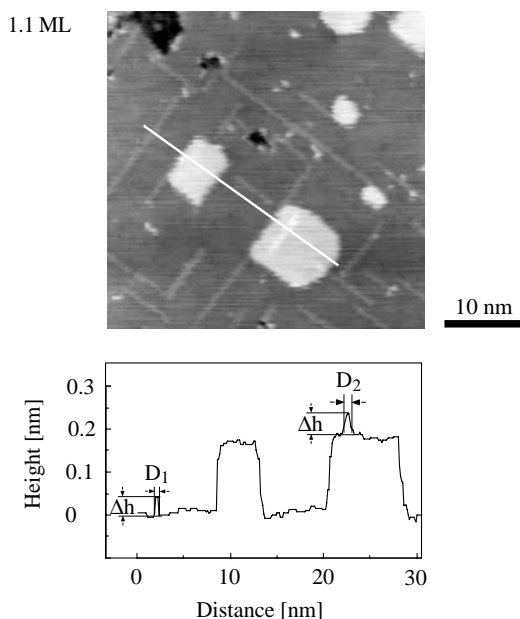
1.1 ML

10 nm

Fig. 23.   Formation of the second copper layer on Ni(100).
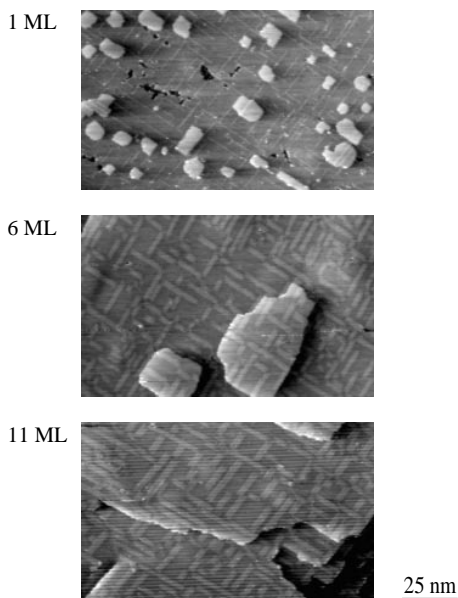
1 ML

6 ML

11 ML

25 nm

Fig. 24.   Evolution of the stripe pattern with film thickness. The films are grown at a substrate temperature of 345 K and a deposition rate of 1.5×10^{-3} monolayers/s. The coverages are indicated.
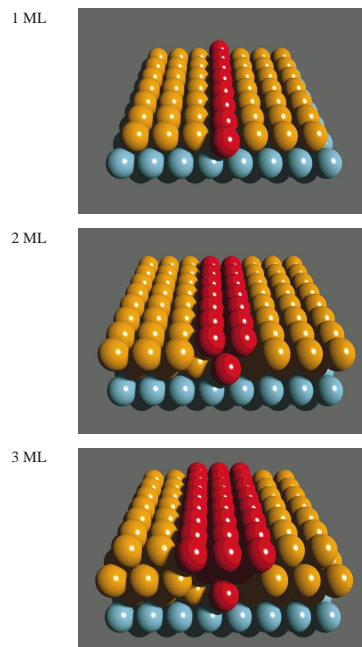
1 ML

2 ML

3 ML

Fig. 25.   Stabilization of the stripe pattern by internal faceting.

atoms wide but their height equals that of the stripes on the first monolayer, as demonstrated in Fig. 23.

Figure 24 shows the evolution of the stripe pattern with the film thickness. The stripes become wider; their height and their density remain constant.

This scenario is reproduced by the internal faceting model shown in Fig. 25.[114,115] It demonstrates the growth of the protruding stripes up to a coverage of three monolayers. The height Δh is constant for all coverages. The width D_i grows stepwise with the coverage until the stripes adjoin. For monolayer coverage the stripes are exactly one atom wide, for two monolayers two atoms wide, and so on. The stripe density and the length distribution are determined by the monolayer configuration. The subsequent growth stabilizes the stripe pattern by the formation of internal {111} facets along the stripes and {110} facets at both ends. This mechanism is energetically favorable because the strain relaxation takes place by the formation of highly stable, close-packed {111} facets.

To demonstrate that the internal {111} faceting model is in quantitative agreement with the experimental observations, the height, width and mean length of the stripes versus coverage are represented
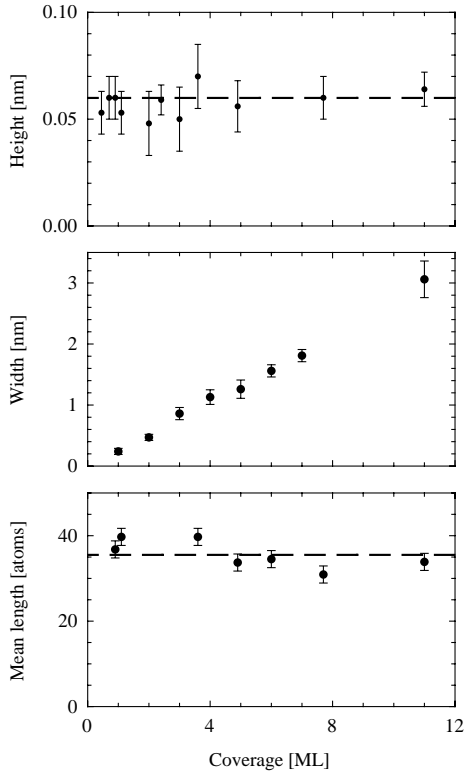
Fig. 26.   Quantitative analysis of height, width and mean length of the stripes with coverage.
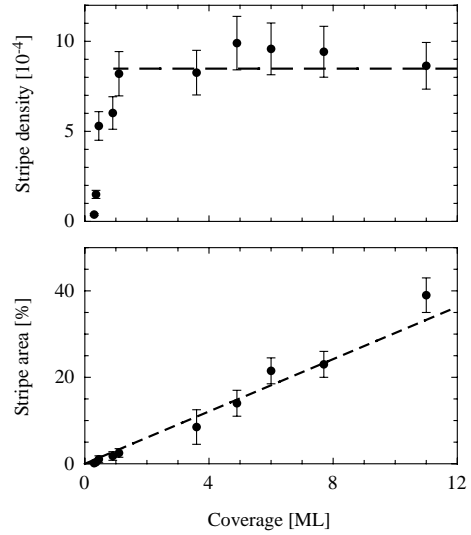

Fig. 27.   Quantitative analysis of stripe density and area with coverage. The dashed line in the lower graph is not a linear fit but the curve derived from mean length, stripe density and stripe width.

in Fig. 26. Indeed, the height of the stripes $\Delta h = (0.06 \pm 0.01)$ nm is constant for coverages of up to 17 monolayers.

The width grows stepwise, as expected from the model. Note that the stripe width is corrected by a constant value, taking into account the finite imaging width of the STM tip on metal surfaces. Monatomic copper chains are usually imaged with a width of 0.5–0.8 nm.[121] Here, however, the stripe atoms protrude only by 1/3 step height, and hence the width of the monatomic chain was just about 0.4 nm.

Above monolayer coverage, when the stripe network has been formed, the mean length of the stripes $\langle s \rangle$ remains constant, (35.6 ± 3.3) atoms, independent of film thickness.

As shown in Fig. 27, the density of stripes ρ is likewise constant, $(8.2 \pm 1.8) \times 10^{-4}$ per substrate atom, for coverages between 1 and 17 monolayers. Thus, the surface area covered by the stripes, as deduced directly from the STM images, has a linear dependence on film thickness. The dashed line is not the linear fit, but represents the dependence derived from the mean length, the stripe density and the

stripe width to demonstrate the consistency of the data. The quantitative analysis of the images reveals that the density of the stripes as well as their mean length and length distribution are determined by the monolayer configuration. The distribution of stripe lengths can be described by an exponential law:[115]

$$N_s(s) = \frac{\rho}{\langle s \rangle - s_{\min}} \exp\left(\frac{s - s_{\min}}{\langle s \rangle - s_{\min}} \right) . \qquad (13)$$

The minimum stripe length $s_{\min}$ derived from the experimental data corresponds to eight atoms. Stripes of less than eight atoms seem to be energetically unstable. Of course, longer stripes are more stable. The length of the stripes is finite as a result of the geometric arrangement in $\langle 110 \rangle$ directions with equal probability and the forbidden crossing of orthogonal stripes because of the two different domains.

The exponential length distribution, the stripe density, and the mean length of the stripes do not change with the variation of deposition rate (10^{-3}–10^{-2} monolayers/s), substrate temperature (200–400 K) or coverage (1–17 monolayers). This behavior indicates that the stripe network is related to a minimum of the total energy of the strained thin film and not determined by the growth kinetics.

As a result of the intermixing of copper and nickel, the stripes disappear after annealing of the sample above 550 K. After annealing, the surface seems to be homogeneous. However, if the film is

Growth at 350 K (12 ML)
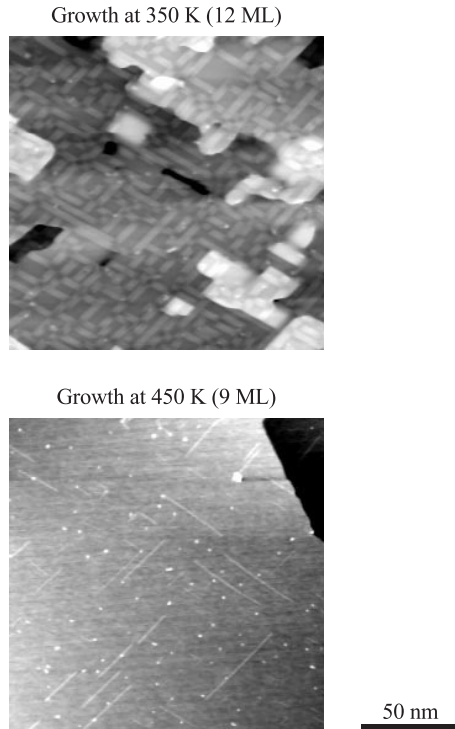

Growth at 450 K (9 ML)

50 nm

Fig. 28.   Formation of long monatomic stripes associated with a considerable reduction in stripe density. Substrate temperatures and coverages are indicated. The deposition rate was 6×10^{-3} monolayers/s for both samples.

grown at substrate temperatures of 450 K, one finds a reduced stripe width and density associated with very long stripes, as shown in the lower part of Fig. 28. For comparison the upper part of the figure exhibits the typical stripe density for the growth at lower substrate temperature. In the lower part the density is reduced by one order of magnitude, and the stripes are only one atom wide although one expects a width of nine atoms at the coverage of nine monolayers. This behavior indicates that the intermixing process starts from the interface as the growth proceeds. Stripes in the top layer, however, are stable. The increased mean length of the stripes and the reduced stripe density show that longer stripes are more stable than smaller ones, as expected.

2.5.2.   *Concurring model for misfit accommodation: inclined stacking faults*

Another mechanism, very similar to the internal faceting, has been proposed to describe the occurrence of the stripe pattern.[122] The model is based

on the following scenario. A single adatom should be placed at a highly coordinated hollow site. As the growth proceeds, adatoms interact with the first one and form islands. If the bulk lattice parameter of the deposited atoms a_d is slightly larger than that of the substrate material a_b, as for copper on nickel, neighboring atoms in the film may be shifted out of the exact hollow position. For stiff interactions in the film material and smooth substrate potential, one can imagine that the complete monolayer film tends to have its bulk lattice constant. Consequently, an integer number of film atoms with their larger size can fit another integer number of substrate atoms. The best accommodation is obtained for an integer number $M = 1/m$, where $m = (a_d - a_b)/a_b$ denotes the lattice mismatch. Thus, the density of "perfect" sites is $\rho = 1/m^2$, a value with is indeed equal to the observed stripe density. Furthermore, this "Henzler" model also provides the appropriate height for the stripes of the 1/6 lattice constant. The model is based on a strong bonding within the film, obviously valid for the present system, where the dimer bond energy is comparable with the migration barrier. Although the "Henzler" model of inclined stacking faults can explain the stripe density, a quantity which is not derived from any other model, it fails for Cu/Ni(100). The Auger electron diffraction data of Chambers *et al.*[31,114] do not show full relaxation of the copper film.

Although the internal faceting model successfully describes the diffraction data of Chambers *et al.* (in contrast to the model applied by the authors), very recent studies based on surface X-ray diffraction yield an even more detailed scenario of strain relief. These studies confirm the internal faceting model for copper on Ni(100) and give a detailed insight into the relaxation behavior of the copper film. Rasmussen *et al.*[117–119] have proved not only the occurrence of internal {111} facets but also the shift of the stripe atoms by half a nearest neighbor distance. Their measurement of the constant stripe height (0.05 nm) agrees well with the STM and spot profile analysis of low energy electron diffraction[116] as well as with the hard sphere model.[114] Since synchrotron X-ray diffraction also yields information about deeper film layers, Rasmussen *et al.*[118,119] were able to detect the suggested lateral relaxation of the copper atoms within the stripe as well as the formation of pseudomorphic copper in between. Furthermore, the

vertical lattice spacing of copper in the wedges as well as between them can be extracted using an appropriate model. Rasmussen *et al.*[118,119] found that during the first few layers the copper in the wedges is laterally fully relaxed to the copper bulk spacing and pseudomorphic in between. For thicker films, however, the strain increases with the height above the interface. Surprisingly, the vertical spacing inside and outside the "huts" is equal and expanded relative to the nickel constant by 4%. Thus, the vertical translation of the huts is identical for all coverages of up to about 20 monolayers. The value of 0.05 nm agrees well with the models discussed.

This explanation of the X-ray diffraction data also explains the Moiré fringes seen many years ago in transmission electron micrograph images of copper films on Ni(100),[28,31] which are not understood by the continuum model. The difference between relaxed copper on the one hand and pseudomorphic copper and nickel on the other hand naturally explains the appearance of Moiré fringes seen in transmission electron microscopy of four-monolayer-thick copper films on Ni(100), a coverage which is well below the critical thickness for the film relaxation by the introduction of strain-relieving defects.

Note that the stripe atoms near the interface use almost all the extra space available by the shift of atoms, resulting in a considerable relaxation of 7%.[118] Away from the interface the relaxation becomes smaller and smaller, so that for coverages of about 20 monolayers the topmost layer shows the lattice constant of bulk nickel, although usually the copper film should tend to its natural spacing. In that way the strain relaxation of copper on Ni(100) is unusual.[118] Nevertheless, similar stripe patterns on flame-annealed polycrystalline gold foils[123] and on KCl/NaCl(100)[122] underline the generality of the internal faceting model. The natural formation of internal nanoscale clusters seems to play a rather general role in heteroepitaxy.

2.5.3. *Formation of a complex dislocation network in copper films on Ni(100)*

As already pointed out, the internal faceting mechanism works only until the film reaches a thickness of about 20 monolayers. At this critical film thickness, the topmost copper layer within and between the stripes (huts) exhibits the nickel spacing, and,
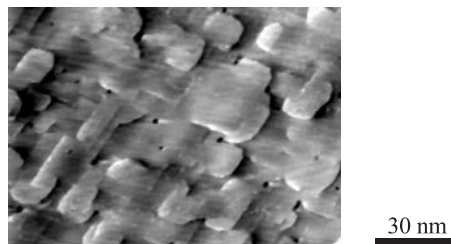

Fig. 29. STM image of a dislocation network formed after deposition of 24 monolayers of copper on Ni(100).
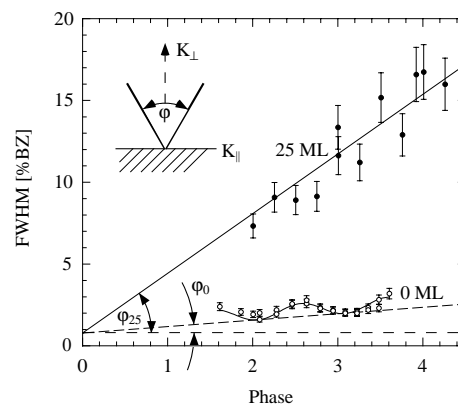

Fig. 30. Experimental determination of the mosaic spread for a 25-monolayer-thick copper film grown on Ni(100). The formation of dislocations results in a significant mosaic spread of 1.32° (solid line). The mosaic spread of the nickel substrate itself is found to be 0.16° (dashed line). The oscillatory behavior is due to the atomic steps on the substrate. (From Ref. 116.)

perhaps more important, neighboring and orthogonal stripes merge. The strain relief mechanism becomes ineffective. Consequently, another type of strain relief arises, as shown by the STM image in Fig. 29. The surface exhibits a patchwork of tilted microterraces. Therefore, one can assume that the stripes rearrange in such a way that they tilt when they merge.

The merging of parallel stripes is already observed at coverages as low as 10 monolayers. Here, the structure is almost unaffected; only the width of merging stripes becomes smaller. At coverages of 17 monolayers, the STM images show very few tilted microterraces. At 24 monolayers, the film fully consists of these tilted terraces.

The formation of tilted terraces is also observed by electron diffraction measurements at different film

thicknesses. From the analysis of the scaled peak intensities in low energy electron diffraction patterns, a critical coverage of about 18 monolayers is found.[116]

High resolution LEED measurements are used to deduce the average mosaic spread of a 25-monolayer-thick copper film.[116] The tilted microterraces cause a broadening of the Bragg rods into cone-shaped bunches which is observed in energy-dependent diffraction patterns.[124] The mosaic angle is found to be 1.32° (see Fig. 30). Assuming dislocations of monatomic height, the dislocation density or microterrace density corresponds to the stripe density. This result indicates that the internal hut clusters are quite stable.

2.6.   *Conclusion*

Although copper and nickel are elements with very similar physical and chemical properties, the relatively small misfit of 2.6% results in unexpected defect structures even at submonolayer coverages. Since the island density is mainly determined by the very early stages of growth at coverages below 0.1 monolayers, the nucleation can be described as for homoepitaxial systems. The sizes of the critical nuclei, which are closely related to the scaling exponents, are consistently determined by nucleation theory and scaling theory. This result has never been experimentally confirmed with such a precision as for the present system. The quantities obtained from the experiments, i.e. the barrier for adatom terrace migration, the related attempt frequency as well as the dimer bond energy, all assume reasonable values. The ramified shape of larger islands at submonolayer coverage is the result of the competition between surface Gibbs energy and strain energy. The relatively large dimer bond energy derived is used to explain the occurrence of the internal faceting, a mechanism of strain relief uncovered and verified recently.

The relaxation of lattice strain at interfaces with square symmetry can be much more complex than expected. The continuum approach completely fails to describe the strain relief scenario at the Cu/Ni(100) surface. This failure is not unusual. Atomic scale surface probes such as scanning tunneling microscopy give unprecedented insights into growth phenomena on the atomic scale, as shown here, and will continue to provide unexpected results. For sure, atomistic details have to be considered in an appropriate modeling of interfacial structures.

3.   Molecular Beam Epitaxy of Para-Hexaphenyl on GaAs Surfaces

3.1.   *Para-hexaphenyl on GaAs — a "complex" system*

The system treated in the section above, copper on Ni(100), is of fundamental interest. Systems of technological relevance are usually more complex. Especially, semiconductors exhibit more or less complicated surface reconstructions, depending on the surface orientation, substrate temperature and deposition rates of the constituents. A prominent example is GaAs(001), which exhibits a sequence of the surface reconstructions dependent on the substrate temperature and As/Ga deposition rate ratio.[125,126] This dependence is often illustrated by the surface phase diagram, i.e. the As/Ga ratio versus substrate temperature as an Arrhenius plot. The main features are the Ga-rich 4×2 reconstruction, a transition region (3×1 or 1×1) and the As-rich 2×4 reconstruction. The surface phase diagram is used to control the growth conditions and to characterize them in comparison with other groups. From a technological point of view, the As-rich (2×4)-reconstructed surface is dominant because thin film structures are frequently grown under these conditions, where (opto)electronic properties are optimized. The (2×4)-reconstructed surface, intensively studied theoretically and experimentally, occurs in three phases related to As coverages between 0.5 and 1 monolayers.[127–129] However, the α, β and γ phases show only slightly different electron diffraction patterns. They are based on As dimers without exception. Therefore, the precise structure seems to be of minor importance for island nucleation.

Symmetries and anisotropies of substrate and islands have to be taken into account for an appropriate description of island formation, because the basic interactions during island formation, such as terrace migration and aggregation, are affected. The regime of condensation discussed for copper on Ni(100), i.e. complete condensation of 2D islands, is rather an exception, since the condensation can be also incomplete and often 3D islands form. Nevertheless, nucleation theory predicts in all cases of

well-defined critical island sizes an Arrhenius be-
havior of the island density and a power law for
the rate dependence of the island density.[41] This
statement is supported by the present system: para-
hexaphenyl on GaAs. One may assume that a rela-
tively large molecule such as para-hexaphenyl does
not form any well-defined epitaxial island on such
a complex substrate as GaAs, but rather randomly
shaped conglomerates with many defects, since the
lattice constant and crystal structure differ dras-
tically. The present review demonstrates, however,
that there are similarities between the MBE growth
of para-hexaphenyl/GaAs and simple atomic sys-
tems. The island densities, island size distributions
and island shapes show analogous behavior. How-
ever, the obtained quantities cannot be interpreted
by simple fundamental processes such as hopping dif-
fusion, and the applicability of the standard models
is still questionable. Nevertheless, the quantities can
be used to predict the island morphology for certain
growth conditions. A detailed understanding of how
the atomistic or molecular growth processes are re-
lated to substrate structure and growth conditions is
vital for utilizing epitaxy to its full capability in the
formation of nanostructures.

Besides submonolayer nucleation studies, many
experiments have been done on island growth sys-
tems. Rather than describe the different systems, the
epitaxial growth of para-hexaphenyl on differently
oriented GaAs surfaces is used to exemplify such
nucleation experiments and follow the attempts to
understand the nucleation and growth behavior of
complex organic-semiconductor systems, in detail,
and to elucidate the general features in epitaxial
growth.

3.2.   *Physical properties of para-hexaphenyl*

3.2.1.   *Structural properties of para-hexaphenyl*

Para-hexaphenyl, $C_{36}H_{26}$, sometimes termed *p-*
sexiphenyl (*Lat.*), is a rigid rodlike organic molecule,
where the phenyl rings are connected to each other
via carbons 1 and 4, as shown by the structural
model in Fig. 31. The different phenyl rings are not
exactly located within one plane. However, the maxi-
mal tilt between the third and fourth phenyl rings in

crystallized para-hexaphenyl corresponds to 3.6°,[130]
a value which is small enough for considering the
molecule as a planar rigid rod.

The π electrons, which are responsible for many
properties of para-hexaphenyl, have a high mobility
along the axis of the molecule and give rise to
the highly anisotropic optical[131] and electronic pro-
perties.[132] This anisotropy is also reflected in the
crystalline structure at room temperature. Para-
hexaphenyl belongs to space group $P2_1/c$. The lat-
tice parameters are found to be $a = 2.6241$ nm,
$b = 0.5568$ nm, $c = 0.8091$ nm and $\beta = 98.17°$.[130]
The molecular axes of para-hexaphenyl are aligned
within the (010) plane, but not parallel to the a and
c axes. They are stacked along b in a zigzag arrange-
ment, forming an angle of 55° between the molecule
plane and the (010) face.[98,130]

Para-hexaphenyl is thermally very stable. It does
not dissociate below its isotropic melting point of
553°C.[133] Below the melting point, there are only
different liquid crystal phases at relatively high tem-
peratures between 450°C and 553°C verified by dif-
ferential scanning calorimetry.[134] Therefore, one can
conclude that para-hexaphenyl sublimates as an in-
tact molecule from the Knudsen type MBE source at
230°C, the source temperature used for the present
experiments. Although the para-hexaphenyl grown
on GaAs(001) with monolayer thickness at a source
temperature of 260°C and a substrate temperature
of 130°C is shown to be pure,[135] one cannot rule
out that a small fraction of molecules dissociates
at the GaAs interface, especially since the GaAs
dangling bonds are known to be effective reaction
sites. Nevertheless, para-hexaphenyl, electrochemi-
cally synthesized,[136] belongs to the organic mate-
rials, which can be sublimated under well-defined
ultrahigh vacuum conditions after adsorbed water is
removed by heating the MBE source above 100°C for
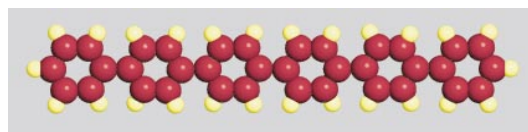24 h.[98]

Fig. 31.   Molecular structure of para-hexaphenyl. The
red and yellow balls represent carbon and hydrogen
atoms, respectively.

3.2.2. *Electronic properties of para-hexaphenyl*

Undoped para-hexaphenyl is a p type semiconductor with a low conductivity of $10^{-15}\Omega^{-1}$ cm^{-1}.[137] It shows blue electroluminescence related to its band gap of 3.1 eV.[138] The advances in manufacturing highly pure organic semiconductor thin films allow the realization of blue-light-emitting devices on the basis of para-hexaphenyl.[139–141] For these device applications, the organic thin films have to be flat and poor of defects to maintain high quantum efficiency, since both impurities and structural defects act as recombination centers. Defects can significantly limit the lifetime of the devices, because a constant electric field over the whole film is not guaranteed anymore. Therefore, the characterization of the film morphology in a quantitative manner to allow simulations becomes an important issue.

3.3. *Para-hexaphenyl island formation on GaAs(001)-(2 × 4)*

The conditions for the deposition of para-hexaphenyl used for device applications commonly lead to polycrystalline or even amorphous films. Higher substrate temperatures and lower deposition rates improve the crystallinity but increase the surface roughness by island formation. The reason for this behavior is related to the intermolecular bonding within the film, which is stronger than the bonding at the interface to the inorganic substrate.

The growth of 3D para-hexaphenyl islands on GaAs(001)-(2 × 4) is characterized by a typical AFM image in Fig. 32. The experimental setup and the film preparation procedure are described elsewhere.[98] The islands were grown at a substrate temperature of 150°C and a deposition rate of 0.05 nm/s applied during 10 min. All islands larger than a critical size of about $(0.5~\mu\text{m})^2$ exhibit an elongated shape. They are oriented into the [100] and [010] directions of the GaAs substrate with the same probability due to the substrate symmetry. Occasionally, one finds small deviations from the exact ⟨100⟩ orientations. In heteroepitaxy, the formation of three-dimensional islands with defined facets can be energetically favorable. The underlying physical reasons are known from inorganic systems. Examples are given, for instance, in the review by J. A. Venables *et al.*[41] The

driving force for island formation in heteroepitaxy results from the minimization of the free energy, which has two major contributions. First, the intermolecular bonding within substrate and film material as well as the interface bonding has to be taken into account. 3D island formation indicates strong bonding within film material and minor molecular interaction at the interface. The other contribution comes from the elastic strain energy, since flat surfaces of strained layers are unstable against undulations and shape changes.[93–95]

The basis of the 3D islands is almost rectangular, and the longer side is often more straight than the shorter one. The islands are about 0.5 μm wide and flat on top. The average height of the islands, (126 ± 4) nm, is four times larger than the average film thickness. The average film thickness is defined to be the thickness of an assumed 2D film which has the total crystallite volume and which fully covers the substrate. The orientation of the islands with respect to the GaAs(001) substrate is verified by X-ray Laue diffraction. The para-hexaphenyl islands are shown to be single-crystalline.[142]

In addition to the AFM experiments, scanning electron microscopy (SEM) and cathodoluminescence measurements have been performed in order to exclude significant surface modifications by the AFM tip. The results of the three methods are compared to each other in Fig. 33. Although electron bombardment induces distinct damages, the nature of interactions is different with respect to AFM. The
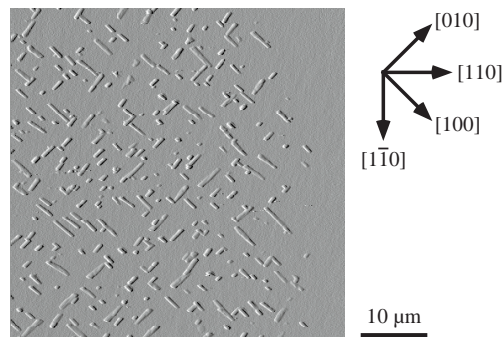

Fig. 32.   Typical AFM image near the shadow edge of the holder that indicates the Volmer–Weber growth mode of para-hexaphenyl on GaAs(001)-(2 × 4). The islands with an average height of 130 nm are grown at a substrate temperature of 150°C and a deposition rate of 0.05 nm/s. The average film thickness corresponds to 30 nm.

(a) Atomic force microscopy

(b) Scanning electron microscopy
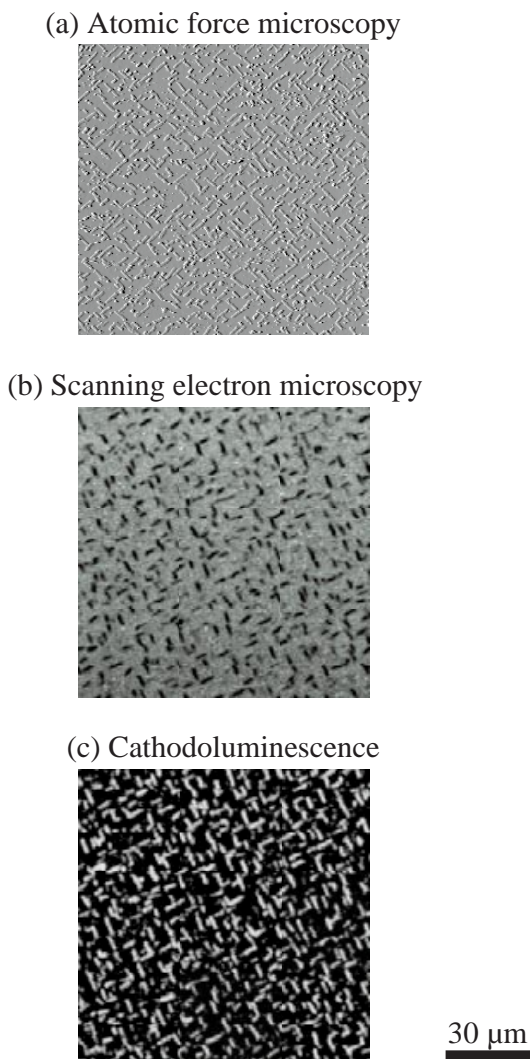

(c) Cathodoluminescence

30 μm

Fig. 33. Comparison between (a) atomic force microscopy, (b) scanning electron microscopy and (c) cathodoluminescence images showing the morphology of para-hexaphenyl on GaAs(001)-(2 × 4) grown at a substrate temperature of 140°C and a deposition rate of 0.06 nm/s (average film thickness 37 nm).

features of the images, however, are identical. Consequently, the AFM images represent an unaffected picture of the surface morphology.

Cathodoluminescence is a very sensitive tool for detecting films with a thickness of a few monolayers.[143] Cathodoluminescence of para-hexaphenyl thin films has also been detected by the use of scanning tunneling microscopy.[144] The cathodoluminescence images does not give any indication that para-hexaphenyl is present between the islands. This means that the para-hexaphenyl film between the
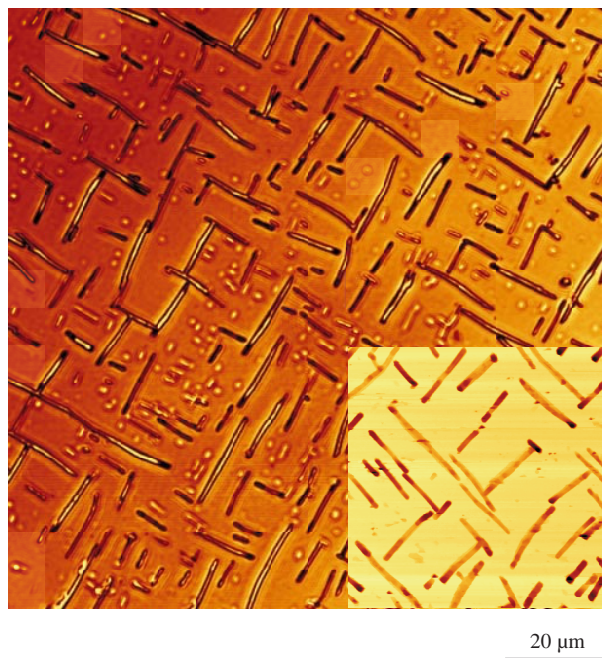

20 μm

Fig. 34. Laser scanning microscopy (LSM 5 PASCAL, Carl Zeiss) at a wavelength of 543 nm and atomic force microscopy (*inset*) images demonstrate the spatial homogeneity of large para-hexaphenyl islands grown on GaAs(001)-(2 × 4) at a substrate temperature of 150°C and a relatively low deposition rate of 0.02 nm/s (average film thickness 27 nm). Note that the larger islands are higher at their ends than at the island centers. The technical support of M. Kohler (Carl Zeiss AG, Switzerland) in taking the LSM image is gratefully acknowledged.

islands has to be extremely thin or is even not present. This observation is substantiated by the AFM images at the shadow edges of the substrate holder that do not display any step edge (cf. right part of AFM image in Fig. 32). Therefore, it is concluded that para-hexaphenyl grows on GaAs(001)-(2 × 4) in the Vollmer–Weber or 3D growth mode.

The para-hexaphenyl islands are large enough for applying conventional light microscopy to characterize their density, size and shape (cf. Fig. 34). The light microscopy image, which shows rather large islands grown at a low deposition rate, has been obtained with a LSM 5 Pascal (Carl Zeiss, Axioskop2 Mot, vario two, scan zoom 2.0, Plan-Neofluar 40 × /0.75) using a wavelength of 543 nm. Both light microscopy, a noninvasive method, and AFM images prove the surface homogeneity. The lateral information on island size and size distribution is comparable for light microscopy, electron microscopy and

AFM. Only AFM measurements, however, deliver the island heights with reasonable resolution. Note that, at the ends, the larger islands shown in the inset of Fig. 34 are higher than in the island's center. Therefore, the analysis of the surface morphology is mainly done by the use of the AFM images.

3.4. *Shape transition of para-hexaphenyl islands on GaAs surfaces*

The anisotropic island shape is not due to the anisotropy of the substrate, since for GaAs(001) the [100] and [010] directions are equivalent. The influence of the substrate reconstructions is ruled out, because the size of the domains on the substrate is not as large as 10 μm. Therefore, the elongated islands arise from the interaction of the islands with the migrating anisotropic molecules. Another indication of these interactions is the fact that the islands never cross each other. Sometimes, islands encounter each other in orthogonal fashion (cf. Fig. 34). The migration rate of individual molecules along the islands depends on the island's orientation and the molecules prefer a parallel arrangement because of the π interactions. This statement is corroborated by the observation of increased island height at both ends of the elongated islands. Since the well-oriented islands have a constant width of about 0.6 μm, one may expect a similar shape transition as discussed for monolayer copper islands on Ni(100).

3.4.1. *Shape transition of para-hexaphenyl islands on GaAs(001)-(2 × 4)*

The AFM images of para-hexaphenyl islands on GaAs(001)-(2 × 4) show that small islands up to a critical size of 0.2 μm^2 having a height of maximal 150 nm exhibit a square shape, whereas the larger islands have a rectangular shape with a constant width. This constant island width is a special feature of coherently strained epitaxial islands in heteroepitaxial growth. As already discussed in the section above, Tersoff and Tromp[96] have predicted theoretically a strain-induced spontaneous shape transition from 2D to 1D growth of flat islands with a rectangular basis. This means that 3D islands with a height much smaller than their width and length grow up to a critical size in both [100] and [010]. Above the
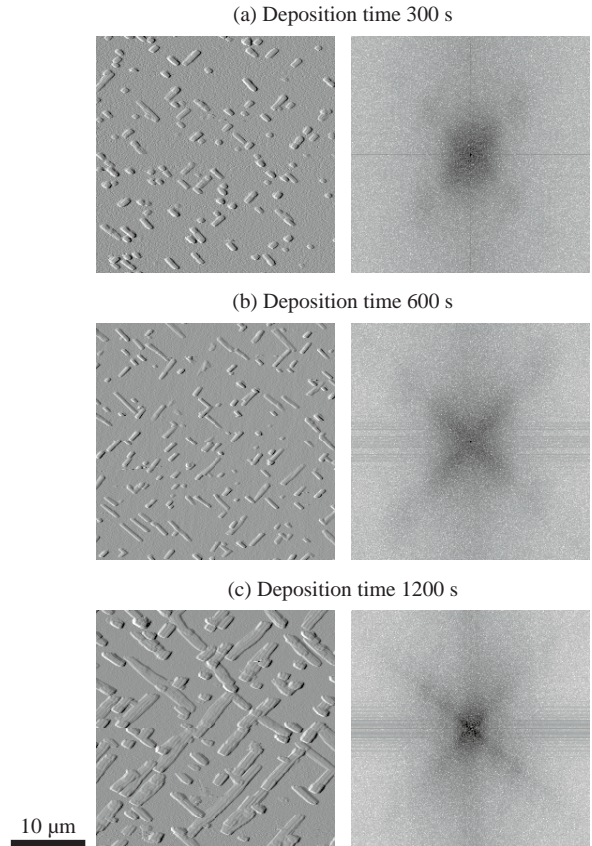
(a) Deposition time 300 s

(b) Deposition time 600 s

(c) Deposition time 1200 s

10 μm

Fig. 35.   AFM images of para-hexaphenyl islands grown on GaAs(001)-(2×4) at a substrate temperature of 150°C and a deposition rate of about 0.04 nm/s. The deposition time is indicated. Small islands have the expected square shape, whereas the larger islands exhibit an elongated shape of constant width. Note that the island width in (c) is not well reproduced by the AFM tip, indicated by the internal ripple structure of the islands. On the right hand side, the related Fourier transform of the simultaneously recorded absolute AFM images is given to emphasis the improved order in the surface morphology.

critical size, the islands grow in length but not in width. The width is even shrinking by a factor of $e \approx 2.7$ and reaches an asymptotic value. This asymptotic island width is observed with the different techniques in the images where the islands are large enough. Smaller islands may be slightly wider, as can be seen in Figs. 35(a) and 35(b). The ratio, however, is definitely smaller than a factor of e. Nevertheless, the experimental data suggest a trend towards smaller island widths near the shape transition. As the island size increases, the islands not only grow in length but also in height, an experimental detail not predicted by the theory.

The morphology of the islands as shown in Fig. 35 is characterized by an improved order with increasing coverage. The order becomes clearer by the Fourier transform of the related absolute AFM images.

3.4.2. *Shape transition of para-hexaphenyl islands on GaAs(111)*

Para-hexaphenyl grows epitaxially not only on GaAs(001) but also on GaAs(111).[145] The island shape, however, is different because of the substrate symmetry. The island morphology is given in Fig. 36. Smaller islands exhibit a droplike shape. Larger islands have not only a droplike "head" but also a "tail" of constant width and height. At higher coverages the droplike shape of the head seems

(a) $\Theta = 17$ nm
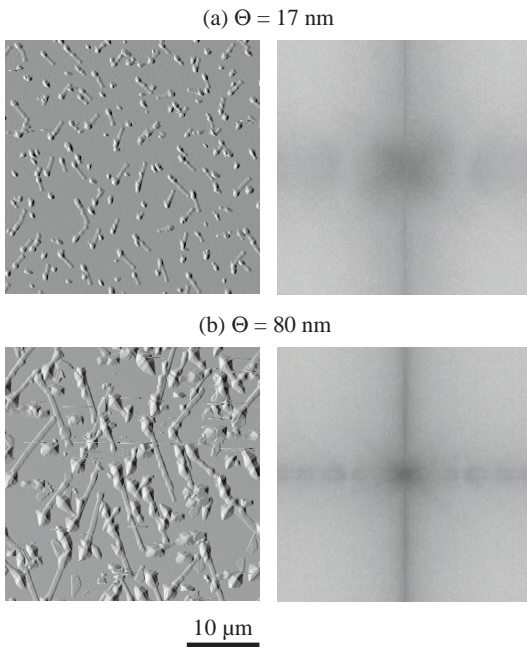

(b) $\Theta = 80$ nm

10 μm

Fig. 36. AFM images of para-hexaphenyl grown on GaAs(111) at a substrate temperature of 150°C and a deposition rate of (a) 0.03 nm/s and (b) 0.01 nm/s, respectively. The average coverages are indicated. Small islands have a droplike or pyramidal shape, whereas the larger islands consist of the droplike "head" and an elongated "tail." The typical height of the heads and of the tails is (a) 300 nm and 100 nm and (b) 800 nm and 160 nm, respectively. Because of the large island height, tip changes occur frequently; here, selected raw data are presented. On the right hand side, the related Fourier transform of the simultaneously recorded absolute AFM images is given to demonstrate that a preferential orientation of the islands with respect to the substrate is not found.

to change to a pyramidal shape with well-defined facets. The tail retains its constant width and height but both parameters increase slightly. Inspecting the AFM images, one may believe that there exist some magic angles between the tails reflecting the triangular nature of the substrate. A careful analysis including the Fourier transforms of the images, however, does not give any evidence for this behavior. It turns out that the direction of the tail is usually arbitrary with respect to the substrate. The facets of the pyramidal heads, however, are often related to the tail direction.

It is worth mentioning that the height of the heads in Fig. 36(a) is about three times larger than the height of the tails, whereas their width is almost identical. Is that the shrinking predicted by Tersoff and Tromp? The pyramidal heads in Fig. 36(b) are wider than the tails on their basis and the height is five times larger than the height of the tails. Hence, the shape transition is much more complex than the simple theory of Tersoff and Tromp can predict. Nevertheless, it is hypothesized that the shape transition is caused by the strain between the GaAs substrate and the para-hexaphenyl. Further experiments, for example by the use of low energy electron microscopy during growth, have to be performed in order to understand the formation of organic islands with such a peculiar shape.

First X-ray and transmission electron diffraction (TED) experiments[145] have already been done. They
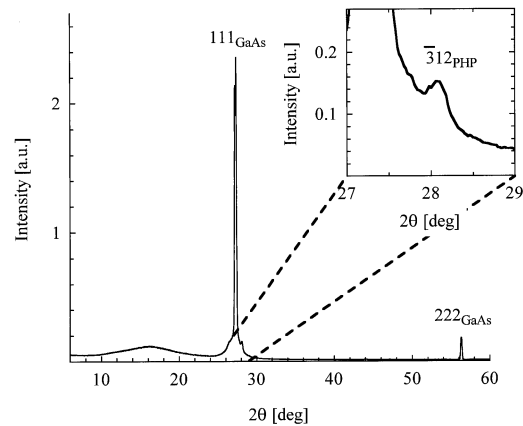

Fig. 37. θ–2θ scan of para-hexaphenyl grown on GaAs(111). The occurrence of the $\overline{3}12$ peak of para-hexaphenyl gives rise to a $(\overline{3}12)$ contact plane. The diffraction measurements are performed using Ge-monochromatized CuK$_{\alpha 1}$ radiation.
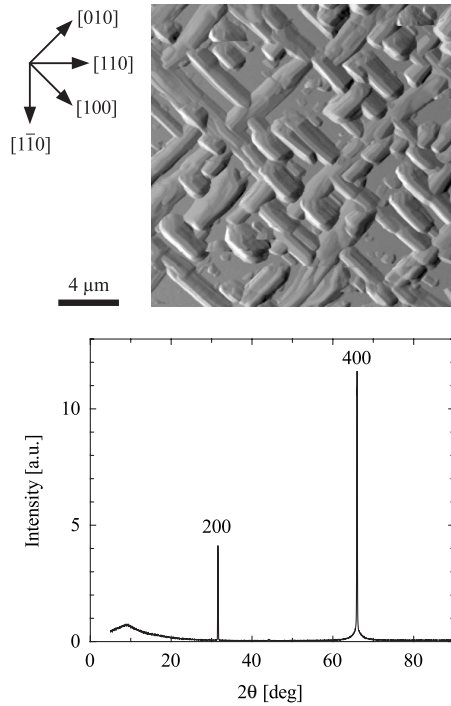
Fig. 38.   AFM image of a 0.6-μm-thick para-hexaphenyl film on GaAs(001) in differential mode. The sample was grown at a deposition rate of 0.04 nm/s and a deposition time of 4 h. The substrate temperature, initially at 110°C, was increased to 150°C after 5 min. The θ–2θ scan of this sample, which is again obtained using CuK$_{\alpha 1}$ radiation, exhibits only the 200 and 400 peaks expected for GaAs(001). This means that, the separations of crystal planes perpendicular to the surface coincide for para-hexaphenyl and GaAs.

indicate three different contact planes between para-hexaphenyl and GaAs(111). Based on the bulk structure of para-hexaphenyl at room temperature, the identified contact planes are $(\overline{3}12)$, $(11\overline{2})$ and $(\underline{1}001)$. The $(\overline{3}12)$ plane is only found by X-ray diffraction (cf. Fig. 37). Unfortunately, the high resolution θ–2θ scans cannot be used to verify the $(11\overline{2})$ and $(\underline{1}001)$ contact planes, because the theoretically expected intensity of the corresponding X-ray reflections is too small. The spatial resolution of TED is high enough to integrate just over a part of a single tail. The heads, however, are too thick to be transmitted by the electrons. Furthermore, it is not fully clear if the sample preparation procedure for the TED experiments modifies the structure of the crystallites. These preliminary results suggest that the epitaxial para-hexaphenyl islands consist of differently oriented domains, and the molecules of head

and tail may have a different orientation towards the substrate.

3.5.   Structural model for para-hexaphenyl grown on GaAs(001)-(2 × 4)

The shape and orientation of the rectangular para-hexaphenyl islands can be understood by a structural model based on the crystalline structure of para-hexaphenyl at room temperature. The model is developed combining the AFM investigations with X-ray diffraction data and geometrical considerations. Unfortunately, the X-ray diffraction data (θ–2θ scans) yield limited information. In contrast to para-hexaphenyl films deposited on glass, on Si(111)-(7×7) or on oxidized GaAs substrates, which show in X-ray diffraction 00l reflections,[135,146] distinct reflections of para-hexaphenyl grown on GaAs(001)-(2×4) are not observed, as shown in Fig. 38.

The reason for the absence of the reflections is not an insufficient layer thickness, since this experimental observation is even found for films with an average thickness of 0.6 μm. Also, the AFM images show the characteristic features of the para-hexaphenyl films irrespective of the film thickness. As an example, a representative AFM image of a 0.6-μm-thick film and the related θ–2θ scan is given in Fig. 38. The reason that we cannot observe any reflections is not an amorphous film either, because the orientation and the well-defined island shape of para-hexaphenyl prove the crystalline state of the material. The absence of the reflections is therefore attributed to the reflection conditions of the (010)-oriented para-hexaphenyl layer, which should produce $0k0$ reflections in θ–2θ scans. According to this model shown in Fig. 39, however, it is not possible to observe any reflections, which are not superimposed by substrate peaks. The reflections of the para-hexaphenyl planes parallel to the substrate surface, which fulfill Bragg's law in θ–2θ scans, match exactly the substrate peaks or have zero intensities. This is the case for $0k0$ reflections, calculated from structural data of para-hexaphenyl given by K. N. Baker *et al.*[130] The same result is deduced from the proposed model. Reflections of the type $0k0: k = 2n + 1$ are anyway systematically extinct due to the 2_1 axis; the intensities for the remaining reflections, $0k0 : k = 2n$, have relative intensities
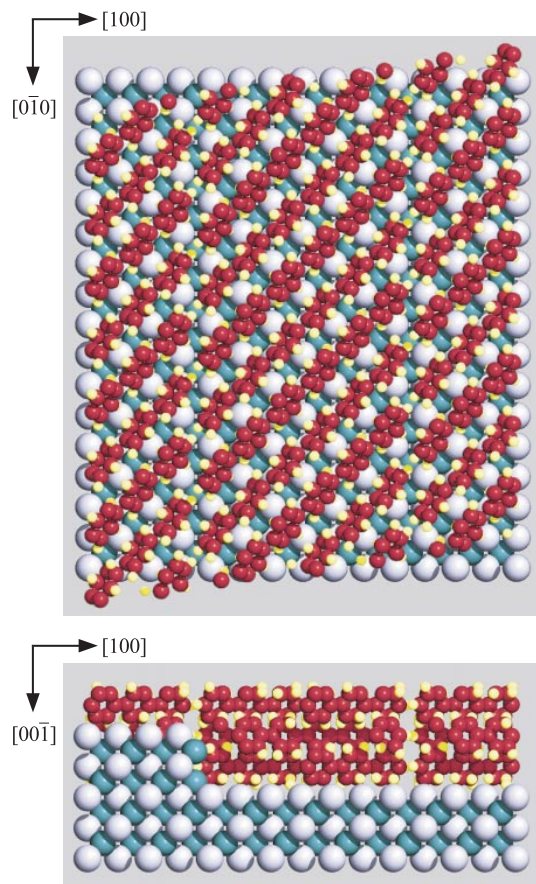
Fig. 39.   Novel structural model for para-hexaphenyl grown on GaAs(001), top and side views. The blue–green and gray–violet spheres represent the gallium and arsenic atoms, respectively. It is *a priori* difficult to determine which kind of atoms forms the interface layer. For the model, however, a determination is not necessary. The red spheres represent the carbon atoms within para-hexaphenyl of the first and second layers. Together they form a double layer with a height identical to the step height of a GaAs(001) double layer. The yellow spheres represent hydrogen. One can clearly see the excellent lattice matching in the three dimensions. The occurrence of well-defined, straight step edges along the (100) plane becomes especially evident in the side view.

lower than 1.5% and appear exactly at the positions of 00l peaks of the GaAs substrate. Hence, the b axis has to be perpendicular to the GaAs(001) surface. Anyway, the step height (double step) of GaAs, which corresponds to the cubic lattice parameter ($a = 0.5653$ nm), is only 1.5% larger than the double layer of para-hexaphenyl ($b = 0.5568$ nm). This small difference can easily be compensated for by the organic material. Steps on the GaAs(001) surface, which must occur frequently because of the 2° misorientation in $\langle 110 \rangle$,[98] should attract and absorb the para-hexaphenyl molecules. The coincidence of the 3D growth mode and the identical height for para-hexaphenyl and GaAs steps edges leads to a comfortable migration of para-hexaphenyl molecules across substrate and adlayer step edges.

The As-rich GaAs(001)-(2×4) surface is characterized by the occurrence of additional As dimers in the topmost layer. These dimers are oriented in a [110] direction. Therefore, one may assume a similar adsorption site for para-hexaphenyl. Indeed, the alignment of the para-hexaphenyl molecules in $\langle 110 \rangle$ is clearly favored because the distance between two adjacent molecules projected on (010) is 0.4 nm, a value that exactly corresponds to d_{110} of GaAs.

The only difference between the present model[98] and the refined crystal structure of para-hexaphenyl[130] is the arrangement of the long molecule axes. In order to center the six phenyl rings on six GaAs surface units, one para-hexaphenyl molecule has to be shifted by about 0.3 nm in the axis direction $\langle 110 \rangle$ with respect to the adjacent one, as shown in Fig. 39. Note that one phenyl ring fits quite nicely into one GaAs surface unit. With this arrangement, the formation of straight and long faces perpendicular to [100] and [010] is naturally explained. Moreover, the short faces are more random: they are located perpendicular to $\langle 710 \rangle$, forming an angle of about 8° to $\langle 100 \rangle$, and give rise to rougher step edges.

For this model, the monoclinic para-hexaphenyl unit cell (space group P2$_1$/c) has different dimensions: $a = 1.9986$ nm, $b = 0.5653$ nm, $c = 1.1306$ nm and $\beta = 98.13°$.[98] The packing of the molecules is almost as close as in the original cell. The difference is less than 8%. This small difference for the whole 3D unit cell should be easily compensated for by an organic material such as para-hexaphenyl.

The proposed model is somehow speculative but accounts for the AFM and X-ray diffraction observations. Its reliability is supported by the available models of other groups. In particular, a growth study of para-hexaphenyl on different substrates under high vacuum conditions[146] led to the formation of a similar para-hexaphenyl phase. This phase II has different a and c lattice parameters than the proposed model and that of K. N. Baker *et al.*,[130] and the molecules are suspected to be slightly shifted

against each other. The unit cell volume is the same as in the present model within the error bars, and hence larger than that of Ref. 130.

Unfortunately, the θ–2θ X-ray diffraction measurements cannot be used to distinguish between the original structure[130] — phase II, proposed by L. Athouel *et al.*[146] — and the present model, since only $0k0$ reflections are detected, and the b lattice parameter is identical for the three models. The occurrence of the phase II found by L. Athouel *et al.*[146] proves, however, that different packings with slightly shifted long axes of the para-hexaphenyl molecules are possible. The present model, in turn, is based on such a shift and results in the formation of straight and long $\langle 100 \rangle$ faces, as observed in the AFM images. Note the openings in the structure are clearly seen in the side view in Fig. 39.

3.6.   *Nucleation and growth of para-hexaphenyl on GaAs*

3.6.1.   *Regimes of condensation*

At elevated substrate temperatures, the sticking coefficient becomes low, and the molecules can desorb from the surface. Desorption effects result in a reduced film thickness. During the deposition experiment, the density of single molecules on the substrate surface is high and desorption starts at much lower substrate temperatures than equilibrium sublimation from a crystal. Note that, for a simple cubic lattice, there is a difference between adatom desorption and bulk sublimation at equilibrium. The latter requires an atom to be extracted from a kink site on the step edge, and three bonds have to be broken. The desorption of an adatom, however, costs the energy of only one broken bond. Hence desorption of single molecules results in a much higher rate than the other desorption processes at a given substrate temperature.

In order to quantify this desorption effect, the mean coverage is measured as a function of substrate temperature. The results are summarized in Fig. 40.

Below 140°C desorption is negligible, and the coverage reaches its maximum value. Above 140°C the coverage is reduced by desorption. At 180°C the para-hexaphenyl molecules are completely desorbed and only the bare substrate is detected. This means that the condensation is incomplete above 140°C. Therefore, it is concluded that the substrate
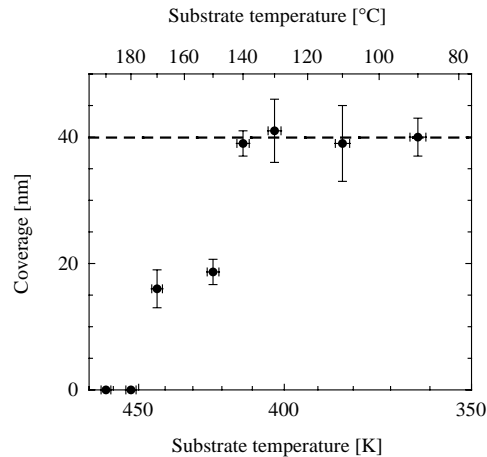

Fig. 40.   Average film thickness of para-hexaphenyl grown on GaAs(001)-(2 × 4) versus substrate temperature. The dashed line corresponds to the average coverage without desorption.

temperature range discussed (90–180°C) includes different regimes of condensation, i.e. complete, initially complete, and extreme incomplete.[41]

3.6.2.   *Analysis of the para-hexaphenyl island densities on GaAs*

Since the film thickness measurements discussed in the subsection above indicate that the range of substrate temperatures investigated covers different regimes of condensation, the size of the critical nucleus should rise with substrate temperature. Hence, the island density has to vary with substrate temperature more than exponential. Qualitatively, the variation of island density with substrate temperature is shown by AFM images in Fig. 41. In this series of experiments, both deposition rate (0.07 nm/s) and deposition time (600 s) are fixed. The images demonstrate that the density of the para-hexaphenyl islands varies over about two orders of magnitude when the substrate temperature is changed from 90 to 170°C. It should be mentioned that the nature of the individual islands at the lower substrate temperatures becomes visible in AFM images with higher magnification (not shown).

Quantitatively, the temperature dependence of island density is shown in Fig. 42 by an Arrhenius representation. Surprisingly, the island density varies with substrate temperature exactly in exponential fashion over the different regimes of condensation.

(a) T = 90 °C   (b) T = 110 °C

(c) T = 130 °C   (d) T = 140 °C

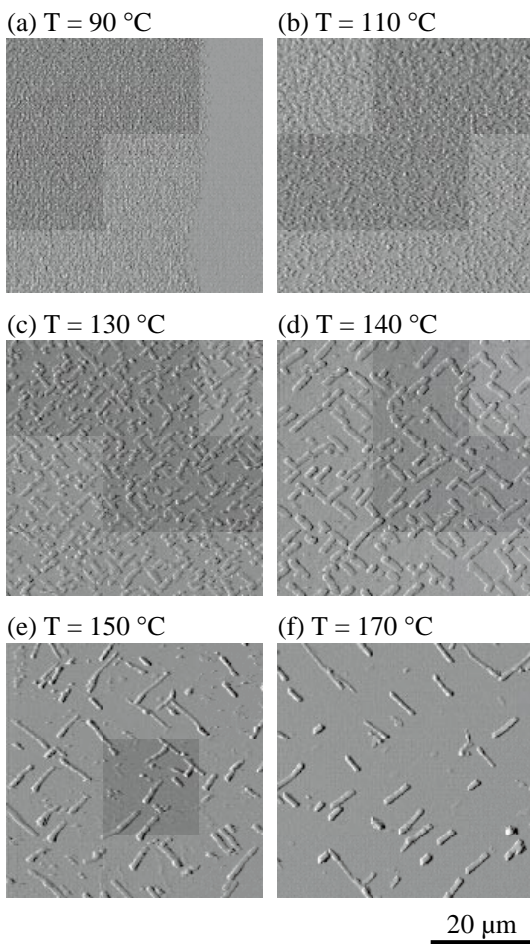(e) T = 150 °C   (f) T = 170 °C

20 μm

Fig. 41. AFM images characterizing the 3D growth of rectangular para-hexaphenyl islands on GaAs(001)-(2 × 4) at different substrate temperatures. The deposition rate (0.07 nm/s) and the deposition time (600 s) were kept constant. The substrate temperatures are indicated.

the fact that the para-hexaphenyl molecule consists of 62 atoms. Therefore, the physical interpretation of this effective activation energy is extremely complicated. Furthermore, one has to consider the highly anisotropic shape of the para-hexaphenyl molecules. It is unknown how a para-hexaphenyl molecule migrates on the substrate. It should be mentioned that the activation energy is reasonable with respect to cluster deposition experiments.[152–154] For the MBE growth of an organic material onto a semiconductor surface, there is often found a disordered interface and hence no true epitaxy.[155] Therefore, the theory of quasiepitaxial growth has been developed,[3–5]
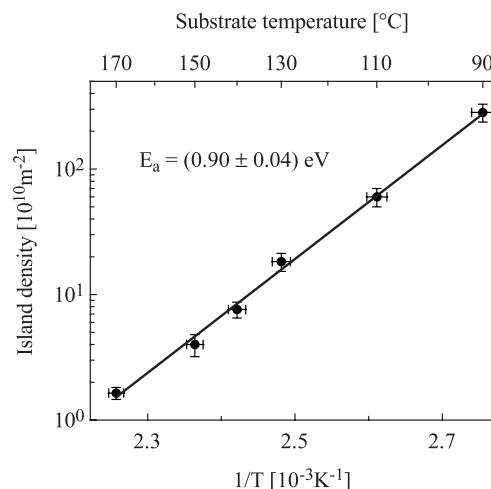
Substrate temperature [°C]

$E_a = (0.90 \pm 0.04)$ eV

Island density [10^{10}m^{-2}]

1/T [10^{-3}K^{-1}]

Fig. 42. Arrhenius plot of the measured island density of para-hexaphenyl grown on GaAs(001)-(2 × 4) at a deposition rate of 0.07 nm/s.

The decrease in island density indicates the effective mobility of para-hexaphenyl on GaAs(001). Since all data in the substrate temperature range between 90 and 170°C are on a straight line in the Arrhenius plot, the changes in island density can be described by a single activation energy. The related fit yields a surprisingly well-defined effective activation energy of (0.90 ± 0.04) eV, and a change of the size of the critical nucleus seems not to be present. Although the value is rather typical for simple semiconductor-on-semiconductor systems[147–151] and only a factor of 2 or 3 higher than that of typical metal-on-metal systems,[37,39,42] it cannot be interpreted in the same manner. One has to account for

Substrate temperature [°C]

Mean island height [nm]

$E_h = (0.253 \pm 0.025)$ eV
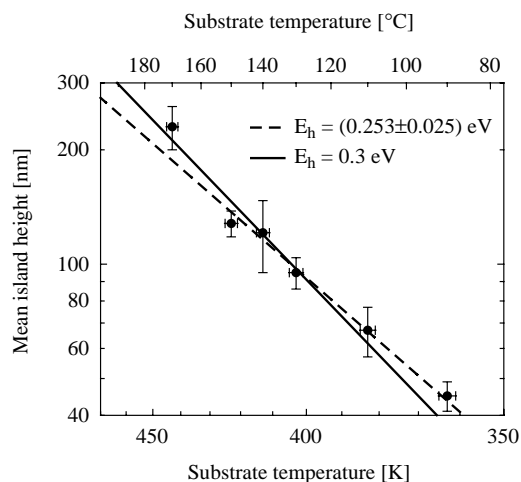$E_h = 0.3$ eV

Substrate temperature [K]

Fig. 43. Arrhenius plot of the mean island height of para-hexaphenyl grown on GaAs(001)-(2 × 4).

which, however, cannot be applied to the present system, as indicated by the high activation energy. This means that para-hexaphenyl on GaAs belongs to the first systems, where the epitaxial growth of an organic material on a semiconductor substrate is uncovered. The island density shows the well-known Arrhenius behavior, which can be used to tailor the mean island size and the island density.

Another experimental observation is the increase of the island height with substrate temperature. As shown in Fig. 43, the mean island size also exhibits the Arrhenius behavior. Here, the fit gives rise to an activation energy E_h of (0.253 ± 0.025) eV (dashed line). The full line is obtained if an isotropic growth of the 3D islands occurs. Thus, each — the height, the width and the length of the island — would have an Arrhenius behavior with a barrier of 0.3 eV, fulfilled for the height but not for the width and length.

Nucleation theory predicts a fractional power law for the rate dependence of the island density. This behavior is verified for the growth of para-hexaphenyl at a substrate temperature of 150°C, where the growth is already incomplete (see Fig. 44). One may speculate that nucleation theory can be used to extract the size of the critical nucleus i.

For extreme incomplete condensation the exponent is $2i/3$, and for initially incomplete condensation it is $2i/5$.[41] Since the exponent derived from

the slope in Fig. 44 corresponds to 2.4 ± 0.3, the size of the critical nucleus should be 4 and 6, respectively. Although the values seem to be reasonable, it is unclear whether the theory is applicable to mean film thicknesses of about 70 monolayers, since the nucleation theory is based on the very early stages of growth. Again, the rate dependence of the island density can be used to tailor nanostructures on the basis of a few well-defined experiments. In principle, the mask-shadowing vapor deposition technique is based on this rate dependence and used for the growth of para-hexaphenyl on KCl(001).[156]

3.6.3. Scaling behavior of the size distributions of para-hexaphenyl islands grown on GaAs(001)-(2 × 4)

As shown in the subsection above, not only the rate dependence of the island density can be used to extract the size of the critical nucleus but also the scaling behavior of the island sizes if the growth is irreversible, i.e. the growth takes place in the complete condensation regime. The reason for the scaling behavior of the island sizes is the constancy of the size of the critical nucleus within a temperature interval. However, studies of the scaling behavior for organic islands on inorganic semiconductor surfaces are not established in the literature. Again, this may arise from the question whether the concept of the critical nucleus is applicable for such large molecules. On the other hand, there are experiments on cluster deposition which support the applicability of the concept.[152−154] More important, however, is the question whether the scaling behavior can be found in the investigated substrate temperature range. That would support the conclusion that the Arrhenius behavior of the island density and height is based on a single activation process. Indeed, as shown in Fig. 45, the scaled island size distributions are identical — within the error bars given by the statistics, $\Delta(n_s S^2/\theta) = 0.04$ — for the substrate temperatures of 110, 130, 140, 150 and 170°C, where an analysis was convenient. The average data are shown by the open circles. For the present system, it is irrelevant whether the size of the 3D islands or just the 2D area of the islands is considered. The two exhibit identical scaling. This conclusion becomes evident when one is comparing the data of Figs. 42 and 43. Within the temperature range of 90 and
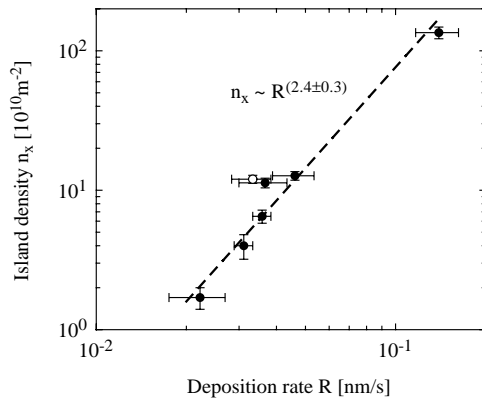
Fig. 44.   Double-logarithmic plot of the island density versus deposition rate for para-hexaphenyl grown on GaAs(001) at a substrate temperature of 150°C. The typical coverage is 25 nm, and the extremes are 10 and 90 nm. For comparison the detected island density of para-hexaphenyl islands on GaAs(111) is included (open circle).
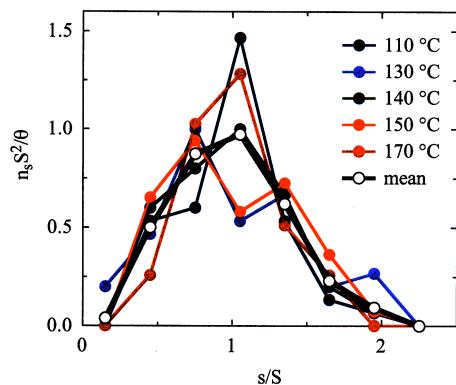
Fig. 45. Scaled island size distribution deduced from AFM images at different substrate temperatures (110, 130, 140, 150 and 170°C). The island size distribution, n_s, corresponds to the density per site of islands containing s molecules at coverage θ, and S is the average island size at fixed coverage. s/S is the scaled island size, i.e. the island size relative to the average island size, so that the size distributions collapse into one curve. Islands contain $\sim 10^6$ molecules.

170°C, the average island height is increased by a factor of 6. If the size of the 2D island grows with the same ratio, i.e. by a factor of 36, the mean island size should rise by a factor of 210, which would correspond to a reduction in island density by a factor of 210, as shown in Fig. 42.

Note that neither the Arrhenius behavior of the island density and height nor the scaled island size distribution is influenced by the desorption effects.

3.7. *Polarized blue light emission from epitaxial islands*

Large anisotropic organic molecules such as para-hexaphenyl give rise to anisotropic emission properties.[131,156–161] Therefore, it is important to control the degree of molecular orientation in the thin films to improve the electroluminescence performances and the light amplification efficiency for developing organic diode lasers. Order within thin films or islands, realized by MBE growth, can be investigated by fluorescence microscopy. Such an experiment is performed to demonstrate the epitaxial character of the para-hexaphenyl islands on GaAs(001) by an optical method. Without a polarizer one can easily observe the blue light generated within the para-hexaphenyl islands under excitation at a wavelength of 365 nm. Using an analyzer to define the polarized
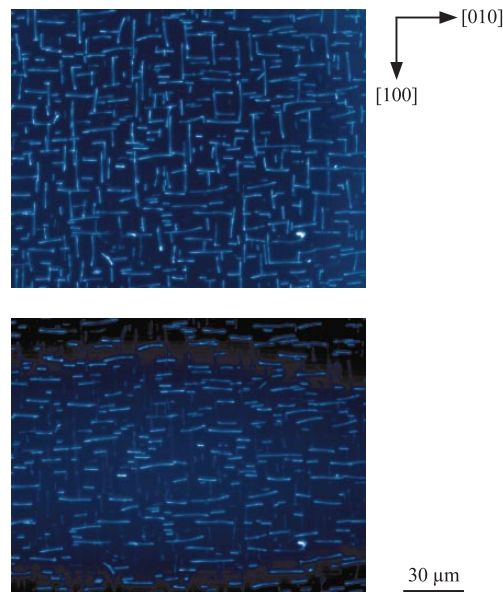

Fig. 46. Fluorescence micrograph of epitaxially grown para-hexaphenyl on GaAs(001) at a substrate temperature of 150°C and a relatively low deposition rate of 0.02 nm/s (average film thickness 27 nm). In the lower part of the figure the image is obtained with vertical polarization of the electric field, i.e. in the [100] direction. The images are obtained by the use of a Leutron Vision CCD camera (1300 × 1030 pixel, 6.7 μm each) with a Zeiss Axioplan2 microscope, a 50× (0.8 NA) Plan-Neofluar objective and a fluorescence filter set (365 nm excitation, 420 nm emission).

emission, it is found that the islands which are parallel to the polarization plane totally vanish, as demonstrated in Fig. 46. The selectivity in the polarized fluorescence images may arise from biaxially oriented molecules.[160] If one assumes that the molecule axes are always perpendicular to the elongated island, this effect is naturally explained by emission perpendicular to the long molecule axes. From the analysis above, however, it is concluded that the long axis of the islands is rotated by 45° with respect to the molecule axes, so that the proposed model cannot be used to explain the polarized light emission. This implies that the polarized emission is not understood by the emission from individual molecules but from an ensemble given by the epitaxial para-hexaphenyl island.

3.8. *Summary*

In conclusion, it has been demonstrated that para-hexaphenyl on GaAs(001)-(2 × 4) and on GaAs(111)

forms well-defined epitaxial islands. The island density shows the well-known Arrhenius behavior and the fractional power law dependency on the deposition rate predicted by the mean field nucleation theory. The size distributions of the para-hexaphenyl islands exhibit a scaling behavior similar to simple atomic systems and to cluster deposition experiments. This means that the concepts of crystal growth, i.e. nucleation and scaling theory, are quite general. Nevertheless, the nature of the deduced quantities such as the activation barrier are not clear yet and further studies are necessary for determining the fundamental processes such as migration and nucleation. Note that the growth of para-hexaphenyl on GaAs is not the exception. Similar island growth is reported for other systems: Para-hexaphenyl on KCl(001),[156,162] n-tritriacontane on KCl substrates[163] and BN on Si(001).[164]

4. Molecular Beam Deposition of Dipolar Organic Molecules at Oblique Incidence

The optical anisotropy of the islands, demonstrated in the previous section, was induced by the molecule–substrate interactions governed by the substrate symmetry. Therefore, the film anisotropy is restricted to the symmetry axes of the substrate. The experimental results of this section are based on amorphous substrates, so that preferential orientation of molecules within the film plane due to the substrate symmetry is avoided. In order to induce a film anisotropy, the symmetry is broken by the deposition experiment. The molecular beam is not directed parallel to the surface normal. The beam axis is tilted by a selected deposition angle. Since the molecules in the beam are activated and randomly distributed, interactions between the arriving molecules and the substrate are necessary for realizing anisotropic thin films by a steering effect. Such an effect has recently been demonstrated even for the homoepitaxial growth of copper.[11,165] For dipolar molecules, this phenomenon might not only result in a structural anisotropy but even in an alignment of the noncentrosymmetric species.[166–171] As a result, such organic thin films promise to open new frontiers for realizing linear and nonlinear optical devices.

4.1. *Molecular beam deposition at oblique incidence*

Film anisotropies due to oblique incidence deposition have been realized for more than 40 years, illuminated by the review of Abelmann and Lodder.[172] The main prerequisite for the anisotropy is a low surface migration of the deposited atoms or molecules, since the observed sculptured morphology develops only if migration is low. At the relatively low substrate temperatures, overhangs can become possible and the simple solid-on-solid models are not applicable anymore. In the extreme case, the particles stick to the substrate or the growing film upon first contact. Therefore, the generated films are rough and porous. The surface of the film can be self-affine fractal, i.e. it has scaling properties, which are well described.[173] These ballistic deposition models are usually not restricted to fixed deposition angles, but in the case of fixed angles one finds mound or columnar structures, which are simply explained by shadowing phenomena. However, the quantitative understanding is more complex and, therefore, some arguments given in the literature should be discussed.

Thin film formation can be divided into different stages:[174] (i) nucleation, (ii) island growth, (iii) coalescence, (iv) channel filling, and (v) steady state film growth. The transitions between the stages of this phenomenological description are somehow arbitrary. The first stage, nucleation, persists only during a fraction of deposition, but it has major influence on the film structure because the nucleation dominates features such as column size, column separation and column density. Since the column density reflects the surface migration, surface migration together with the shadowing phenomena are said to be the key elements for explaining the structure of obliquely deposited thin films. These films consist of bundles of inclined columns, with the bundles being aligned perpendicular to the vapor incidence direction. The inclination angle of the columns lies between the substrate normal and the incidence direction of the atoms or molecules. This observation has been explained by different effects and their combination: (i) adaption of the continuum model for the finite size of atoms and molecules, respectively, (ii) shadowing, (iii) conservation of parallel momentum, and (iv) angle-dependent growth. In the

simple continuum model, the edge of the film grows exactly towards the evaporation source. This naive continuum approach is too simple, because the finite size effect of the atoms or molecules is not included. Since the incorporation of the finite size effects into a general growth model valid for different species is complicated, only empirical expressions are derived. Most common is the tangent rule: $\tan\alpha = 0.5\tan\beta$,[175] where α is the vapor incidence direction and β is the columnar inclination angle, both with respect to the substrate normal. This rule does not have any physical meaning. It is merely a description which fits a number of measurements. Other empirical expressions are given by ballistic deposition models.[176]

The tangent rule, however, accounts qualitatively for the phenomena mentioned. The shadowing by neighboring atoms due to oblique incidence shifts the column orientation towards the substrate normal. Since the atoms or molecules do not arrive normally at the substrate, they have a parallel momentum. Therefore, it might be possible that they continue to move a certain distance in the direction of the beam before incorporation. However, such an effect is not confirmed yet.

The column diameter is usually much larger than the lattice constants. Hence, a continuum model can be applied to explain the inclination by angle-dependent growth. One has to assume a certain roughness and a growth rate which depends on the slope of the surface. Thus, the surface develops a roughness where the minima and maxima are shifted from layer to layer, resulting in a columnar structure. Although textures for the columnar structures are present,[177] there is no experimental evidence that certain planes are favored in the growth over others, resulting in the survival of the fastest during the generation of these anisotropic films.

Another empirical finding concerns the substrate temperature applied to generate columnar structures. The substrate temperature has to be just below half of the melting point.[174,178] A further decrease of the substrate temperature implies more disorder and smaller anisotropies in the optical or magnetic film properties.[7–10] Temperatures above the half of the melting point lead to more and more isotropic film properties due to migration and diffusion within the porous structures. As a result of the relatively low substrate temperatures applied, the films exhibit not only a porosity of up to 80% but also an enormous defect level. This high amount of structural defects limits the field of applications. For optical applications the scattering losses are often unacceptable.

Still, the method has some potential. For example, by the use of an additional evaporation source from the opposite side, the porosity and inclination angle can be chosen independently.[174,179] Furthermore, substrate rotation gives rise to chiral structures with simple helical, zigzag or four-sided square helical shapes controlled down to 10 nm.[178–187] The method has been demonstrated for fluorides, oxides[188] and some metals (Cu, Cr, Pt, Ti).[185] The use of organic materials, however, is not reported.

4.2. Prerequisites for the realization of nonlinear optically active thin films

Surfaces and interfaces give rise to second order effects such as second harmonic light, because the required asymmetry is provided by definition. Bulk materials, however, exhibit these second order effects only if the constituents have a noncentrosymmetric order. Dipolar molecules seem to be less suited for realizing a noncentrosymmetric order, because they tend to become antiparallel due to their dipole moments and the electrostatic interaction. A noncentrosymmetric order of noncentrosymmetric molecules does not correspond to the thermal equilibrium. Such structures have to be prepared far from the thermal equilibrium and have to be stabilized. Molecular beam deposition usually takes place far from equilibrium and provides further advantages. The ultrahigh vacuum conditions lead to high purity thin films. The film growth can be monitored by surface-sensitive techniques, so that the film thickness can be controlled down to the monolayer level and abrupt interfaces can be achieved. The substrate temperatures are moderate. Consequently, anisotropic thin films made of inorganic materials have been produced by molecular beam deposition at oblique incidence.[8,10] These films exhibit structural, magnetic and optical anisotropies but not an alignment of noncentrosymmetric molecules. One reason for this behavior may be the low orientational stability. The problem of thermal and mechanical stability can be mastered by hydrogen bonds

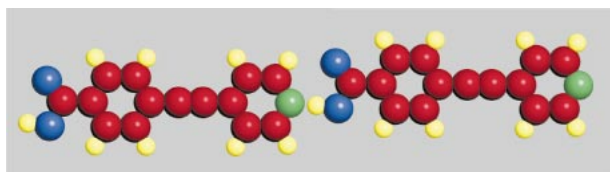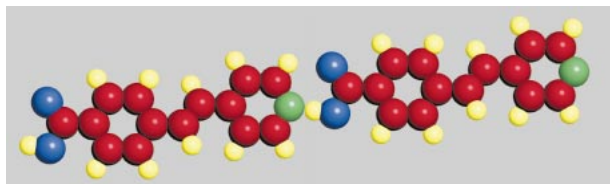(a) 4-(pyridin-4-ylethynyl)benzoic acid (**PEBA**)

(b) 4-[*trans*-(pyridin-4-ylvinyl)]benzoic acid (**PVBA**)

Fig. 47. Molecular structure of (a) PEBA and (b) PVBA, as simulated using AM1 implemented in the MOPAC Hamiltonian computer code (Cerius^2, BIOSYM/Molecular Simulations Inc.). The red spheres represent the carbon atoms, the blue ones the oxygen atoms, the green ones the nitrogen atoms and the yellow ones the hydrogen atoms. The molecules are connected by hydrogen bonds in a linear fashion.

between organic molecules.[166–169,171] These hydrogen bonds can be broken for the evaporation of appropriate molecules, i.e. the molecules have to be ultrahigh-vacuum-compatible and have to be capable of molecular beam formation. Hence, the molecules are intact at the sublimation temperatures. Arriving at the substrate, the molecules adopt the substrate temperature and can form a polymer-like superstructure by hydrogen bonding.

Two model compounds, 4-[trans-(pyridin-4-ylvinyl)]benzoic acid (PVBA) and 4-(pyridin-4-ylethynyl)benzoic acid (PEBA), are selected to demonstrate the feasibility of the scenario. The molecular structures of PVBA and PEBA are represented in Fig. 47.

Both rigid molecules comprise a pyridyl head group shown in the figure on the right hand side and a carboxylic acid tail group shown on the left hand side. The hydrogen forms a rather strong bond between the head and the tail, as indicated by solid state ^{15}N NMR spectroscopy.[166] A consequence of the strong hydrogen bonding is the relatively high melting points of PVBA (350°C) and PEBA (300°C), verified by differential
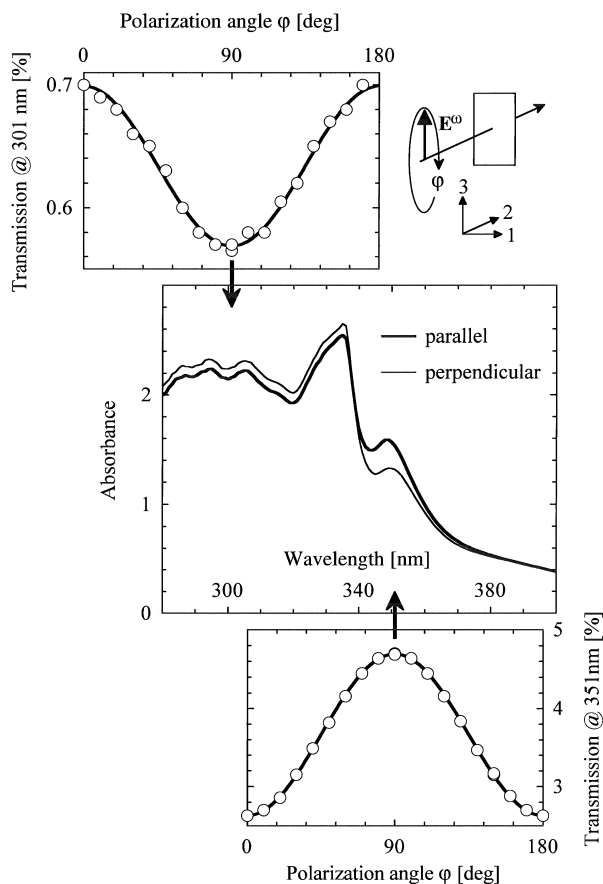

Fig. 48. Transmission measurements of ultraviolet light for PEBA on fused silica. The film with a thickness of 270 nm was grown at a substrate temperature of 100°C and a deposition rate of 0.09 nm/s. The central part shows the anisotropy of the absorbance. The transmission data as a function of the polarization angle perfectly follow a sine. At a wavelength of 338 nm, the neutral point, the phase shifts by 90°.

scanning calorimetry.[167] The hydrogen bonding guarantees not only the thermal stability but also the mechanical stability of the organic thin films. AFM measurements become possible on these thin films.[167]

The molecules are small enough that they can be sublimated below their decomposition temperature to produce a reasonably high deposition rate. A typical MBE deposition rate of 1 μm/h is achieved at a sublimation temperature of about 220°C and a base pressure of 6×10^{-9} mbar during the experiment. To avoid significant re-evaporation from the amorphous SiO_2 substrates, the substrate temperature must be kept below 120°C.[167]

4.3. *Linear dichroism of organic thin films prepared by molecular beam deposition at oblique incidence*

The anisotropy of PEBA thin films grown on fused silica (Suprasil®) with a deposition angle of $26° \pm 5°$ is shown in Fig. 48 by transmission measurements of ultraviolet light. The relatively small deposition angle guarantees film homogeneity with respect to film thickness. On the other hand, it gives rise to the observed in-plane optical anisotropy. While for wavelengths between 280 and 338 nm the absorbance is higher when the polarizer is perpendicular to the plane of incidence of the molecular beam, for wavelengths above 338 nm the absorbance becomes higher parallel to the incident beam. Note that the anisotropy below 335 nm remains almost constant. The polarization dependencies of the transmission always show the well-known sinusoidal behavior, but at the neutral point of 338 nm the phase shifts by 90°, indicating excitations parallel and perpendicular to the molecule axis. Two characteristic transmission curves below the critical point at a wavelength of 301 nm and above the critical point at a wavelength of 351 nm are given in Fig. 48. This optical anisotropy reveals the preferential alignment of the molecules within the plane of incidence. Due to the geometry of the deposition experiment that only induces the anisotropy within the plane of incidence, it is convincing that the net orientation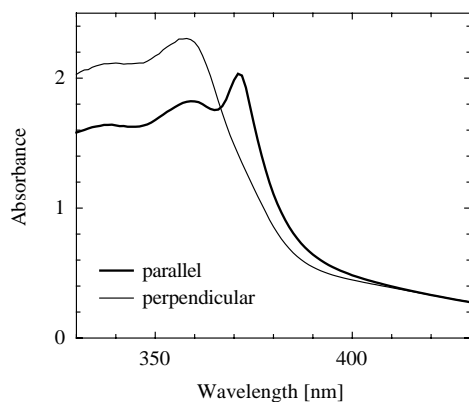 of the long axis of the molecules is parallel to the plane of incidence. This reflection of the symmetry is backed by the observation that the predominant peak at (344 ± 4) nm does not change its position substituting the fused silica substrate by glass or sapphire. However, the change of the organic material, PVBA instead of PEBA, shifts the characteristic peak to a wavelength of (373 ± 2) nm, as shown in Fig. 49. Therefore, the in-plane optical anisotropy is characteristic for the organic material. It is attributed to the long-axis-polarized transition.

The linear optical anisotropy is often identified with the linear dichroism.[189] It is defined as the difference in the absorbance parallel and perpendicular to the molecular axis. The linear dichroism is related to the molecular structure and the interactions of the molecules. Figure 50 shows the relative linear dichroism, i.e. the linear dichroism divided by its average value, as a function of wavelength. The three graphs correspond to PEBA films of different thicknesses grown on fused silica under almost identical conditions (substrate temperature 100°C, deposition rate 0.06 nm/s for the 90- and 180-nm-thick films and 0.09 nm/s for the 270-nm-thick film, respectively). The predominant peak is found at a wavelength of (344 ± 3) nm. The amplitude of the linear dichroism strongly depends on the film thickness. This observation indicates that the dichroism is not a surface or interface effect but generated within the whole film.

Preliminary experiments demonstrate a strong correlation between linear dichroism and deposition

Fig. 49. Optical anisotropy of PVBA grown on glass (microscopy slide) at a substrate temperature of 100°C and a deposition rate of 0.10 nm/s (film thickness 270 nm). The peak at a wavelength of 373 nm is characteristic for PVBA.
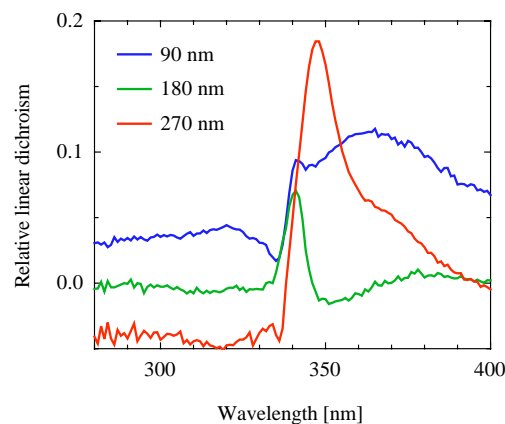

Fig. 50. The wavelength dependence of the relative linear dichroism of PEBA for three different film thicknesses. The films were grown on fused silica at a substrate temperature of 100°C and a deposition rate of 0.06 nm/s for the 90 and 180 nm films and 0.09 nm/s for the 270 nm thin film, respectively.
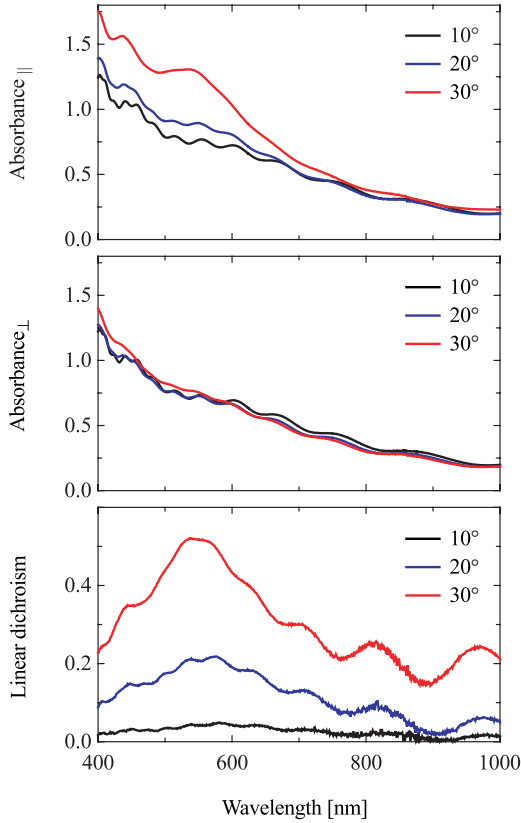
Fig. 51.   Absorbance of 1.3-μm-thick PVBA films grown on fused silica measured with the polarizer perpendicular and parallel to the plane of incidence as a function of the angle of incidence. The film anisotropy is represented by the linear dichroism.

angle. Figure 51 reveals that the absorbance measured with the polarizer perpendicular to the deposition plane (absorbance$_\perp$) is almost constant when the deposition angle changes from 10° to 30°, but the adsorbance measured with the polarizer parallel to the deposition plane (absorbance$_\parallel$) significantly increases with the deposition angle. This result is interpreted by an improved molecular order mainly parallel to the deposition plane. The maximum of the linear dichroism rises from 0.05 at a deposition angle of 10° via 0.22 at 20° to 0.53 at a deposition angle of 30°. At glancing incidence, however, the films become extremely milky due to the high surface roughness and an enormous defect level. This means that by an appropriate choice of the deposition angle the anisotropic film properties can be considerably enhanced. The in-plane optical anisotropy detected by the transmission measurements is weak in comparison with other organic thin films,[190] but comparable

to anisotropies of thin films produced by oblique incidence deposition.[10]

4.4.   *Preferential alignment of dipolar organic molecules*

The two selected molecules, PEBA and PVBA, have different end groups, implying a dipolar character of the organic molecules.[6] Semiempirical calculations for PVBA performed by C. Cai using the computer code Cerius[2] (Molecular Simulations Inc.) suggest a high dipole moment of 32.7 debyes along the long molecular axis. If the molecules are aligned, a macroscopic charge transfer should arise, which corresponds to the average of the charge transfer within the individual molecules. Linear optical methods such as absorbance measurements cannot be used to distinguish between parallel and anti-parallel molecular configurations. However, second harmonic generation (SHG), the frequency doubling of light, belongs to the nonlinear techniques and can be used to detect structural anisotropies due to a preferential orientation of the molecules. For the thin films realized by oblique incidence deposition, such a preferential orientation of the molecules can only occur within the plane of incidence, because the planes perpendicular to the molecular beam show mirror symmetry. The mirror symmetry is related to a sign reversal of the nonlinearity, and the SHG intensity $I^{2\omega}$ becomes zero. Ignoring surface and interface contributions, the second harmonic polarization, which is correlated to the second harmonic light intensity, can be defined as

$$P_i^{2\omega} = \varepsilon_0 d_{ijk} E_j^\omega E_k^\omega , \qquad (14)$$

where the Einstein summation convention has to be applied. $P_i^{2\omega}$ is the second order polarization component along axis i, ε_0 is the vacuum permittivity, and E_j^ω and E_k^ω are the electric field vector components of the fundamental wave along axes j and k, respectively. Due to the symmetry arguments summarized above, the second order susceptibility tensor d_{ijk} possesses a large component within the plane of incidence normal to direction 1 (cf. Fig. 52). By the variation of the angle of incidence Θ around axis 1, the orientation of the effective charge transfer, which is related to the molecule axis, is determined. Since the SHG intensity shows its maximum at $\Theta = 0$, it is concluded that the PEBA molecules are
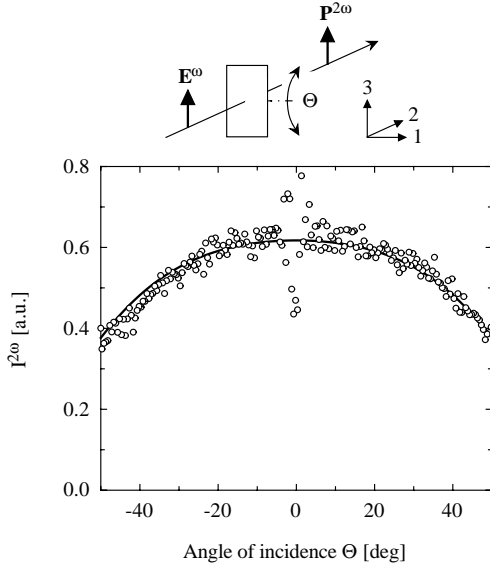
Fig. 52. SHG intensity versus angle of incidence for PEBA grown on fused silica. The film with a thickness of 180 nm was deposited at a substrate temperature of $100°$C and a deposition rate of 0.08 nm/s. The scattering of the data near $\Theta = 0$ is due to multiple reflections.

$d_{311} = d_{131} = d_{113}$, according to the Kleinman symmetry for nonabsorbing, dispersionless materials.[194] The smaller component d_{311} can be derived from the polarization angle dependence of the SHG intensity at $\Theta = 0$, which is displayed in Fig. 53. The two curves have to fulfill the following equations for the second harmonic polarization components:

$$P_3^{2\omega}(\Theta = 0, \varphi) = \varepsilon_0 d_{333} \cos^2 \varphi + \varepsilon_0 d_{311} \sin^2 \varphi,$$

$$P_1^{2\omega}(\Theta = 0, \varphi) = 2\varepsilon_0 d_{113} \cos \varphi \sin \varphi = \varepsilon_0 d_{311} \sin(2\varphi).$$
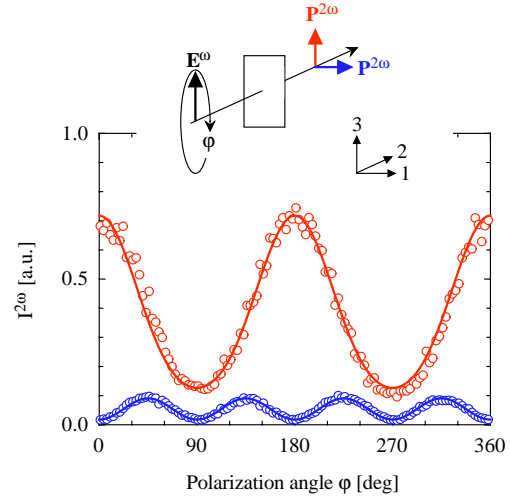
$$(15)$$

Fig. 53. SHG intensity as a function of the polarization angle. The growth conditions of the PEBA thin film on fused silica are given in Fig. 52. The solid lines are the fits using Eq. (15).

preferentially oriented in plane. The related nonlinear optical coefficient $d_{333} = (0.8 \pm 0.1)$ pm/V at a wavelength of 1064 nm is derived using the standard Maker fringe technique.[191] As calibration reference, quartz is employed ($d_{11} = 0.3$ pm/V).[192,193] The refractive indices for the fundamental and the second harmonic light (1064 and 532 nm, respectively) as used for the fit are found to be 1.75 and 1.82.[167] Note that there is no overlap of the wavelength of the second harmonic light (532 nm) and the absorption peak at a wavelength of 341 nm. Hence, resonance enhancement is negligible.

A very similar behavior is found for PVBA, which is not surprising, since the donor and acceptor end groups are identical. The SHG intensity also has its maximum at $\Theta = 0$, but the nonlinear optical coefficient $d_{333} = (0.55 \pm 0.05)$ pm/V is smaller than that of PEBA. This suggests that not only the choice of the donor–acceptor end groups but also the bridge with the two π electron ring systems is crucial for the second order effects, because the bridge determines the charge transfer as well as the linearity and rigidity of the molecule.

Since the molecules in the thin film are shown to be preferentially oriented along axis 3, besides the large component d_{333}, the only nonzero component is
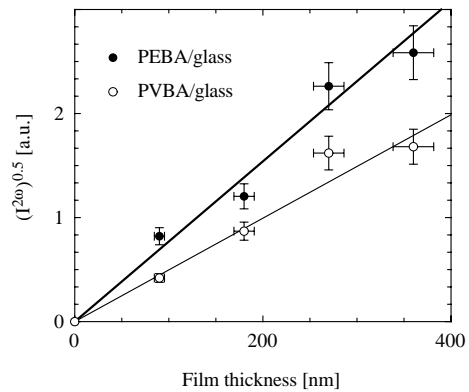

Fig. 54. Square root of the SHG intensity versus film thickness for PEBA and PVBA on glass. The films were deposited at a substrate temperature of $30°$C and a deposition rate of about 0.07 nm/s.

The SHG intensity detected is proportional to the square of the second harmonic polarization amplitude $P^{2\omega}$. Figure 53 reveals that the SHG signal follows the dependencies given by Eq. (15). The maximum of the curve for $P_3^{2\omega}$ corresponds to d_{333}, whereby the minimum is related to d_{311}. The signal detected with polarization along direction 1 oscillates with 2φ, as predicted, and the maximum of that curve gives rise to $d_{113} \sim d_{311}$. The independent fits for the two curves lead to $d_{133} = d_{311} = 0.31 \pm 0.04$.

The values of the nonlinear optical coefficients are relatively small, and contributions from the surface and the interface cannot be ruled out from the experiments discussed. Therefore, the film thickness has been varied to distinguish between surface/interface and bulk contributions. If surface and interface effects are negligible, and the degree of ordering within the film remains constant with the film thickness, the SHG intensity detected for $\Theta = 0$ and $\varphi = 0$ related to the largest nonlinear optical coefficient d_{333} should increase quadratically with film thickness.[195–197] This dependence is proven for films of the selected molecules on glass substrates in Fig. 54.

It should be mentioned that the slope could also be used to extract the nonlinear optical coefficient d_{333}. By a careful analysis of the film thickness, as is performed by different *in situ* and *ex situ* techniques,[167] the error bars are reduced, resulting in a more precise determination of d_{333}.[168]

Figure 55 shows that the substitution of the glass substrate by fused silica has almost no influence on the nonlinear optical coefficient d_{333}. This indicates that a possible grovelike microstructure of the glass substrate cannot be responsible for the molecule alignment. However, in order to exclude any possible influence of lateral substrate inhomogeneities, the following experiment is carried out. One substrate is cut into four pieces rotated to each other by 90° and fixed on the holder before deposition. The obtained anisotropy verified by transmission and SHG measurements depends only on the deposition geometry, and not on the substrate orientation.

Another experiment has been performed to exclude the possible influence of electrical or magnetic fields. Here, the sample was rotated by 180° after the film had reached half of its thickness. Due to the induced sign reversal of the nonlinearity, the SHG signal was almost zero. At the ends, where the film had only half thickness due to shadowing of the holder at oblique incidence deposition, the expected SHG signal was detected.

In conclusion, PEBA and PVBA are molecules which can be used to realize nonlinear optical thin films, whereby the molecule alignment with respect to the substrate edges can be *in situ* chosen to any desired in-plane direction simply by substrate rotation. The nonlinear optical coefficients crucially depend on the deposition conditions, namely the deposition angle, the substrate temperature and the deposition rate.

4.5. *Interpretation of the molecule alignment during molecular deposition at oblique incidence*

After the effect of oblique incidence deposition of dipolar organic molecules is clearly verified, the question of the origin of the alignment arises. Obviously, the classical theory of molecular beam deposition at oblique incidence fails, since the molecules are preferentially aligned within the substrate plane and do not develop a sculptured morphology. The formation of flat films is mainly attributed to the applied rather high substrate temperature and the moderate deposition rates. The films exhibit the highest anisotropies at substrate temperatures of about 60% of the melting point. At the moderate deposition angles of about 30°, the root mean square roughness of the film is even smaller than that of the substrate itself.[171]
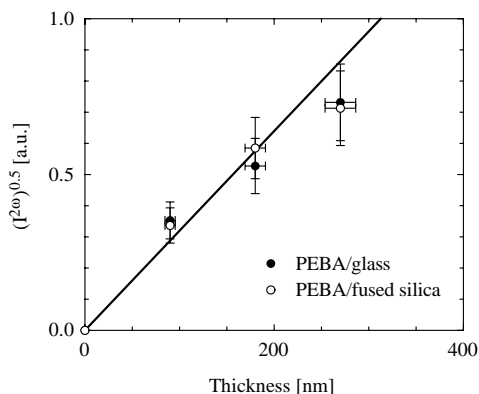

Fig. 55.   Square root of the SHG intensity versus film thickness for PEBA on fused silica and on glass. The films were deposited at a substrate temperature of 100°C and a deposition rate of about 0.07 nm/s.

Very recently a model has been developed which is based on reflections concerning the possible conformations (molecule shape and bonding) and self-shadowing as well as self-correction effects.[170] This paper includes some important phenomena and can stimulate discussions on the molecular beam deposition at oblique incidence, but the role of long range electrostatic interactions of the dipolar molecules with the substrate potential is ignored. These electrostatic interactions, however, seem to play a very important role, particularly for the selected molecules. PVBA grown on Ag(111) forms double chains at submonolayer coverages, which give rise to a regular mesoscopic pattern indicating long range repulsive interactions between the chains.[198] More important, however, are the interactions of the surface potential with the incoming molecules. Even the surface potential of a well-prepared copper surface changes the path of copper atoms deposited at oblique incidence near the surface.[11,165] The long range attractive forces between the substrate and the incoming copper atoms lead to a preferential arrival of atoms on top of islands. This phenomenon results in a significantly increased surface roughness, especially for deposition angles larger than 60°. At grazing incidence, PVBA also forms thin films with a huge roughness and the anisotropy becomes less obvious in the optical characterization.

Although many MBE systems use oblique incidence due to the system design, which includes several evaporation sources, the growth models have always regarded a homogeneous deposition rate of incoming atoms or molecules. Possible influences of inhomogeneities as a result of surface roughness on the atomic scale have been completely ignored. This shortcoming is noteworthy, since simulations based on molecular dynamics demonstrate a substantial deflection of obliquely deposited atoms towards the surface at distances as large as one nanometer above the surface.[199] Note that the surface potential has a level of a few eV, whereas the kinetic energy of the incoming atoms or molecules is just a few tenths of an eV. This means that the atoms and molecules are accelerated towards the substrate. For copper on Cu(100) it is demonstrated by trajectory calculation that copper atoms with a kinetic energy of 0.15 eV, directed with a deposition angle of 80°, actually hit the surface by an angle of 17°![11] Interestingly, this steering gives rise to a shadowing effect, since the de-

position rate is reduced behind the islands.[11] However, the same authors note that the deposition rate behind the islands never becomes zero, as expected from the classical theory.

Approaching the substrate, the dipolar molecules are not only accelerated but also tilted with its positive end group (acceptor) towards the negatively charged surface. Due to momentum conservation parallel to the surface, the molecules may become preferentially aligned within the plane of incidence, because the bonding via the two π electron ring systems of the stilbene analog is favorable. During the proceeding multilayer growth the π binding between the dipolar molecules is expected to stabilize the in-plane order, which is further stabilized in a linear fashion by the hydrogen bonding.

Unfortunately, the verification of the alignment of the dipolar molecules by a structural method is difficult, since electrons, the probe of choice, damage the film. Using atomic force microscopy the surface appears featureless and individual molecules are not resolved.[167] This means that the only possible way is X-ray measurements. The interpretation of the data, however, is somewhat speculative, because the crystalline bulk structure of the selected molecules is unknown. Polycrystalline PVBA, condensed under ultrahigh vacuum conditions, is used to perform simple θ–2θ scans in transmission mode. The diffractogram, which exhibits a sequence of peaks, is displayed in Fig. 56. The structure of PVBA, however, is too complicated to be extracted from this simple measurement. Not even the unit cell dimensions could have been detected using computer codes for indexing. Therefore, it is rather unlikely that PVBA crystallizes in a highly symmetric space group, since unit cells with a symmetry higher than orthorhombic are generally found by the code. Consequently, one may hypothesize that PVBA crystallizes with monoclinic or even triclinic structure.

Nevertheless, because of the occurrence of just one peak in the θ–2θ scans of PVBA and PEBA thin films (an example is given in Fig. 56), it can be concluded that there is a preferential orientation. The main peak for the thin film measured in reflection mode occurs at the same position as the main peak of the crystallized material ($2\theta = 24.789°$). The peaks of the crystallized PVBA, which have an intensity of about 40%, are not present for the film material, but should be detected in the case of randomly

distributed PVBA crystallites within the film. This means that the absence of further peaks is due to a preferential order of the dipolar molecules perpendicular to the surface, as expected from the optical measurements. The only peak for PVBA corresponds to a lattice plane distance of 0.35888 nm.

Another feature of the θ–2θ scan of the PVBA thin film is the half width of the peak, which is between 0.8° and 0.9°. Assuming that this half width is due only to domain size, these domains would have an extension of about 10 nm according to the Scherrer formula. Another explanation for this broadening could be a disturbed stacking sequence perpendicular to the substrate surface.[171]

In addition, a Laue transmission experiment was carried out using white radiation with a maximal energy of 40 keV. It was impossible to observe any reflection, not even with exposure times larger than 24 h and with a grazing incidence beam, respectively. However, distinct radiation damage of the glass substrate and possibly also of the PVBA thin film was found, in contrast to the reflection measurements carried out with lower energy $CuK_{\alpha 1}$ radiation.

As a consequence, it is highly desirable to uncover the crystalline bulk structure of PVBA and PEBA, for example by the use of synchrotron-radiation-based X-ray diffraction. At grazing incidence and lower energies it should be possible to detect the structural anisotropy of the thin films grown.
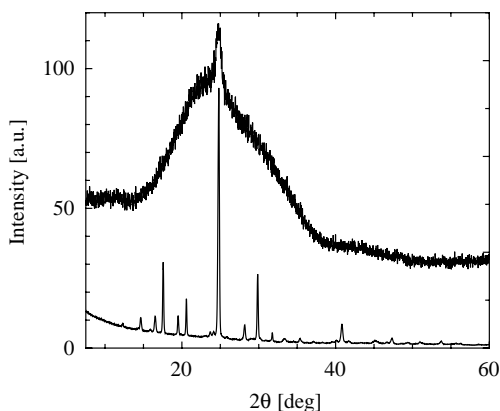

Fig. 56.   X-ray diffraction data (θ–2θ scans with $CuK_{\alpha 1}$ radiation) of crystallized PVBA from the evaporation source (transmission mode) and of a 360-nm-thick PVBA thin film grown on glass at a substrate temperature of 30°C and a deposition rate of 0.07 nm/s (reflection mode).

4.6. *Natural formation of nanostructures by molecular deposition at oblique incidence*

Poelsema and coworkers[11,165] have illustrated by high resolution electron diffraction that copper islands grown on Cu(100) exhibit a rectangular shape at oblique incidence, whereas at normal incidence the islands have the expected square shape. The islands are elongated perpendicular to the plane of incidence even for submonolayer coverages as low as 0.3 monolayers. The authors claim that for larger deposition angles, i.e. grazing incidence deposition, copper forms highly ordered arrays of parallel asymmetric ripples oriented normal to the plane of incidence. They expect a stronger effect for metals than for semiconductors or insulators, since here the substrate and deposit have relatively high electronic polarizabilities. Therefore, one can presume a substantial effect for organic molecules such as PVBA and PEBA. In order to realize such nanostructures with an optimized anisotropy, however, the deposition angles have to be larger than 30°, as used for the present experiments due to the chamber design. The selection of the deposition angle is essential to producing nanostructures with improved anisotropic optical, magnetic and electronic properties by oblique incidence deposition. Oblique incidence deposition is a method not only to structure substrates, which may subsequently act as templates for heteroepitaxial growth as mentioned,[11] but also to generate directly films with a well-defined morphology, which consists of aligned molecules.

5.   The Impact of Well-Defined Nanostructures on Biocompatibility

Biocompatibility is understood as the surface and structural compatibility of a material integrated in the desired biological environment. The performance of an implant material depends not only on its physicochemical nature but also on its surface architecture or morphology. Surface architecture is a key aspect of biocompatibility[200] and tends to have even a greater effect than chemical pattern.[201] The significance of topographic features of micrometer size has been clearly demonstrated.[15,17,20] The power of features on the nanometer scale in phenomena such

as protein adsorption and activity as well as behavior is still unclear.[26,202]

Therefore, it is highly desirable to perform protein adsorption and cell experiments on well-defined nanostructured surfaces. Germanium islands naturally grown on Si(001) provide an ideal template for such experiments. The island density, the island shape and the island size distribution can be tailored adjusting the growth conditions.

5.1. *Natural formation of 3D germanium islands on Si(001)*

The preparation of silicon with atomically flat terraces of micrometer size is well known from semiconductor research and the microelectronics industry, where generally the Si(001) surface is used.[97,147,203–205] The growth of germanium, which has a 4% larger lattice constant than silicon, on such a substrate has been described by layer-plus-island mode. The wetting layer, a uniformly strained germanium film, grows pseudomorphically to a thickness of 2–3 monolayers, followed by the formation
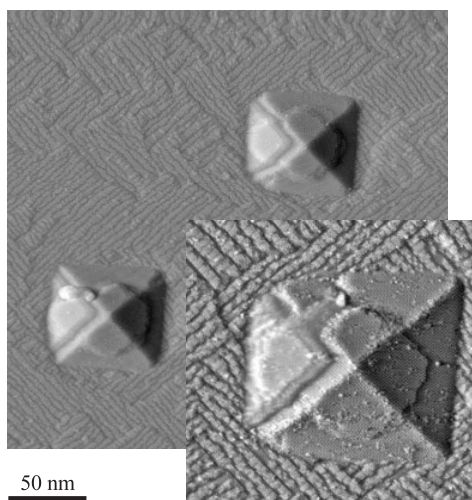

50 nm

Fig. 57. Scanning tunneling microscopy images of germanium nanopyramids (hut clusters) grown on Si(001)-(2 × 1) at a substrate temperature of 550°C and a deposition rate of 0.16 monolayers/s by molecular beam epitaxy. The germanium coverage corresponds to 5.8 monolayers. One monolayer equals 6.78×10^{14} atoms/cm^2. The pyramids have a height of about 6 nm and a basis of 60 nm × 60 nm, and exhibit well-defined {105} facets. The atomic structure is visible in the inset, where the magnification is further increased by a factor of 2. The facet on the left is not well resolved, due to the imperfect STM tip.

of three-dimensional islands on top of the uniform film.[204,206] These islands have a pyramidal or prism-like shape and are free of dislocations.[206] At lower coverages the nanopyramids are elongated or square huts with {105} facets, forming angles of 11.3° with the flat substrate.[204] Such pyramids are represented by scanning tunneling microscopy images in Fig. 57. These hut clusters are about 6 nm high and 60 nm wide. The evolution of 3D island formation is made visible using high temperature STM by Voigtländer *et al.*[207] The video can be downloaded from http://www.fz-juelich.de/video/voigtlaender/. At lower coverages the islands exhibit the square shape as shown in Fig. 57. At higher coverages the islands start to become elongated.

At even higher coverages the shape changes again, and nanopyramids, termed "dome clusters," form.[208–210] Here, the side planes are {113} and {102} facets, which give rise to angles of 25.2° and 26.6°, respectively. Their basis is comparable with that of hut clusters but their height exceeds by more than a factor of 2. These observed shape changes are attributed to transitions in the growth of strained islands.[211–213] Since the strain determines the island shape, one can take advantage of submonolayer carbon predeposition to produce smaller pyramids with a top facet.[214,215] This means that, adjusting the island volume and the strain energy at the Ge–Si interface, one finds six distinct island shapes inhering top, shallow and steep facets.[212] The size of the islands can be significantly increased by annealing, whereas the island shape can change from islands with steeper facets, termed "domes," back to huts.[216–219] In addition, the island size distribution can be tailored by self-organization during the growth of multilayer Ge/Si sandwich structures.[220–223] The multilayer arrays of coherently strained islands result in progressively more uniform island sizes and spacings irrespective of their initial density.

It should be mentioned that the formation of these islands on the wetting layer is not understood by nucleation and growth as discussed in the sections above. The growth rather proceeds via a precursor array of shallow, stepped mounds on the surface that result from the strain-driven growth instability.[224,225]

Although most of the reported studies of germanium islands growth on Si(001) are based on molecular beam epitaxy, because surface-sensitive

methods such as electron diffraction, low energy electron microscopy or STM can be applied, a limited number of publications related to chemical vapor deposition is reported.[226–228] The islands found at a coverage of about 12 monolayers have a narrow island height distribution of (15 ± 1) nm and a diameter of about 70 nm.[228] For the present study, very similar islands have been prepared also by ultrahigh vacuum chemical vapor deposition. The related *ex situ* AFM images are shown in Fig. 58. When the silicon substrate with the germanium nanopyramids is exposed to air, a limited amount of native oxide forms on the germanium. The germanium wetting layer is likely to be fully oxidized, but a thin oxide film on the pyramids does not significantly modify the pyramid geometry. This statement is corroborated by the AFM height measurements, which lead to an almost constant value of (15 ± 3) nm, in agreement with the *in situ* STM measurements. Certainly, possible subtle effects associated with the strain of the native oxide may deform the pyramids or change their facet structure. The strain may expand the island surface, inducing depressions around the islands.[228]

The AFM images directly provide the surface morphology. However, the quantification of the surface roughness using the AFM images with different island densities is generally obscure. As shown in Table 1, the data for the root mean square (RMS) roughness and average roughness as well as the extracted effective surface depend significantly on the scanning range and the surface morphology itself. Consequently, these data cannot be used for the quantitative analysis of properties on the nanoscale surface roughness.

As an alternative, one can count the islands on a certain area for different images to determine the island density. Since the height of the nanopyramids can be precisely measured by the AFM and the shape
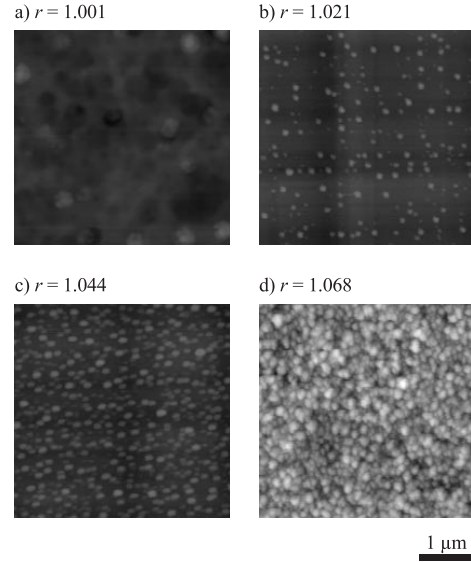

Fig. 58. AFM images illustrating the pyramid density. The roughness factor r corresponds to the ratio between the effective and the projected surface. The gray scale is chosen to 80 nm.

Table 1. Characterization of surface roughness. AFM scanning range is given in brackets.

Substrate	RMS roughness (nm)	Average roughness (nm)	Effective surface	Pyramid density (10^{12} m^{-2})	Roughness factor r
a	3.7 (5 μm)	2.7 (5 μm)	1.001 (5 μm)	0.84	1.001
	5.1 (10 μm)	3.2 (10 μm)	1.001 (10 μm)		
b	4.7 (2.5 μm)	3.1 (2.5 μm)	1.010 (2.5 μm)	12.56	1.021
	5.1 (5 μm)	3.6 (5 μm)	1.006 (5 μm)		
	7.5 (10 μm)	6.0 (10 μm)	1.004 (10 μm)		
c	5.7 (2.5 μm)	4.5 (2.5 μm)	1.018 (2.5 μm)	26.08	1.044
	5.8 (5 μm)	4.6 (5 μm)	1.012 (5 μm)		
	6.1 (10 μm)	4.6 (10 μm)	1.008 (10 μm)		
d	11.4 (2.5 μm)	9.0 (2.5 μm)	1.070 (2.5 μm)	40.16	1.068
	12.0 (5 μm)	9.0 (5 μm)	1.048 (5 μm)		
	13.0 (10 μm)	10.0 (10 μm)	1.027 (10 μm)		

of the dome pyramids is known, the effective surface comes to light. The roughness factor is defined by the ratio of the effective surface to the projected surface. For pyramids, the fraction of the surface which is covered by the islands has to be weighted by the inverse cosine of the facet angle. Hence, even a possible shape change of the nanopyramids due to the natural oxidation can be considered simply by an additional factor.

5.2. *Effects of surface roughness on wetting hysteresis*

It has been reported that surface roughness modifies the contact angles and the hysteresis of wetting. In general, the authors claim that the contact angles are greater on rough surfaces than on smooth surfaces and that the wetting hysteresis increases with the surface roughness.[229] However, sometimes the same authors state that surface roughness has no definite effect on the contact angle.[230] For contact angles smaller than 90°, the contact angle can even decrease with surface roughness explained by the capillary effect.[231] The reason for the inconsistency can often be found in the qualitative characterization of surface roughness, for example "highly polished," or in the obscure RMS roughness determination by the scanning probe techniques as discussed in the subsection above. Furthermore, very recently wetting and dewetting studies on surfaces, structured on the micrometer scale, have uncovered shape changes of the droplet associated with morphological transitions.[232–234] Hence, the well-accepted Young equation is not satisfied for small enough domains.

Therefore, the question arises as to how far nanoscale surface morphology controls the contact angle and its hysteresis. The answer is important for very different fields, including pharmaceutical,[235] tribological and conduction problems.[236] Potentially, it also plays a significant role in biocompatibility.[237–239]

Since Young has established the relation between the interfacial energies and the contact angle, wetting is understood as a thermodynamic phenomenon.[240] Therefore, Wenzel introduced the roughness factor, the ratio of effective and projected surface, to account for the surface roughness.[241] He justified the roughness factor by the statement that within a measured unit area of a rough surface the intensity of the surface energy is greater than in the same measured

unit area on a smooth surface. Although various experimental studies have depicted this effect qualitatively, there is no evidence presented because the Wenzel ratio was not detected exactly.[231] Since the Wenzel ratio can be exactly determined for the pyramidal surfaces, it is worth measuring the contact angle versus the roughness factor. Naturally oxidized silicon and germanium substrates are known to be very hydrophilic. Typical values for water are around 40°.[242–245] This angle is already rather small, and contact angle measurements below 15° exhibit a large error bar. Water, the liquid with the highest possible liquid–vapor interfacial energy related to the highest possible contact angle,[246] is also used in the present study. The problem here is the fact that the result strongly depends on the ambient conditions, namely the humidity. Therefore, the direct measurement of the equilibrium Young angle as a function of nanoscale roughness was crude. An experiment which is much more reproducible is the dynamic measurement of the advancing and the receding contact angle. Again, the results depend crucially on the ambient conditions. Therefore, it is decided to measure the dynamic contact angles on the differently rough substrates after water treatment. Thus, the surface is covered by a very thin water film, which does not equalize the roughness, but which makes the measurement reproducible.
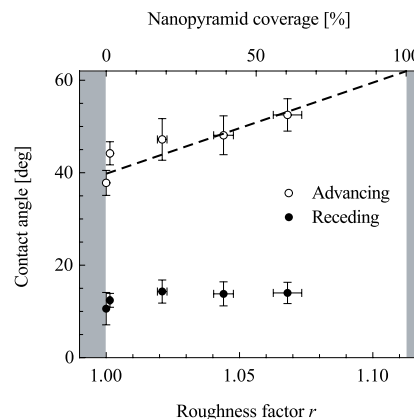

Fig. 59. Contact angles of water versus roughness factor to elucidate the increase of the contact angle hysteresis with the nanometer scale surface roughness. The measurements were performed at room temperature. The dashed line represents the linear regression of advancing angles. The gray areas are not accessible with a nanopyramidal surface having 26° facets.
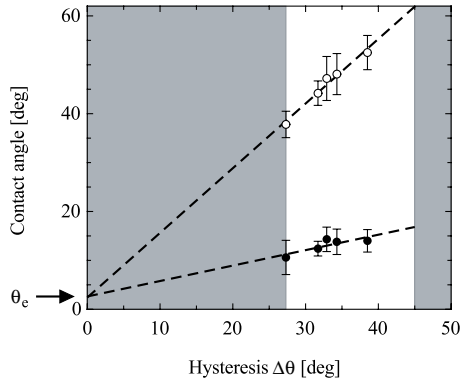
Fig. 60. Advancing (open cycles) and receding (filled cycles) contact angles versus contact angle hysteresis for water on surfaces with different Ge nanopyramid density. The dashed lines correspond to the linear regressions. The gray regions are not accessible by the measurement. The Young angle θ_e derived is close to zero. Note that the presentation does not contain directly the surface roughness.

The results, represented in Fig. 59, elucidate that the advancing contact angle of water can change by $20°$ from flat substrates to substrates with maximum pyramid density, whereas the receding contact angle remains constant within the error bars. Note that the contact angle measurement is rather difficult for values below $15°$. To reduce the error bars, six independent measurements, each on the bare silicon wafer (not shown), on the flat germanium wetting layer and on the four nanostructured substrates as reproduced in Fig. 58, were carried out. Each measurement consists of 20 angles at advancing and receding water droplets.

The equilibrium contact angle θ_e is found by the intersection of the fits for advancing and receding angles versus contact angle hysteresis $\Delta\theta$ with the ordinate at $\Delta\theta = 0$,[231] as shown in Fig. 60. The contact angle hysteresis is the difference between the advancing angle θ_a and the receding angle θ_r : $\Delta\theta = \theta_a - \theta_r$. As a result, one finds a system of two linear equations:

$$\theta_a = A_a\Delta\theta + \theta_e\,,$$
$$\theta_r = A_r\Delta\theta + \theta_e\,, \qquad (16)$$

with $A_a = A_r + 1$. The Young angle, fitted by linear regression $\theta_e = 2.5° \pm 4.0°$, is close to zero. It is attributed to the water pretreatment. Of course, at equilibrium water on water forms the thin films with contact angle zero. Again, the gray regions of Fig. 60,

which are inaccessible for the measurement, illustrate the relatively small window of contact angle hysteresis available by dome cluster nanostructuring. The dynamic measurements give access not only to the equilibrium contact angle but also to a second parameter, which is the slope (A_a and A_r, respectively). The slope is attributed to the resistance of the water layer adsorbed to the nanostructured substrate to the wetting by water. Hence, dynamic contact angle measurements provide a means of characterizing the surface morphology and roughness.

The understanding of contact angle hysteresis, however, has a preliminary character. Although wetting hysteresis has been theoretically treated on idealized surfaces with nanoscale roughness[247] and even at the molecular scale,[248] the phenomenon is not fully clear. First, the influence of drop size[249] and spreading velocity has to be clarified by experiments. Second, besides the barrier effect, which gives rise to a symmetric hysteresis, where the equilibrium contact angle is simply the arithmetic mean of the advancing and the receding angle,[231] and besides the capillary effect, which leads to a contact angle reduction,[231,240,250] another phenomenon must exist to describe the plot of Fig. 60.

5.3. Adsorption and activity of selected proteins on nanopyramidal surfaces

Protein adsorption is a primary event when an implant surface is exposed to living tissue. The inflammatory response is closely correlated with the initial protein adsorption. In order to optimize an implant surface by a well-defined nanostructure, the influence of the surface morphology on the adsorption behavior has to be demonstrated.

Proteins such as bovine serum albumin (BSA) and bovine γ-globulin (BGG) have sizes comparable to the side planes of the nanopyramids. The geometry of the hut and dome cluster is compared with the extensions of BSA and BGG[251] in Table 2.

The pyramid edges provide different adsorption sites for BSA and BGG. Consequently, one may assume that the presence of nanopyramids modifies the protein adsorption and activity. Indeed, the amount of adsorbed proteins, BSA and BGG labeled with fluorescein isothiocyanate, tremendously increases with the nanopyramid density on the substrate. The

Table 2. Extensions of nanopyramids and selected proteins.

Structural element	Area of base (nm^2)	Height (nm)	Facet	Facet angles
Hut cluster	60×60	6	{105}	10.9°
Dome cluster	60×60	15	{113}, {102}	25.2°, 26.6°
BSA	3.8×3.8	14		
BGG	4.4×4.4	23.5		

data are shown in Fig. 61. The higher protein adsorption of BGG with respect to BSA is only a result of the higher molecular weight. The surface concentrations are comparable. Experimental details on the protein concentration measurements are given elsewhere.[252] On the flat germanium substrate without pyramids, about 20 ng/cm^2 adsorb. Increasing the effective surface by 7%, the amount of adsorbed proteins rises by a factor of 2.5. This means that the adsorption sites are different on the flat and the pyramidal surface. Nanopyramids are effective adsorption sites for BSA and BGG.

The stronger protein–substrate bonding at the nanopyramids can modify the conformation and thereby the protein activity.[253,254] Here, protein activity is understood as the capability of recognition and, therefore, the affinity interactions between BGG and anti-BGG-POD (POD — peroxidase). The experimental determination of the protein activity is given in Ref. 252. It was found that the amount of

biologically active BGG does not scale with the adsorbed BGG. It is even lowered on the substrate with a high nanopyramid density. On the flat substrates without pyramids, BGG is almost completely active, as demonstrated by the data of Fig. 62. The relative activity of BGG decreases with pyramid density. When the substrate is fully covered by pyramids, BGG becomes totally inactive, as shown by the open circle in Fig. 62. This happens already well below the maximal nanopyramid density, since BGG adsorption is expected to be dominated by the nanopyramid ledges. Consequently, the nanopyramids are effective adsorption sites changing the conformation of the protein.

The protein adsorption is true to scale as shown in Fig. 63. Here, three potential adsorption sites of high symmetry are represented. The selected proteins consist of three parts of elliptical shape connected by the hinge region. Fc means fragment crystallizable and Fab denotes fragment antigen binding. The angle between the two Fab parts varies between 0° and 90°.[255] The change in the conformation of the adsorbed BGG can arise from protein
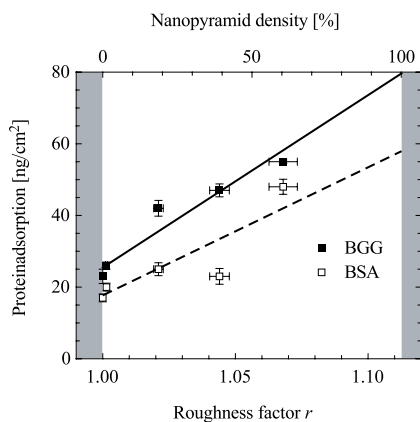
Fig. 61. Protein adsorption of BSA and BGG as a function of the roughness factor. Although the effective surface increases only by 7%, the amount of adsorbed proteins is more than a factor of 2 higher on the rough than on the flat substrate, indicating the existence of preferred nucleation sites at nanopyramids.
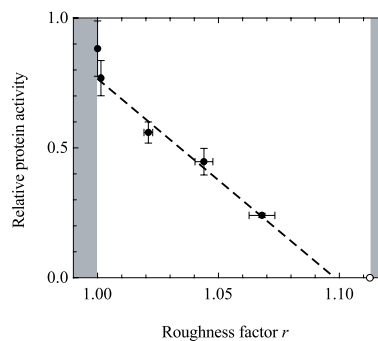
Fig. 62. Ratio between anti-BGG–POD and BGG as a function of the roughness factor. The ratio decreases with pyramidal density, as illustrated by a linear fit, reaching zero just below the maximal possible pyramid density (open cycle).
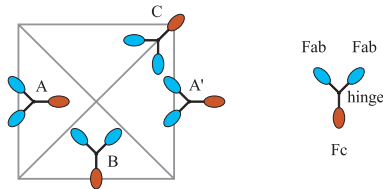
Fig. 63.   A selection of possible adsorption sites of BGG at nanopyramids.

bending at the pyramid ledges or from the increased contact area of the elliptically shaped protein at the ledges. Another possible mechanism is the self-blocking of the proteins close to the monolayer coverage.

The adsorption sites labeled A and A′ have identical adsorption energy, if the side plane of the pyramid and the flat surface are chemically equivalent. These two sites are preferred, since both of the Fab parts form an increased contact area with the substrate at the pyramid ledges. However, if the interaction between the substrate and the Fc part is much stronger, the configuration B becomes possible. The adsorption of BGG at site C is related to a possible protein bending. In order to understand the adsorption and the activity of BGG, it is highly desirable to perform measurements to identify the preferred adsorption site.[256] The identification of the adsorption side is a prerequisite for understanding the improved protein adsorption and the reduced activity of BGG, and, finally, for taking advantage of this phenomenon for implant design.

5.4. *Reduction of inflammatory reactions by nanopyramids*

Inflammatory reactions can be studied applying the monocyte-like cell line U937. Monocytes and especially the cells of U937 contain a special receptor (FcγIIR),[257] which allows interactions with the intact Fc part of BGG as present in bovine serum. These interactions result in an activation characterized by the expression of the cytokines interleukin-1β (IL-1β) and the tumor necrosis factor (TNF-α).[258,259]

The observations of the increased adsorption of BSA and BGG as well as of the reduced activity of BGG due to the nanopyramids are supported by the cell viability and the cytokine release of the monocyte-like cells from the cell line U937. The

in vitro assays with monocytes show that the viability of the monocytes after five days is zero on the substrate with only a very few nanopyramids and increases with the surface roughness until at maximal pyramid density the viability reaches the reference value as given by the open circle in Fig. 64. It should be noted that the total number of cells is almost constant on the different substrates.

The number of viable cells is a result of cell activation. During activation, cytokines, i.e. IL-1β and TNF-α, are expressed. On one hand, the cytokine release leads to an amplified activation, and, on the other hand, TNF-α is cytotoxic for the monocyte-like cell line U937.[260] Consequently, low viability means high activation. The expression of TNF-α is highest
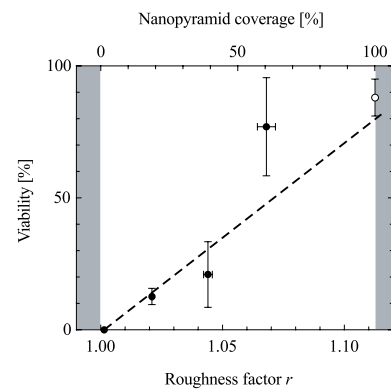
Fig. 64.   Viability of monocyte-like cell line U937 versus roughness factor. The strong correlation between viability and pyramid density is obvious. The reference is reached at the maximal possible pyramid density (open cycle). The dashed line corresponds to the linear fit under consideration of the error bars.
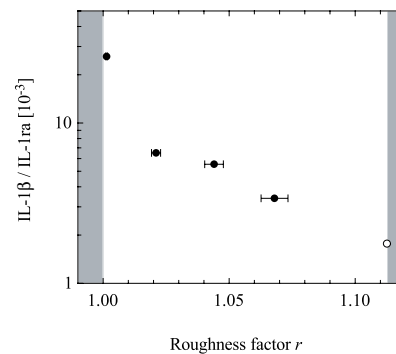
Fig. 65.   The ratio between the released proteins IL-1β and IL-1ra crucially depends on the pyramid density. The reference is reached at the maximal possible pyramid density (open cycle).

r = 1.001

30 µm   3 µm

r = 1.068

30 µm   3 µm
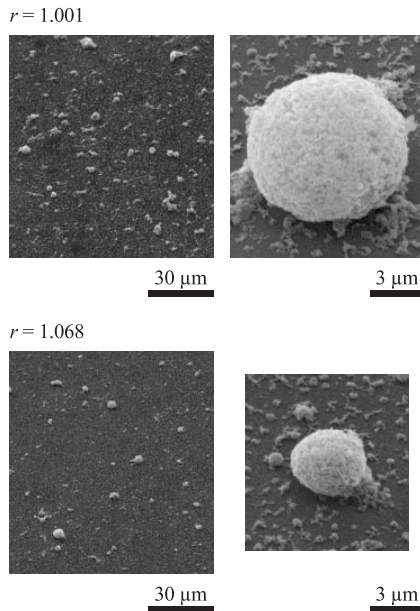
Fig. 66. SEM images of cell fragments and large cells formed on the substrates with the smallest and the largest nanopyramid density [cf. Figs. 58(a) and 58(d)]. The substrate with few pyramids shows large amounts of cells and cell debris. Furthermore, the cells are a factor of 2 larger in diameter than on the surface with high pyramid density, in agreement with cytokine release. Note that a typical cell size corresponds to the sizes of the AFM images in Fig. 58.

for the monocytes on the substrate with only a few nanopyramids and lowest for the substrate with the highest pyramid density. The related AFM images are shown in Figs. 58(a) and 58(d). In addition, the amount of IL-1β, one of the most crucial cytokines in inflammatory reactions, decreases with pyramid density. Even more important for the inflammatory behavior is the ratio of the cytokines IL-1β and its receptor antagonist IL-1ra.[261] This ratio exhibits a more than exponential decay with the roughness factor, as verified by Fig. 65. This behavior can be qualitatively supported by electron microscopy images of the cells and their fragments. Figure 66 represents two images of the substrate with the lowest pyramid density and two images of that with the highest density on different scale showing an increased amount of cell fragments and more expanded cells.

5.5. *Conclusions*

Epitaxial growth of germanium on Si(001) can be used in a natural way to realize nanopyramids of identical shape with different density and without the use of any lithographic technique. Counting the nanopyramids, the effective surface and the roughness factor (Wenzel ratio) are determined with high precision. Since the study is focused on dome clusters with facets, which form an angle of about 26° with the substrate, the roughness factor can be varied between 1.0000 and 1.1126. The nanopyramids give rise to a strong interaction between BSA and BGG on one hand and the substrate on the other hand, changing the protein conformation. BGG adsorbed on the nanopyramids becomes inactive. Related experiments with monocyte-like cells reveal a strong correlation between nanopyramid density and cell viability as well as protein release responsible for inflammatory behavior. Along these lines, features on the nanometer scale such as nanopyramids can reduce the inflammatory reactions of various implants by the application of structural compatibility.

6. Conclusion

Copper on Ni(100), a heteroepitaxial system with square symmetry, is comprehensively studied using variable temperature scanning tunneling microscopy. The study demonstrates that the mean field nucleation theory and the scaling theory also explain the very early stages of heteroepitaxy. The nucleation kinetics dominates the island density. Cu/Ni(100) is the first heteroepitaxial system where an abrupt transition in the stable island size from the dimer to the tetramer is consistently uncovered by mean field nucleation theory and scaling theory. Other quantities, the barrier height of monomer migration, the dimer bond energy and the attempt frequency, are determined with unattainable precision. By the use of these quantities and the nucleation theory, the island density and size can be tailored adjusting substrate temperature, deposition rate and coverage. In addition, the present review demonstrates that postdeposition effects associated with a high monomer density on the substrate can be described, quantitatively. Strain effects due to the lattice mismatch between substrate and film material, however, play a crucial role in heteroepitaxy already at submonolayer coverages. Contrary to nucleation, which is dominated by the growth kinetics, the strain effects are of thermodynamic origin and cannot be outwitted by the choice of the growth conditions. For

copper on Ni(100), the strain is relieved by successive processes: island ramification, stripe and dislocation formation. These strain-relieving mechanisms are uncovered and quantified especially by variable temperature scanning tunneling microscopy.

The general features of epitaxial growth, predicted by the mean field nucleation theory, are verified for the heteroepitaxy of 3D para-hexaphenyl islands on GaAs(001)-(2 × 4). The island density exhibits the well-known Arrhenius behavior on the substrate temperature and the fractional power law dependency on the deposition rate. Consequently, island density, island size, and island size distribution can be tailored in the same manner as for simple atomic systems. The transitions in island shape of para-hexaphenyl on GaAs, which depend on the substrate symmetry, are explained by the spontaneous shape transition theoretically predicted by Tersoff and Tromp.[96] This means that the concepts of crystal growth with their thermodynamic restrictions have a universal character.

The deposition of anisotropic molecules onto substrates of high symmetry can lead to nanostructures with anisotropic properties. The para-hexaphenyl islands grown on GaAs(001)-(2 × 4), for example, show polarized blue light emission. Another method to realize nanostructures with anisotropic morphology is the deposition at oblique incidence. Oblique incidence deposition of dipolar molecules onto amorphous substrates even results in a preferential alignment of the molecules. This preferential alignment of the "heads" of the molecules is demonstrated for the first time by the presented nonlinear optical measurements.

Anisotropic properties are common in living matter systems. The impact of nanostructured substrates and scaffolds on tissue formation, however, is still unknown. The present work gives clear evidence that well-defined nanostructures prepared by molecular beam epitaxy, i.e. germanium nanopyramids on Si(001), can considerably improve the biocompatible properties of implants. The interdisciplinary character of the nanosciences on living matter is elucidated by the observation that the nanopyramid density alters not only the inflammatory behavior, the adsorption and the activity of selected proteins but also the contact angle hysteresis, a purely physical phenomenon not yet fully understood.

By the use of physical vapor deposition, stable nanostructures can be tailored with respect to density, size, shape, spacing, orientation and anisotropy. Undoubtedly, this nanofabrication approach opens up new opportunities to engineer novel optical materials and to understand fundamental interactions of scaffolds and implants with proteins, living cells, and, finally, different kinds of tissue to provide an essential contribution to structural biocompatibility.

Acknowledgments

References

1. E. H. C. Parker (Plenum, New York, London, 1985).
2. M. A. Herman and H. Sitter, *Molecular Beam Epitaxy: Fundamentals and Current Status* (Springer, Berlin, 1996).
3. Y. Hirose, S. R. Forrest and A. Kahn, *Appl. Phys. Lett.* **66**, 944 (1995).
4. Y. Hirose, S. R. Forrest and A. Kahn, *Phys. Rev.* **B52**, 14040 (1995).
5. S. R. Forrest, *Chem. Rev.* **97**, 1793 (1997).
6. C. Bosshard, K. Sutter and P. Prêtre *et al.*, *Organic Nonlinear Optical Materials* (Gordon and Breach, Basel, 1995).
7. Y. Park, E. E. Fullerton and S. D. Bader, *Appl. Phys. Lett.* **66**, 2140 (1995).
8. I. Hodgkinson, S. Cloughley and Q. H. Wu *et al.*, *Appl. Opt.* **35**, 5563 (1996).

9. A. Rodriguez-Navarro, W. Otano-Rivera and J. M. Garcia-Ruiz *et al.*, *J. Mater. Res.* **12**, 1689 (1997).

10. Y. Takeda, T. Motohiro and T. Hioki *et al.*, *J. Vac. Sci. Technol.* **A16**, 7 (1998).

11. S. van Dijken, L. C. Jorritsma and B. Poelsema, *Phys. Rev. Lett.* **82**, 4038 (1999).

12. J.-P. Locquet, J. Perret and J. Fompeyrine *et al.*, *Nature* **394**, 453 (1998).

13. I. K. Schuller, *Nature* **394**, 419 (1998).

14. H. Brune, M. Giovannini and K. Bromann *et al.*, *Nature* **394**, 451 (1998).

15. R. Singhvi, A. Kumar and G. P. Lopez *et al.*, *Science* **264**, 696 (1994).

16. A. Ungersböck and B. Rahn, *J. Mater. Sci.: Mater. Med.* **5**, 434 (1994).

17. E. T. den Braber, J. E. de Ruijter and H. T. J. Smits *et al.*, *Biomater.* **17**, 1093 (1996).

18. A. Ungersböck, O. E. M. Pohler and F. W. Baumgart *et al.*, in *Medical Applications of Titanium and Its Alloys: The Material and Biological Issues*, ed. J. E. Lemons (ASTM, Ann Arbor, 1996).

19. C. S. Chen, M. Mrksich and S. Huang *et al.*, *Science* **276**, 1425 (1997).

20. B. Chehroudi, D. McDonnell and D. M. Brunette, *J. Biomed. Mater. Res.* **34**, 279 (1997).

21. R. G. Richards, G. R. Owen and B. A. Rahn *et al.*, *Cells and Materials* **7**, 15 (1997).

22. R. G. Richards, P. C. Lloyd and B. A. Rahn *et al.*, *J. Microscopy* **171**, 205 (1993).

23. K. J. Bundy, O. C. Roberts and K. O'Conner *et al.*, *J. Mater. Sci.: Mater. Med.* **5**, 500 (1994).

24. R. G. Richards, I. Gwynn and K. Bundy *et al.*, *Cell Biol. Int.* **19**, 1015 (1995).

25. R. G. Richards, B. A. Rahn and I. Gwynn, *J. Mater. Sci.: Mater. Med.* **6**, 120 (1995).

26. T. J. Webster, R. W. Siegel and R. Bizios, *Biomater.* **20**, 1221 (1999).

27. D. J. Chakrabarti, D. E. Laughlin and S. W. Chen *et al.*, in *Phase Diagrams of Binary Nickel Alloys*, ed. P. Nash (The Materials Information Society, 1991), Vol. 6, pp. 85–95.

28. A. Chambers and D. C. Jackson, *Philos. Mag.* **31**, 1357 (1975).

29. W. F. Egelhoff, *J. Vac. Sci. Technol.* **A2**, 350 (1984).

30. W. F. Egelhoff, *Phys. Rev.* **B30**, 1052 (1984).

31. S. A. Chambers, H. W. Chen and I. M. Vitomirov *et al.*, *Phys. Rev.* **B33**, 8810 (1986).

32. L. S. Perkins and A. E. DePristo, *Surf. Sci.* **319**, 225 (1994).

33. G. L. Kellogg, *Phys. Rev. Lett.* **73**, 1833 (1994).

34. J. K. Nørskov, K. W. Jacobsen and P. Stoltze *et al.*, *Surf. Sci.* **283**, 277 (1993).

35. H. Brune, H. Röder and C. Boragno *et al.*, *Phys. Rev. Lett.* **73**, 1955 (1994).

36. H. Röder, E. Hahn and H. Brune *et al.*, *Nature* **366**, 141 (1993).

37. B. Müller, B. Fischer and L. Nedelmann *et al.*, *Phys. Rev.* **B54**, 17858 (1996).

38. M. C. Bartelt and J. W. Evans, *Phys. Rev.* **B46**, 12675 (1992).

39. J. A. Stroscio and D. T. Pierce, *Phys. Rev.* **B49**, 8522 (1994).

40. J. A. Venables, *Philos. Mag.* **27**, 697 (1973).

41. J. A. Venables, G. D. T. Spiller and M. Hanbücken, *Rep. Prog. Phys.* **47**, 399 (1984).

42. H. Brune, *Surf. Sci. Rep.* **31**, 121 (1998).

43. M. C. Tringides (Plenum, New York, 1997).

44. J. A. Venables, *Phys. Rev.* **B36**, 4153 (1987).

45. M. von Smoluchowski, *Z. Phys. Chem.* **17**, 557 (1916).

46. M. von Smoluchowski, *Z. Phys. Chem.* **92**, 129 (1917).

47. M. J. Stowell, *Philos. Mag.* **26**, 349 (1972).

48. B. Lewis, *Surf. Sci.* **21**, 289 (1970).

49. G. S. Bales and D. C. Chrzan, *Phys. Rev.* **B50**, 6057 (1994).

50. M. C. Bartelt and J. W. Evans, *Phys. Rev.* **B54**, R17359 (1996).

51. H. Brune, H. Röder and K. Bromann *et al.*, *Thin Solid Films* **264**, 230 (1995).

52. M. F. Sykes and M. Glen, *J. Phys.* **A9**, 87 (1976).

53. M. C. Bartelt, L. S. Perkins and J. W. Evans, *Surf. Sci.* **344**, L1193 (1995).

54. J. A. Stroscio, D. T. Pierce and R. A. Dragoset, *Phys. Rev. Lett.* **70**, 3615 (1993).

55. J. J. D. Miguel, A. Sánches and E. Cebollada *et al.*, *Surf. Sci.* **189—190**, 1062 (1987).

56. M. Breeman and D. O. Boerma, *Surf. Sci.* **269/270**, 224 (1992).

57. H. J. Ernst, F. Fabre and J. Lapujoulade, *Phys. Rev.* **B46**, 1929 (1992).

58. J. K. Zuo, J. F. Wendelken and H. Dürr *et al.*, *Phys. Rev. Lett.* **72**, 3064 (1994).

59. H. Dürr, J. F. Wendelken and J. K. Zuo, *Surf. Sci.* **328**, L527 (1995).

60. M. H. Langelaar and D. O. Boerma, *Surf. Sci.* **352—354**, 597 (1996).

61. C. M. Zhang, M. C. Bartelt and J. M. Wen *et al.*, *J. Cryst. Growth* **174**, 851 (1997).

62. C. M. Zhang, M. C. Bartelt and J. M. Wen *et al.*, *Surf. Sci.* **406**, 178 (1998).

63. M. C. Bartelt, M. C. Tringides and J. W. Evans, *Phys. Rev.* **B47**, 13891 (1993).

64. A. G. Amar, F. Family and P. M. Lam, *Phys. Rev.* **B50**, 167 (1994).

65. J. G. Amar and F. Family, *Phys. Rev. Lett.* **74**, 149 (1995).

66. C. Ratsch, A. Zangwill and P. Smilauer, *Surf. Sci.* **314**, L937 (1994).

67. M. Schroeder and D. E. Wolf, *Phys. Rev. Lett.* **74**, 2062 (1995).

68. P. A. Mulheran and J. A. Blackman, *Phys. Rev.* **B53**, 10261 (1996).

69. J. A. Blackman and P. A. Mulheran, *Phys. Rev.* **B54**, 11681 (1996).

70. V. Bressler-Hill, S. Varma and A. Lorke *et al.*, *Phys. Rev. Lett.* **74**, 3209 (1995).

71. M. C. Bartelt, J. B. Hannon and A. K. Schmid *et al.*, *Coll. Surf.* **A165**, 373 (2000).

72. S. Harris and P. Smilauer, *Phys. Rev.* **B50**, 7952 (1994).

73. M. I. Larsson, W.-X. Ni and G. V. Hansson, *J. Appl. Phys.* **78**, 3792 (1995).

74. P. Smilauer and D. D. Vvedensky, *Phys. Rev.* **B48**, 17603 (1993).

75. D. D. Chambliss and K. E. Johnson, *Phys. Rev.* **B50**, 5012 (1994).

76. M. Bott, M. Hohage and M. Morgenstern *et al.*, *Phys. Rev. Lett.* **76**, 1304 (1996).

77. G. Zinsmeister, *Thin Solid Films* **7**, 51 (1971).

78. W. F. Egelhoff and I. Jacob, *Phys. Rev. Lett.* **62**, 921 (1989).

79. G. Vandoni, C. Félix and R. Monot *et al.*, *Surf. Sci.* **320**, L63 (1994).

80. H. Brune, G. S. Bales and C. Boragno *et al.*, *Phys. Rev.* **B60**, 5991 (1999).

81. Z. Zhang, X. Chen and M. G. Lagally, *Phys. Rev. Lett.* **73**, 1829 (1994).

82. R. Hwang, J. Schröder and C. Günther *et al.*, *Phys. Rev. Lett.* **67**, 3297 (1991).

83. H. Brune, C. Romanczyk and H. Röder *et al.*, *Nature* **369**, 469 (1994).

84. H. Röder, K. Bromann and H. Brune *et al.*, *Phys. Rev. Lett.* **74**, 3217 (1995).

85. M. Hohage, M. Bott and M. Morgenstern *et al.*, *Phys. Rev. Lett.* **76**, 2366 (1996).

86. H. Brune, K. Bromann and J. Jacobsen *et al.*, *Surf. Sci. Lett.* **349**, L115 (1996).

87. C.-L. Liu, *Surf. Sci.* **316**, 294 (1994).

88. P. Stoltze, *J. Phys. Condens. Matter* **6**, 9495 (1994).

89. E. Kopatzki, S. Günther and W. Nichtl-Pecher *et al.*, *Surf. Sci.* **284**, 154 (1993).

90. E. Hahn, E. Kampshoff and N. Wälchli *et al.*, *Phys. Rev. Lett.* **74**, 1803 (1995).

91. J. M. Wen, J. W. Evans and M. C. Bartelt *et al.*, *Phys. Rev. Lett.* **76**, 652 (1996).

92. A. Brodde, G. Wilhelmi and D. Badt *et al.*, *J. Vac. Sci. Technol.* **B9**, 920 (1991).

93. M. A. Grinfeld, *Sov. Phys. Dokl.* **31**, 831 (1986).

94. D. Srolovitz, *Acta Metall.* **37**, 621 (1989).

95. B. J. Spencer, P. W. Voorhees and S. H. Davis, *Phys. Rev. Lett.* **67**, 3696 (1991).

96. J. Tersoff and R. M. Tromp, *Phys. Rev. Lett.* **70**, 2782 (1993).

97. Y.-W. Mo, R. Kariotis and B. S. Swartzentruber *et al.*, *J. Vac. Sci. Technol.* **8**, 232 (1990).

98. B. Müller, T. Kuhlmann and K. Lischka *et al.*, *Surf. Sci.* **418**, 256 (1998).

99. J. Tersoff, *Phys. Rev. Lett.* **74**, 434 (1995).

100. R. Kern, G. L. Lay and J. J. Metois, in *Curr. Topics in Mater. Sci.*, ed. E. Kaldis (Elsevier Science, Amsterdam, 1979), Vol. 3, pp. 131–419.

101. L. Vitos, A. V. Ruban and H. L. Skriver *et al.*, *Surf. Sci.* **411**, 186 (1998).

102. J. Fassbender, U. May and B. Schirmer *et al.*, *Phys. Rev. Lett.* **75**, 4476 (1995).

103. B. Müller, L. P. Nedelmann and B. Fischer *et al.*, *Surf. Rev. Lett.* **5**, 769 (1998).

104. F. C. Frank and J. H. van der Merwe, *Proc. R. Soc. London* **A198**, 205 (1949).

105. W. A. Jesser and D. Kuhlmann-Wilsdorf, *Phys. Status Solidi* **19**, 95 (1967).

106. C. A. B. Ball, *Phys. Status Solidi* **42**, 357 (1970).

107. J. W. Matthews and J. L. Crawford, *Thin Solid Films* **5**, 187 (1970).

108. R. Bruinsma and A. Zangwill, *J. Phys. (Paris)* **47**, 2055 (1986).

109. H. Brune, H. Röder and C. Boragno *et al.*, *Phys. Rev.* **B49**, 2997 (1994).

110. C. Günther, J. Vrijmoeth and R. Q. Hwang *et al.*, *Phys. Rev. Lett.* **74**, 754 (1995).

111. J. A. Meyer, P. Schmid and R. J. Behm, *Phys. Rev. Lett.* **74**, 3864 (1995).

112. C. B. Carter and R. Q. Hwang, *Phys. Rev.* **B51**, 4730 (1995).

113. J. A. Matthews, *Epitaxial Growth* (Academic, New York, 1975).

114. B. Müller, B. Fischer and L. Nedelmann *et al.*, *Phys. Rev. Lett.* **76**, 2358 (1996).

115. B. Müller, L. Nedelmann and B. Fischer *et al.*, *J. Vac. Sci. Technol.* **A14**, 1878 (1996).

116. L. Nedelmann, B. Müller and B. Fischer *et al.*, *Surf. Sci.* **376**, 113 (1997).

117. M. Nielsen, R. Feidenhans'l and F. B. Rasmussen *et al.*, *Physica* **B248**, 1 (1998).

118. F. B. Rasmussen, J. Baker and M. Nielsen *et al.*, *Phys. Rev. Lett.* **79**, 4413 (1997).

119. F. B. Rasmussen, J. Baker and M. Nielsen *et al.*, *Physica* **B248**, 34 (1998).

120. B. Müller, L. Nedelmann and B. Fischer *et al.*, *Surf. Rev. Lett.* **4**, 1161 (1997).

121. J. P. Bucher, E. Hahn and P. Fernandez *et al.*, *Europhys. Lett.* **27**, 473 (1994).

122. M. Henzler, C. Homann and U. Malaske *et al.*, *Phys. Rev.* **B52**, R17060 (1995).

123. N. Breuer, A. M. Funtikov and U. Stimming *et al.*, *Surf. Sci.* **335**, 145 (1995).

124. M. Henzler and W. Göpel, *Oberflächenphysik des Festkörpers* (Teubner, Stuttgart, 1994).

125. B. Müller (Dresden University of Technology, Dresden, 1988).

126. L. Däweritz and R. Hey, *Surf. Sci.* **236**, 15 (1990).

127. W. Mönch, *Semiconductor Surfaces and Interfaces* (Springer-Verlag, Berlin, New York, 1995).

128. J. Behrend (Humboldt-University, Berlin, 1996).

129. A. R. Avery, H. T. Dobbs and D. M. Holmes *et al.*, *Phys. Rev. Lett.* **79**, 3938 (1997).

130. K. N. Baker, *Polymer* **34**, 1571 (1993).
131. N. Kirova, S. Brazovskii and A. R. Bishop, *Synth. Met.* **100**, 29 (1999).
132. P. Puschnig and C. Ambrosch-Draxl, *Phys. Rev.* **B60**, 7891 (1999).
133. I. C. Lewis and J. B. Barr, *Mol. Cryst. Liq. Cryst.* **72**, 65 (1981).
134. P. A. Irvine, D. C. Wu and P. J. Flory, *J. Chem. Soc., Faraday Trans. 1* **80**, 1821 (1984).
135. R. Resel, N. Koch and F. Meghdadi *et al.*, *Thin Solid Films* **305**, 232 (1997).
136. C. Chevrot, O. Brihaye and C. Legrand *et al.*, *Synth. Met.* **55—57**, 5075 (1993).
137. F. Garnier, G. Horowitz and X. Z. Peng *et al.*, *Synth. Met.* **45**, 163 (1991).
138. K. Seki, U. O. Karlsson and R. Engelhardt *et al.*, *Chem. Phys.* **91**, 459 (1984).
139. S. Tasch, C. Brandstätter and F. Meghdadi *et al.*, *Adv. Mater.* **9**, 33 (1997).
140. H. Yanagi and S. Okamoto, *Appl. Phys. Lett.* **71**, 2563 (1997).
141. H. Yanagi, S. Okamoto and T. Mikami, *Synth. Met.* **91**, 91 (1997).
142. K. Erlacher, R. Resel and S. Hampel *et al.*, *Surf. Sci.* **437**, 191 (1999).
143. A. Gustafsson, D. Hessman and L. Samuelson *et al.*, *J. Cryst. Growth* **147**, 27 (1995).
144. M. Klemenc, F. Meghdadi and S. Voss *et al.*, *Synth. Met.* **85**, 1243 (1997).
145. R. Resel, K. Erlacher and B. Müller *et al.*, *Surf. Int. Anal.* **29** (2000).
146. L. Athouel, G. Froyer and M. T. Riou *et al.*, *Thin Solid Films* **274**, 35 (1996).
147. Y. W. Mo, J. Kleiner and M. B. Webb *et al.*, *Phys. Rev. Lett.* **66**, 1998 (1991).
148. B. Voigtländer and A. Zinner, *Surf. Sci.* **292**, L775 (1993).
149. M. Horn-von Hoegen and H. Pietsch, *Surf. Sci.* **321**, L129 (1994).
150. B. Voigtländer, A. Zinner and T. Weber *et al.*, *Phys. Rev.* **B51**, 7583 (1995).
151. B. Müller and M. Henzler, *Surf. Sci.* **389**, 338 (1997).
152. L. Bardotti, P. Jensen and A. Hoareau *et al.*, *Phys. Rev. Lett.* **74**, 4694 (1995).
153. L. Bardotti, P. Jensen and A. Hoareau *et al.*, *Surf. Sci.* **367**, 276 (1996).
154. P. Jensen, *Rev. Mod. Phys.* **71**, 1695 (1999).
155. E. Umbach, M. Sokolowski and R. Fink, *Appl. Phys.* **A63**, 565 (1996).
156. H. Yanagi and T. Morikawa, *Appl. Phys. Lett.* **75**, 187 (1999).
157. M. Era, T. Tsutsui and S. Saito, *Appl. Phys. Lett.* **67**, 2436 (1995).
158. A. Niko, F. Meghdadi and C. Ambrosch-Draxl *et al., Synth. Met.* **76**, 177 (1996).
159. A. Piaggi, G. Lanzani and G. Bongiovanni *et al.*, *Phys. Rev.* **B56**, 10133 (1997).
160. T. Mikami and H. Yanagi, *Appl. Phys. Lett.* **73**, 563 (1998).
161. A. Andreev, G. Matt and C. J. Brabec *et al.*, *Adv. Mater.* **12**, 629 (2000).
162. A. Kawaguchi, M. Tsuji and S. Moriguchi *et al.*, *Bull. Inst. Chem. Res.*, *Kyoto Univ.* **64**, 54 (1986).
163. K. Matsushige, T. Hamano and T. Horiuchi, *J. Crystal Growth* **146**, 641 (1995).
164. J. Patscheider (Surface-and-Coatings-Technology, 1998).
165. L. Jorritsma, *Growth Anisotropies in Cu(001) Homoepitaxy* (Wormgoor B. V., Almelo, 1997).
166. C. Cai, M. M. Bösch and Y. Tao *et al.*, *J. Am. Chem. Soc.* **120**, 8563 (1998).
167. B. Müller, M. Jäger and Y. Tao *et al.*, *Opt. Mater.* **12**, 345 (1999).
168. B. Müller, C. Cai and A. Kündig *et al.*, *Appl. Phys. Lett.* **74**, 3110 (1999).
169. B. Müller, C. Cai and M. Bösch *et al.*, *Thin Solid Films* **343—344**, 171 (1999).
170. C. Cai, B. Müller and J. Weckesser *et al.*, *Adv. Mater.* **11**, 750 (1999).
171. C. Cai, M. Bösch and B. Müller *et al.*, *Adv. Mater.* **11**, 745 (1999).
172. L. Abelmann and C. Lodder, *Thin Solid Films* **305**, 1 (1997).
173. C. Tang and S. Liang, *Phys. Rev. Lett.* **71**, 2769 (1993).
174. H. van Kranenburg and C. Lodder, *Mater. Sci. Eng.* **R11**, 295 (1994).
175. I. Hodgkinson, Q. H. Wu and A. McPhun, *J. Vac. Sci. Technol.* **B16**, 2811 (1998).
176. R. N. Tait, T. Smy and M. J. Brett, *Thin Solid Films* **226**, 196 (1993).
177. O. P. Karpenko, J. C. Bilello and S. M. Yalisove, *J. Appl. Phys.* **82**, 1397 (1997).
178. R. Messier, T. Gehrke and C. Frankel *et al.*, *J. Vac. Sci. Technol.* **A15**, 2148 (1997).
179. K. Robbie, J. C. Sit and M. J. Brett, *J. Vac. Sci. Technol.* **A16**, 1115 (1998).
180. N. O. Young and J. Kowal, *Nature* **183**, 104 (1959).
181. R. M. A. Azzam, *Appl. Phys. Lett.* **61**, 3118 (1992).
182. K. Robbie, M. J. Brett and A. Lakhtakia, *J. Vac. Sci. Technol.* **A13**, 2991 (1995).
183. K. Robbie, L. J. Friedrich and S. K. Dew *et al.*, *J. Vac. Sci. Technol.* **A13**, 1032 (1995).
184. K. Robbie, D. J. Broer and M. J. Brett, *Nature* **399**, 764 (1999).
185. K. Robbie and M. J. Brett, *J. Vac. Sci. Technol.* **A15**, 1460 (1997).
186. P. I. Rovira, R. A. Yarussi and R. W. Collins *et al.*, *Appl. Phys. Lett.* **71**, 1180 (1997).
187. P. I. Rovira, R. A. Yarussi and R. W. Collins *et al.*, *Thin Solid Films* **313—314**, 373 (1998).
188. I. Hodgkinson, Q. H. Wu and J. Hazel, *Appl. Optics* **37**, 2653 (1998).

189. A. Rodger and B. Nordén, *Circular Dichroism and Linear Dichroism* (Oxford University Press, Oxford, New York, Tokyo, 1997).

190. R. E. Gill, G. Hadziioannou and P. Lang *et al.*, *Adv. Mater.* **9**, 331 (1997).

191. J. Jerphagnon and S. K. Kurtz, *J. Appl. Phys.* **41**, 1667 (1970).

192. U. Gubler and C. Bosshard, *Phys. Rev.* **B61**, 10702 (2000).

193. C. Bosshard, U. Gubler and P. Kaatz *et al.*, *Phys. Rev.* **B61**, 10688 (2000).

194. D. A. Kleinman, *Phys. Rev.* **126**, 1977 (1962).

195. G. Decher, B. Tieke and C. Bosshard *et al.*, *J. Chem. Soc., Chem. Commun.* **1988**, 933 (1988).

196. G. J. Ashwell, P. D. Jackson and W. A. Crossland, *Nature* **368**, 438 (1994).

197. G. J. Ashwell, G. Jefferies and C. D. George *et al.*, *J. Mater. Chem.* **6**, 131 (1996).

198. J. V. Barth, J. Weckesser and C. Cai *et al.*, *Angew. Chem. Int. Ed.* **39**, 1230 (2000).

199. D. E. Sanders, D. M. Halstead and A. E. DePristo, *J. Vac. Sci. Technol.* **A10**, 1986 (1992).

200. E. Wintermantel and S. W. Ha, *Biokompatible Werkstoffe und Bauweisen — Implantate für Medizin und Umwelt* (Springer-Verlag, Berlin, 1996).

201. A. Curtis and C. Wilkinson, *Biochem. Soc. Symp.* **65**, 15 (1999).

202. L. Smith, T. Nguyen and J. R. Dennis *et al.*, in preparation (2000).

203. J. M. Marée, K. Nakagawa and F. M. Mulders *et al.*, *Surf. Sci.* **191**, 305 (1987).

204. Y. W. Mo, D. E. Savage and B. S. Schwarzentruber *et al.*, *Phys. Rev. Lett.* **65**, 1020 (1990).

205. U. Köhler, O. Jusko and B. Müller *et al.*, *Ultramicroscopy* **42–44**, 832 (1992).

206. D. J. Eaglesham and M. Cerullo, *Phys. Rev. Lett.* **64**, 1943 (1990).

207. M. Kästner and B. Voigtländer, *Phys. Rev. Lett.* **82**, 2745 (1999).

208. F. M. Ross, J. Tersoff and R. M. Tromp, *Phys. Rev. Lett.* **80**, 984 (1998).

209. G. Medeiros-Ribeiro, A. M. Bratkovski and T. I. Kamins *et al.*, *Science* **279**, 353 (1998).

210. F. M. Ross, R. M. Tromp and M. C. Reuter, *Science* **286**, 1931 (1999).

211. O. V. Kolosov, M. R. Castell and C. D. Marsh *et al.*, *Phys. Rev. Lett.* **81**, 1046 (1998).

212. I. Daruka, J. Tersoff and A.-L. Barabasi, *Phys. Rev. Lett.* **82**, 2753 (1999).

213. L. G. Wang, P. Kratzer and M. Scheffler *et al.*, *Phys. Rev. Lett.* **82**, 4042 (1999).

214. O. Leifeld, D. Grützmacher and B. Müller *et al.*, *Mater. Res. Soc. Proc.* **533**, 183 (1998).

215. O. Leifeld, E. Müller and D. Grützmacher *et al.*, *Appl. Phys. Lett.* **74**, 994 (1999).

216. T. I. Kamins and R. S. Williams, *Surf. Sci.* **405**, L580 (1998).

217. G. Medeiros-Ribeiro, T. I. Kamins and D. A. A. Ohlberg *et al.*, *Phys. Rev.* **B58**, 3533 (1998).

218. T. I. Kamins, G. Medeiros-Ribeiro and D. A. A. Ohlberg *et al.*, *Appl. Phys.* **A67**, 727 (1998).

219. T. I. Kamins, G. Medeiros-Ribeiro and D. A. A. Ohlberg *et al.*, *J. Appl. Phys.* **85**, 1159 (1999).

220. J. Tersoff, *Phys. Rev. Lett.* **76**, 1675 (1996).

221. C. Teichert, M. G. Lagally and L. J. Peticolas *et al.*, *Phys. Rev.* **B53**, 16334 (1996).

222. C. Teichert, J. C. Bean and M. G. Lagally, *Appl. Phys.* **A67**, 675 (1998).

223. F. Liu, S. E. Davenport and H. M. Evans *et al.*, *Phys. Rev. Lett.* **82**, 2528 (1999).

224. P. Sutter and M. G. Lagally, *Phys. Rev. Lett.* **84**, 4637 (2000).

225. R. M. Tromp, F. M. Roos and M. C. Reuter, *Phys. Rev. Lett.* **84**, 4641 (2000).

226. B. Cunningham, J. O. Chu and S. Akbar, *Appl. Phys. Lett.* **59**, 3574 (1991).

227. A. Hartmann, L. Vescan and C. Dieker *et al.*, *Mater. Sci. Technol.* **11**, 410 (1995).

228. T. I. Kamins, E. C. Carr and R. S. Williams *et al.*, *J. Appl. Phys.* **81**, 211 (1997).

229. R. H. Dettre and R. E. Johnson Jr., *Adv. Chem. Ser.* **43**, 136 (1964).

230. J. J. Bikerman, *J. Phys. Coll. Chem.* **54**, 653 (1950).

231. H. Kamusewitz, W. Possart and D. Paul, *Coll. Surf.* **A156**, 271 (1999).

232. P. Lenz and R. Lipowsky, *Phys. Rev. Lett.* **80**, 1920 (1998).

233. H. Gau, S. Herminghaus and P. Lenz *et al.*, *Science* **283**, 46 (1999).

234. R. Lipowsky, P. Lenz and P. S. Swan, *Coll. Surf.* **A161**, 3 (2000).

235. G. Zografi and B. A. Johnson, *Int. J. Pharmaceutics* **22**, 159 (1984).

236. K. L. Woo and T. R. Thomas, *Wear* **58**, 331 (1980).

237. J. Vienken, M. Diamantoglou and C. Hahn *et al.*, *Artificial Organs* **19**, 398 (1995).

238. J. H. Lee, J. W. Lee and G. Khang *et al.*, *Biomater.* **18**, 351 (1997).

239. T. Knoell, J. Safarik and T. Cormack *et al.*, *J. Membrane Science* **157**, 117 (1999).

240. L. W. Schwartz and S. Garoff, *Langmuir* **1**, 219 (1985).

241. R. N. Wenzel, *Ind. Eng. Chem.* **28**, 988 (1936).

242. K. A. Vetelino, P. R. Story and B. DeClerq *et al.*, *Int. J. Microcircuits and Electronic Packaging.* **19**, 212 (1996).

243. E. Fadda, P. Warren and F. Chollet *et al.*, *J. Adhesion Sci. Technol.* **10**, 1067 (1996).

244. I.-M. Lee and C. G. Takoudis, *J. Vac. Sci. Technol.* **A15**, 3154 (1997).

245. L. D. Eske and D. W. Galipeau, *Coll. Surf.* **A154**, 33 (1999).

246. D. Y. Kwok and A. W. Neumann, *Coll. Surf.* **A161**, 31 (2000).

247. R. E. Johnson Jr. and R. H. Dettre, *Adv. Chem. Ser.* **43**, 112 (1964).
248. W. Jin and J. Koplik, *Phys. Rev. Lett.* **78**, 1520 (1997).
249. W. J. Herzberg and J. E. Marian, *J. Coll. Interf. Sci.* **33**, 161 (1970).
250. L. W. Schwartz and S. Garoff, *J. Coll. Interf. Sci.* **106**, 422 (1985).
251. C. G. Gölander and E. Kiss, *J. Coll. Interf. Science* **121**, 240 (1988).
252. M. Riedel, B. Müller and E. Wintermantel, *Biomater.*, submitted (2000).
253. M. Wahlgren and T. Arnebrant, *Trends Biotech.* **9**, 201 (1991).
254. P. A. Underwood, J. G. Steele and B. A. Dalton, *J. Cell Sci.* **104**, 793 (1993).
255. C. A. Janeway and P. Travers, *Immunologie* (Spektrum Akademischer Verlag, Heidelberg, 1997).
256. H. X. You and C. R. Lowe, *J. Coll. Interf. Science* **182**, 586 (1996).
257. R. van Furth, in *Cell Kinetics: The Inflammatory Reaction*, ed. O. H. Iversen (Springer, Berlin, 1989), pp. 125–150.
258. C. A. Dinarello, in *Interleukin-1, Inflammation and Desease*, eds. R. Bomford and B. Henderson (Elsevier, Amsterdam, 1989), pp. 17–28.
259. A. Gearing and R. Thorpe, in *Interleukin-1, Inflammation and Desease*, eds. R. Bomford and B. Henderson (Elsevier, Amsterdam, 1989), pp. 79–91.
260. J. A. Cairns, G. R. Guy and Y. H. Tan, *Immunology* **75**, 669 (1992).
261. K. M. DeFife, M. S. Shive and K. M. Hagen *et al.*, *J. Biomed. Mater. Res.* **44**, 298 (1999).

Abbreviations

0D	zero-dimensional
1D	one-dimensional
2D	two-dimensional
3D	three-dimensional
%BZ	percent Brillouin zone
AFM	atomic force microscopy
BGG	bovine γ-globulin
BSA	bovine serum albumin
ECM	extracellular matrix
EMT	effective medium theory
Fab	fragment antigen binding
Fc	fragment-crystallizable
fcc	face-cubic-centered
FWHM	full width at half maximum
hcp	hexagonal close-packed
IL	interleukin
LEED	low energy electron diffraction
LSM	laser scanning microscope
MBD	molecular beam deposition
MBE	molecular beam epitaxy
MOPAC	semiempirical quantum chemistry program package
NMR	nuclear magnetic resonance
PEBA	4-(pyridin-4-ylethynyl)benzoic acid
POD	peroxidase
PVBA	4-[trans-(pyridin-4-ylvinyl)]benzoic acid
RHEED	reflection high energy electron diffraction
RMS	root mean square
SEM	scanning electron microscopy
SHG	second harmonic generation
STM	scanning tunneling microscopy
TED	transmission electron diffraction
TNF-α	tumor necrosis factor

Symbols and Constants

a_b	bulk lattice constant
a_{Cu}, a_{Ni}	lattice constant of copper and nickel
a_d	lattice constant of deposit
a_s	surface lattice constant
A	island size
A_c	critical island size
b	constant of Tersoff–Tromp theory
d_{ijk}	second order susceptibility tensor
D	diffusion coefficient
D_1	stripe width at monolayer coverage
D_2	stripe width at double layer coverage
D_i	stripe width at i-layer coverage
e	Euler number
E	normalized energy
E_a	effective activation energy
E_b	dimer bond energy
E_i	binding energy for the critical nucleus i
E_h	activation energy for island height
E_m	height of migration barrier
E^*	energy gain of forming square-shaped with respect to ramified islands
E^ω	electric field at frequency ω
H	height of 3D islands
i	size of the critical nucleus
$I^{2\omega}$	SHG intensity
k	Boltzmann constant
$K_\parallel$	parallel component of scattering vector
$K_\perp$	perpendicular component of scattering vector
L	length of 3D islands

m	lattice mismatch	W_∞	island with at infinite island size
n_1	monomer density	Δh	height of stripes
n_s	density of islands of size s	$\Delta\theta$	contact angle hysteresis
$n_s(\theta)$	island size distribution	ε_0	vacuum permittivity
N_s	density of stripes of size s	φ	polarization angle
n_x	density of stable islands	φ_0	mosaic spread of substrate
p	island perimeter	φ_{25}	mosaic spread of a 25-monolayer-thick
$P_i^{2\omega}$	components of the macroscopic		film
	polarization	ν	hopping rate
r	roughness factor	ν_0	attempt frequency for monomer migration
R	deposition rate	ν_0^*	attempt frequency of dimer dissociation
s	island size	χ	scaling exponent
$\langle s \rangle$	mean stripe length	ρ	stripe density
$s_{\min}$	minimum stripe length	σ_1	capture number for monomers
S	mean island size	σ_x	capture number of stable islands
t	time	θ	coverage
T	substrate temperature	θ_a	advancing contact angle
T_c	critical temperature	θ_e	equilibrium contact angle (Young's angle)
w	arm width of islands	θ_r	receding contact angle
W	width of 3D islands	θ–2θ	angular scan in X-ray diffraction
W_c	island width at critical size	Θ	angle of incidence